Chapter 4
Ion Thruster Plasma Generators

Ion thrusters are characterized by the electrostatic acceleration of ions extracted from a plasma generator. Ion thruster geometries are best described in terms of three basic components: the ion accelerator, the plasma generator, and the electron neutralizer. The ion accelerator, described in Chapter 5, typically uses electrically biased multi-aperture grids to produce the ion beam. The neutralizer cathode, which is discussed in Chapter 6, is positioned outside the thruster body to provide electrons to neutralize the ion beam and maintain the potential of the thruster and spacecraft relative to the space plasma potential. In this chapter, three types of the third component of modern flight ion thrusters, namely the plasma generator, are discussed. These plasma generators utilize direct current (DC) electron discharges, radio frequency (rf) discharges and microwave discharges to produce the plasma. Physics-based models will be developed and used throughout the chapter to describe the performance and characteristics of these different plasma-generation techniques.

4.1 Introduction

The basic geometry of an ion thruster plasma generator is illustrated well by the classic DC electron discharge plasma generator. This version of the thruster plasma generator utilizes an anode potential discharge chamber with a hollow cathode electron source to generate the plasma from which ions are extracted to form the thrust beam. A simplified schematic of a DC electron bombardment ion thruster with these components coupled to a multi-grid accelerator is shown in Fig. 4-1. Neutral propellant gas is injected into the discharge chamber, and a small amount is also injected through the hollow cathode. Electrons extracted from the hollow cathode enter the discharge chamber and ionize the propellant gas. To improve the efficiency of the discharge in producing ions, some form of magnetic confinement typically is employed at the anode wall. The magnetic fields provide confinement primarily of the energetic electrons, which increases the electron path length prior to loss to the anode wall and improves the

ionization probability of the injected electrons. Proper design of the magnetic field is critical to providing sufficient confinement for high efficiency while maintaining adequate electron loss to the anode to produce stable discharges over the operation range of the thruster.

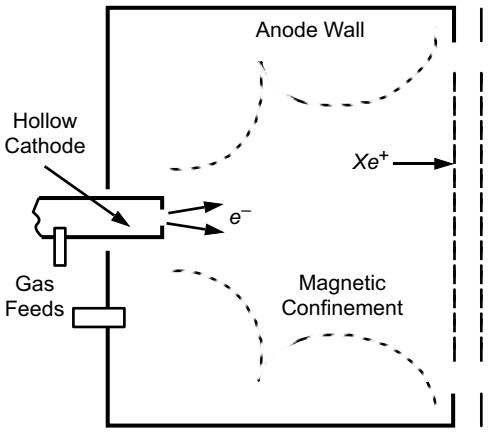

Fig. 4-1. Illustration of a DC-discharge electron bombardment ion thruster.

Several power supplies are required to operate the cathode and plasma discharge. A simplified electrical schematic typically used for DC-discharge plasma generators is shown in Fig. 4-2. The cathode heater supply raises the thermionic emitter to a sufficient temperature to emit electrons, and is turned off once the plasma discharge is ignited. The keeper electrode positioned around the hollow cathode tube is used to facilitate striking the hollow cathode discharge, and also protects the cathode from ion bombardment from the discharge chamber region. The cathode and keeper are discussed in Chapter 6. The discharge supply is connected between the hollow cathode and the anode, and normally is run in the current-regulated mode in order to provide a stable discharge at different power levels.

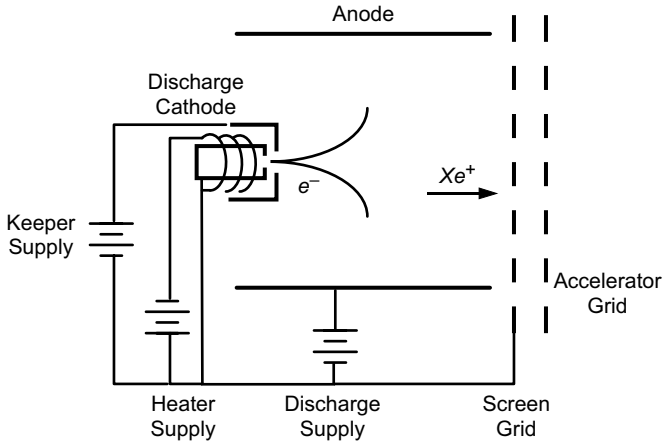

Fig. 4-2. Electrical schematic of a DC-discharge ion thruster with the cathode heater, keeper and discharge power supplies.

RF and microwave ion thrusters utilize ion accelerator and electron-neutralizer implementations nearly identical to that of the DC-discharge ion thruster. However, these thrusters do not employ a discharge hollow cathode or anode power supply. These components are replaced by rf or microwave antenna structures, sources of microwave radiation and compatible discharge chambers to ionize the propellant gas and deliver the ions to the accelerator structure. These thrusters also utilize either applied or self-generated magnetic fields to improve the ionization efficiency of the system.

The three thruster plasma generators to be discussed here, DC electron discharge, rf, and microwave discharge, have been successfully developed and flown in space. The principles of these different classes of plasma generators are described in the following sections after a discussion of the plasma generator efficiency that can be expected in an idealized case.

4.2 Idealized Ion Thruster Plasma Generator

It is worthwhile to examine an ion thruster in the simplest terms to provide an understanding of the dominant processes in the particle flows and energy transport required to produce the plasma. The idealized thruster model has power injected by arbitrary means into a volume filled with neutral gas to produce ionization and neutral gas excitation, with all the ions going to the accelerator grids and an equal number of plasma electrons going to the wall to conserve charge. This is illustrated schematically in Fig. 4-3. For this model, the thruster discharge chamber has a volume V that fully encloses the plasma that is produced by ionization of neutral gas by the plasma electrons. The ions from the plasma flow only to the accelerator grid structure (perfect confinement elsewhere in the discharge chamber) with a current given by the Bohm current:

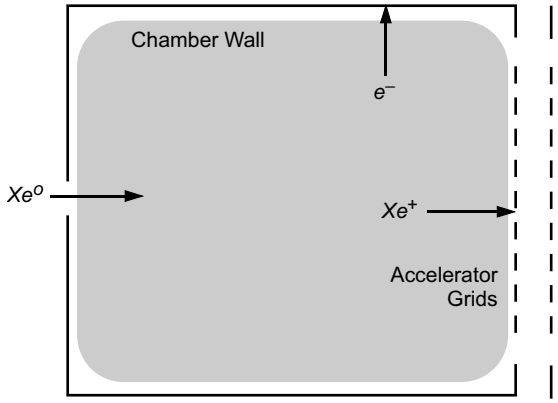

Fig. 4-3. Idealized ion thruster with the ions assumed going to the grids and electrons going to the chamber wall.

$$I_i = \frac{1}{2} n_i e v_a A \,, \tag{4.2-1}$$

where n_i is the ion density in the center of the volume; v_a is the ion acoustic velocity; A is the total ion loss area, which is assumed to be only the grid area; and the ions are assumed to be cold relative to the electrons. The ion beam current is then the total ion current to the grids multiplied by the effective grid transparency, T_g:

$$I_b = \frac{1}{2} n_i e v_a A T_g \,, \tag{4.2-2}$$

where the current lost to the accel and decel grids has been neglected as small. Ions are assumed to be produced by ionization of neutral particles by the plasma electrons in the discharge chamber, with a rate given by

$$I_p = n_o n_e e \langle \sigma_i v_e \rangle V \,, \tag{4.2-3}$$

where n_o is the neutral gas density, n_e is the plasma electron density, σ_i is the ionization cross section, v_e is the electron velocity, and the term in the brackets is the reaction rate coefficient which is the ionization cross section averaged over the Maxwellian electron velocity distribution function. The formulation of the reaction rate coefficient was described in Chapter 3, and the values for xenon as a function of electron temperature are given in Appendix E.

Power is conserved in the system, so the power put into the plasma is equal to the power that comes out in the form of charged particles and radiation. To first order, the power injected into the plasma goes into ionization and excitation of the neutral gas, heating of the electrons, and power that is carried to the walls and the grids by the ions and electrons. The power that is put into the system is then

$$P_{\text{in}} = I_p U^+ + I^* U^* + I_i \varepsilon_i + \frac{n_e V}{\tau} \varepsilon_e \,, \tag{4.2-4}$$

where U^+ is the ionization potential of the propellant gas, U^* is the excitation potential of the gas, τ is the average electron confinement time, ε_i is the ion energy carried to the walls, and ε_e is the electron energy carried to the walls by the electrons leaving the plasma. The term I^* is the excited neutral production rate, given by

$$I^* = \sum_j n_o n_e e \left\langle \sigma_* v_e \right\rangle_j V , \tag{4.2-5}$$

where σ_* is the excitation cross section and the reaction rate coefficient is averaged over the electron distribution function and summed over all possible excited states *j*. Using Eqs. (4.2-3) and (4.2-5) in Eq. (4.2-4), the power input can then be written as

$$P_{\text{in}} = n_o n_e \left\langle \sigma_i v_e \right\rangle V \left[U^+ + \frac{\left\langle \sigma_* v_e \right\rangle_j}{\left\langle \sigma_i v_e \right\rangle} U^* \right] + I_i \varepsilon_i + \frac{n_e V}{\tau} \varepsilon_e . \tag{4.2-6}$$

Assuming quasi-neutrality ($n_i \approx n_e$) and that the ions and electrons leave the volume by ambipolar flow at the same rate, which is a function of the mean confinement time τ, the ion current out is given by

$$I_i = \frac{1}{2} n_i e v_a A = \frac{n_i e V}{\tau} . \tag{4.2-7}$$

The mean confinement time for ions and electrons is then

$$\tau = \frac{2V}{v_a A} . \tag{4.2-8}$$

The energy that an electron removes from the plasma as it goes to the wall is given by

$$\varepsilon_e = 2 \frac{kT_e}{e} + \phi , \tag{4.2-9}$$

where ϕ is the plasma potential relative to the wall. Equation (4.2-9) is derived in Appendix C. The ions fall first through the pre-sheath potential, approximated by $T_{eV}/2$ to produce the Bohm velocity, and then through the sheath potential. Each ion then removes from the plasma a total energy per ion of

$$\varepsilon_i = \frac{1}{2} \frac{kT_e}{e} + \phi . \tag{4.2-10}$$

The plasma potential in these two equations is found from the electron current leaving the plasma, which is given by Eq. (3.7-52):

$$I_a = \frac{1}{4}\left(\frac{8kT_e}{\pi\, m}\right)^{1/2} e\, n_e\, A_a \exp^{-e\phi/kT_e}, \tag{4.2-11}$$

where A_a is the electron loss area and m is the electron mass. Since ambipolar ion and electron flow to the wall was assumed, equate Eqs. (4.2-1) and (4.2-11) and use $\sqrt{T_e/M}$ for the ion acoustic velocity to give the plasma potential relative to the wall:

$$\phi = \frac{kT_e}{e}\ln\left[\frac{A_a}{A}\sqrt{\frac{2M}{\pi m}}\right]. \tag{4.2-12}$$

Equation (4.2-12) is normally called the *floating potential* and applies in this case because there are no applied potentials in our ideal thruster to draw a net current.

The electron temperature can be found by equating the ion production and loss rates, Eqs. (4.2-1) and (4.2-3), which gives

$$\frac{\sqrt{kT_e/M}}{\langle\sigma_i v_e\rangle} = \frac{2n_o V}{A}. \tag{4.2-13}$$

The reaction rate coefficient in the denominator depends on the electron temperature, and so this equation can be solved for T_e if the discharge chamber volume, neutral pressure, and ion loss area are known.

The discharge loss is defined as the power into the plasma divided by the beam current out of the thruster, which is a figure of merit for the efficiency of the plasma-generation mechanism. The discharge loss for this idealized thruster, using Eq. (4.2-2) for the beam current, is then given by

$$\eta_d = \frac{P_{in}}{I_b} = \frac{2n_o\langle\sigma_i v_e\rangle V}{v_a\, A\, T_g}\left[U^+ + \frac{\langle\sigma_* v_e\rangle_j}{\langle\sigma_i v_e\rangle}U^*\right] + \frac{1}{T_g e}\left[2.5kT_e + 2kT_e\ln\left(\frac{A_a}{A}\sqrt{\frac{2M}{\pi m}}\right)\right]. \tag{4.2-14}$$

As evident in Eq. (4.2-14), the grid transparency (T_g) directly affects the discharge loss, and the input power is distributed between the first term related

to producing ions and excited neutrals, and the second term related to heating the electrons that are lost to the walls.

To evaluate Eq. (4.2-14), the ratio of the excitation to ionization reaction rates as a function of the Maxwellian electron temperature must be known. This is shown in Fig. 4-4 for xenon gas from data in Appendix E. For electron temperatures below about 8 V, the excitation rate exceeds the ionization rate in xenon for Maxwellian electrons. Since the lowest excitation potential is near the ionization potential in xenon, this higher excitation rate results in more of the input power being radiated to the walls than producing ions. This effect explains at least part of the inefficiency inherent in xenon plasma generators. Excitation rates equal to or higher than the ionization rate at low electron temperatures are also generally found for other inert gas propellants.

The discharge loss from Eq. (4.2-14) for this ideal thruster example is plotted as a function of the mass utilization efficiency for a generic 20-cm-diameter thruster in Fig. 4-5, where the ionization potential of xenon is 12.13 V, the average excitation potential is 10 V, and 80% of the ions incident on the grids become beam ions ($T_g = 0.8$). It was also assumed for simplicity that the plasma electrons were lost to the floating screen grid and the chamber wall. The mass utilization efficiency is inversely proportional to the neutral density in the thruster, which will be derived in Section 4.3.6. In the figure, the discharge loss is shown in (eV/ion), which is equivalent to watts of discharge power per ampere of beam ions (W/A). In an ideal plasma-generator case with 80% of the ions that are generated assumed to become beam current, the amount of power

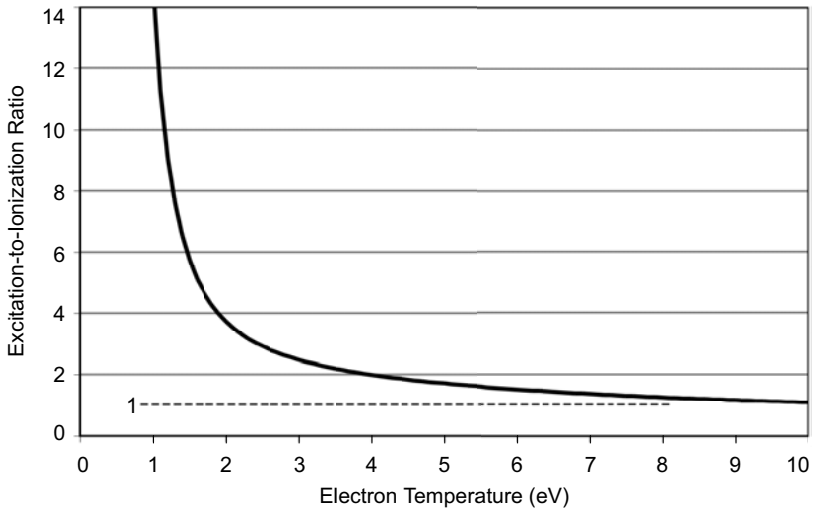

Fig. 4-4. Ratio of the excitation to ionization rate coefficients for xenon as a function of the electron temperature.

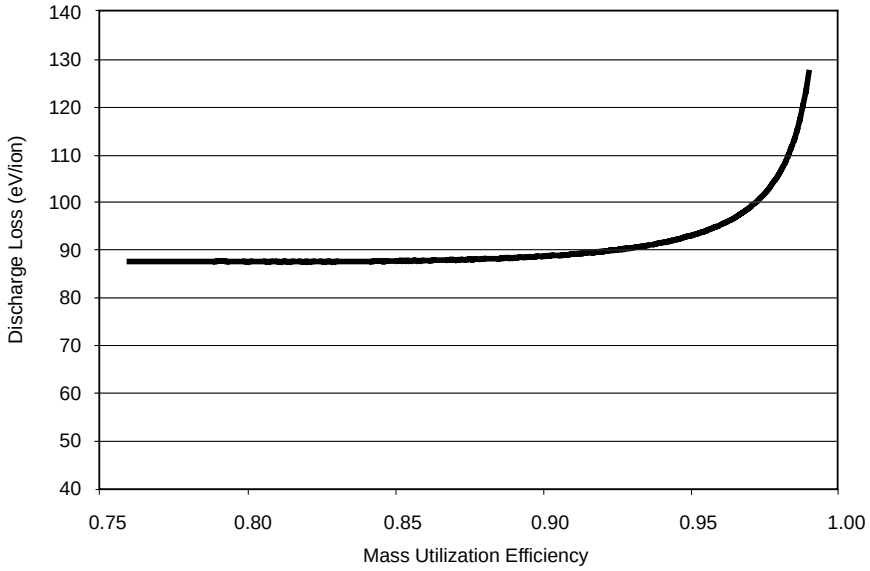

Fig. 4-5. Discharge loss for the ideal thruster example as a function of mass utilization efficiencies for a 30-cm plasma generator length.

required to produce one ampere of beam current is about 90 watts. While it only takes 12.13 eV to ionize a xenon atom, even in an idealized thruster it takes 7.5 times this energy to produce and deliver an ion into the beam due to other losses.

It is informative to see where the extra input power goes in the thruster. Figure 4-6 shows the power lost in each of the four energy loss mechanisms described above for an ideal thruster 30-cm long producing 1 A of beam current. The ionization power is constant in this case because this example was constrained to produce 1 A, and the power required per beam ampere is then (1/0.8)*12.13 = 15.1 W. The major power loss is excitation at low mass utilization where the electron temperature is low, as suggested by Fig. 4-4. The ion and electron convection losses to the wall also increase at higher mass utilization efficiencies because the neutral density is decreasing, which increases the electron temperature, raises the plasma potential, and thereby increases the energy lost per electron and ion.

Many thruster design concepts use electron confinement to improve the efficiency. The impact of this can be examined in this ideal thruster model by reducing the anode area A_a. Figure 4-7 shows the four energy-loss mechanisms for the same idealized thruster example just used, but with the effective anode area collecting electrons decreased to 1 cm^2. By conservation of charge,

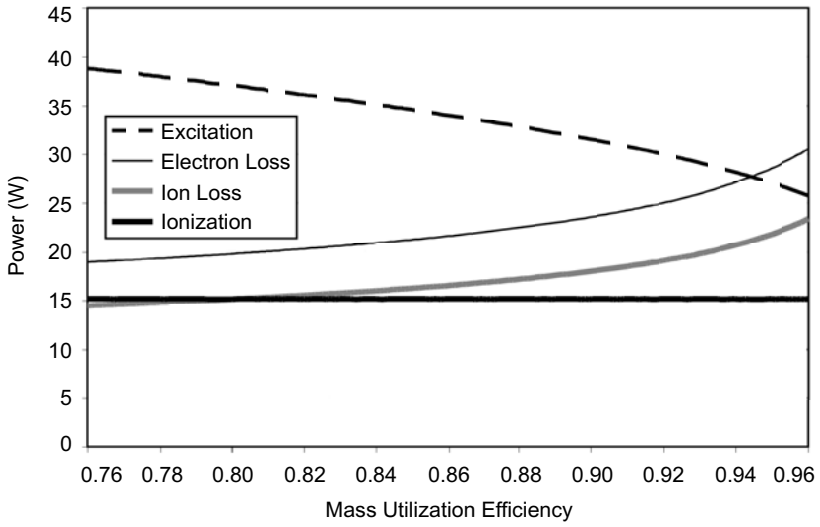

Fig. 4-6. Discharge loss for each of the energy loss mechanisms for the ideal thruster example.

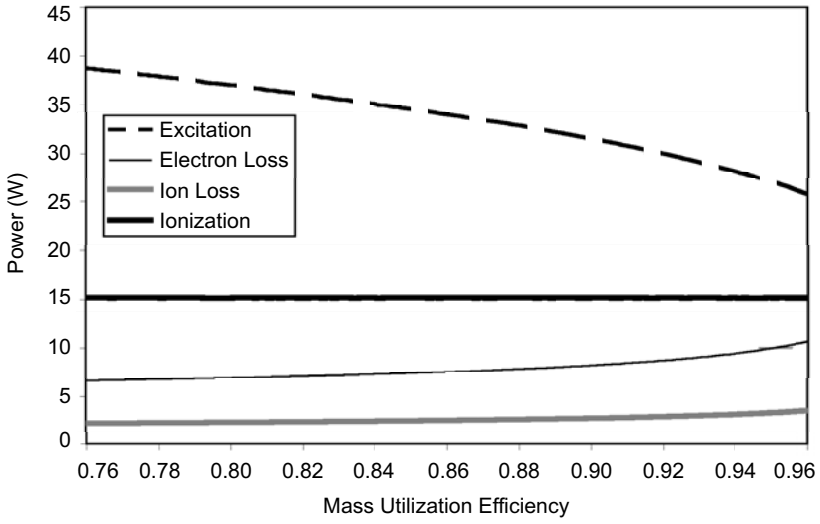

Fig. 4-7. Discharge loss for each of the energy loss mechanisms for the ideal thruster with reduced anode area.

electrons in this discharge are lost at the same rate as ions, so electron confinement does not change the number or rate of electrons lost. The reduced anode area only changes the plasma potential relative to the loss area potential in order to maintain charge balance, as seen from examining Eq. (4.2-11). This effect is clearly seen by comparing Figs. 4-6 and 4-7, where the energy loss rates for ionization and excitation have not changed with the better electron

confinement, but the energy convected out of the plasma in the form of ion and electron power to the boundaries has decreased. This is because the plasma potential described by the last term in Eq. (4.2-14) is reduced due to the smaller anode area, which reduces the ion and electron energy loss channels. This is the fundamental mechanism for making efficiency improvements (reducing the discharge loss) in plasma generators.

The idealized thruster description illustrates that the power that must be provided to produce the plasma in a thruster is large compared to that required for ionization. In terms of the total thruster efficiency, this is the majority of the "other" power in P_o in Eq. (2.5-1). In reality, the discharge loss is significantly higher than that found in this idealized example due to imperfect confinement of the ions and electrons in the thruster, and due to other loss mechanisms to be described below.

Finally, in most ion thrusters, such as electron bombardment thrusters and microwave-heated electron cyclotron resonance (ECR) thrusters, the electron distribution function is non-Maxwellian. The higher energy electrons observed in electron bombardment thrusters are often called *primaries*, and they have been found to be either monoenergetic or have some distribution in energies depending on the plasma-generator design. Primary electrons have a larger ion to excited-neutral production rate than do the plasma electrons due to their higher energy, and so even small percentages of primaries in the plasma can dominate the ionization rate. The inclusion of ionization by primary electrons in particle and energy balance models such as the one just described tends to reduce the discharge loss significantly.

4.3 DC Discharge Ion Thruster

Ion thrusters that use a DC electron-discharge plasma generator employ a hollow cathode electron source and an anode potential discharge chamber with magnetic multipole boundaries to generate the plasma and improve the ionization efficiency. Electrons extracted from the hollow cathode are injected into the discharge chamber and ionize the propellant gas introduced in the chamber. Magnetic fields applied in the discharge chamber provide confinement primarily of the energetic electrons, which increases the electron path length prior to their being lost to the anode and improves the ionization efficiency. The ions from this plasma that flow to the grids are extracted and accelerated to form the beam.

Empirical studies over the past 50 years have investigated the optimal design of the magnetic field to confine electrons and ions in thrusters. Figure 4-8 shows the evolution of the discharge chamber geometry and magnetic field shape

employed in efforts primarily aimed at improving the confinement of energetic electrons injected into the chamber from thermionic cathodes in order to more efficiently produce the plasma. Early thrusters pioneered by Kaufman utilized a solenoidal [1] or mildly divergent magnetic field [2], shown in Fig.4-8(a), which requires that electrons from the on-axis thermionic filament cathode undergo collisions in order to diffuse to the anode and complete the discharge circuit. A strongly divergent magnetic field thruster [3], shown in Fig. 4-8(b), improved the primary electron uniformity in the plasma volume and resulted in a lower discharge loss and a more uniform beam profile. This thruster introduced a baffle in front of the hollow cathode electron source to further inhibit on-axis electrons. The radial magnetic field thruster [4], shown in Fig. 4-8(c), produced very uniform plasmas and good efficiencies, as did a cusp version of the "divergent magnetic field" thruster shown in Fig. 4-8(d). The use of permanent magnet, multipole boundaries, first reported by Moore [5],

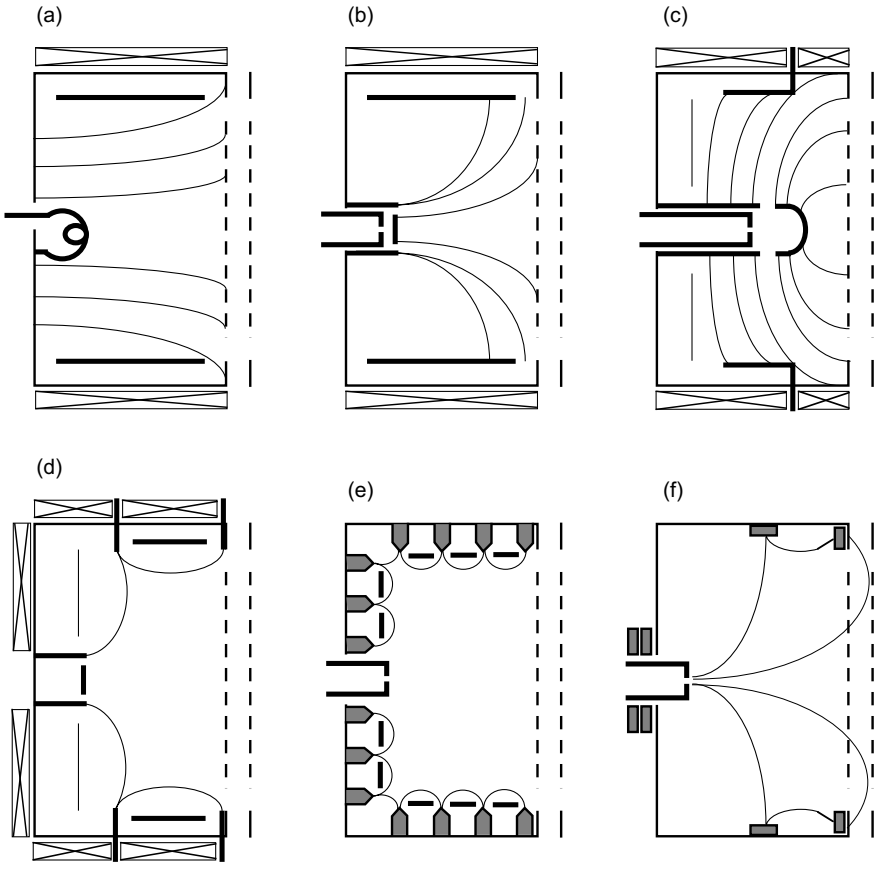

Fig. 4-8. Magnetic field types of ion thrusters: (a) mildly divergent B-field, (b) strongly divergent B-field, (c) radial field, (d) cusp field, (e) magnetic multipole field, and (f) ring-cusp fields.

created essentially a field-free region in the center of the thruster that produced uniform plasmas. The magnets in various versions of this concept were oriented in rings or in axial lines to provide plasma confinement. Moore biased the wall and magnets at cathode potential and placed the anodes inside the cusp fields, as shown in Fig. 4-8(e), to require that electrons diffuse across the field lines by collisions or turbulent transport before being lost. The permanent magnet ring-cusp thruster of Sovey [6] is shown in Fig. 4-8(f), which has become the most widely used thruster design to date.

The divergent field Kaufman ion thruster matured in the 1970s with the development of 30-cm mercury thrusters [7,8]. Kaufman thrusters are described in more detail in Section 4.4. Concerns with using mercury as the propellant resulted in the development of xenon ion thrusters [9,10], which emerged at the same time that the benefits of ring-cusp confinement geometries became apparent [6,11,12]. The design and development of the NASA Solar Electric Propulsion Technology Applications Readiness (NSTAR) [13] and Xenon Ion Propulsion System (XIPS®) [14] flight thrusters in the 1990s was based on this early work. At this time, only two of these magnetic field geometries are still used in DC ion thrusters: the multipole magnetic field ring-cusp thrusters and the divergent solenoidal magnetic fields in Kaufman-type thrusters. Ring-cusp thrusters use alternating polarity permanent magnet rings placed around the anode-potential thruster body. Energetic electrons are injected along a weak diverging magnetic field at the cathode and demagnetize sufficiently to bounce from the surface magnetic fields until they either lose their energy by collisions or find a magnetic cusp to be lost to the anode. Kaufman thrusters inject energetic electrons along a strong diverging solenoidal magnetic field with the pole-pieces typically at cathode potential and rely on cross-field diffusion of the electrons to an anode electrode placed near the cylindrical wall to produce ionization and create a stable discharge.

4.3.1 Generalized 0-D Ring-Cusp Ion Thruster Model

The idealized plasma-generator model developed in Section 4.2 is useful in describing how the discharge produces the plasma, but neglects many of the particle flows and energy transport mechanisms found in actual thrusters. The complete particle flows in a thruster discharge chamber are shown in Fig. 4-9. The primary electron current emitted by the hollow cathode, I_e, generates ions and plasma electrons. The ions flow to the accelerator structure (I_s), to the anode wall (I_{ia}), and back to the cathode (I_k). Some fraction of the primary electrons is lost directly to the anode at the magnetic cusp (I_L). The plasma electrons are also predominately lost to the anode at the cusp (I_a), with only a

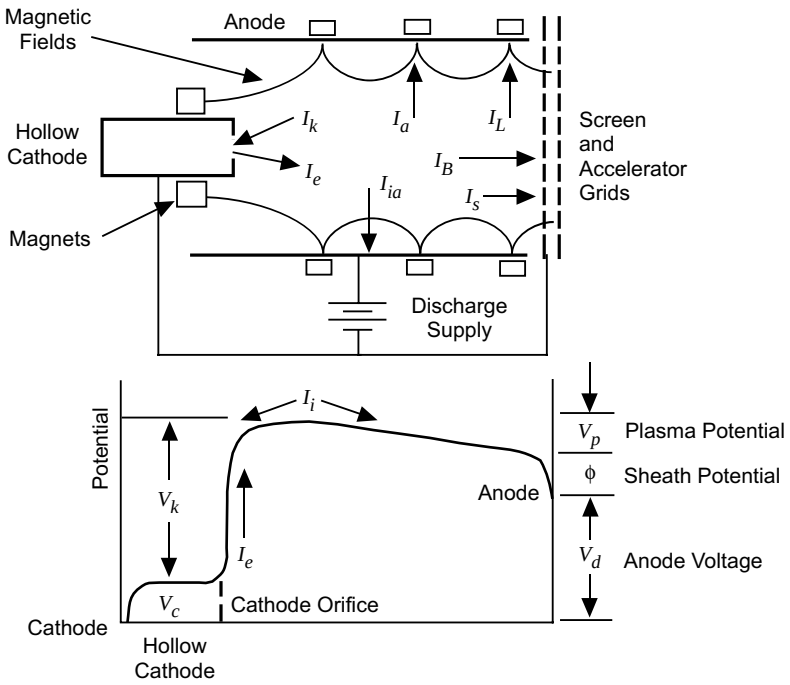

Fig. 4-9. Schematic of the thruster showing particle flows and potential distribution in the discharge chamber.

very small fraction lost across the transverse magnetic field between the cusps corresponding to the ambipolar current flows in this region.

The particle energies are determined by the potential distribution in the thruster. Figure 4-9 also schematically shows the potential in the plasma chamber. Electrons from the plasma inside the hollow cathode at a potential V_c are extracted through the orifice and into the discharge chamber where they gain energy by passing through the potential $V_k = V_d - V_c + V_p + \phi$, where V_p is the potential drop in the plasma and ϕ is the anode sheath potential. Some of these electrons cause ionization near the hollow cathode exit, which produces a higher plasma density locally near the cathode exit that must be dispersed before reaching the grid region in order to produce the desired uniform plasma profile across the grids. The potential drop V_p in the plasma, which is assumed to be uniform and quasineutral, can be reasonably approximated as $kT_e / 2e$ from the pre-sheath potential in the nearly collisionless plasma. Ions leaving the plasma then gain the energy $\varepsilon_1 = kT_e / 2e + \phi$, which was given in Eq. (4.2-10). Electrons in the tail of the Maxwellian distribution overcome the anode sheath

and are collected by the anode at the cusps, where they remove an energy per particle of $\varepsilon_e = (2kT_e / e + \phi)$, which is given in Eq. (4.2-9) and derived in Appendix C.

Analytic models of the discharge chamber performance in ion thrusters have been described in the literature for many years [15–17]. The first comprehensive model of the discharge chamber performance using particle and energy balance equations in ring-cusp thrusters was developed by Brophy and Wilbur [18,19] in 1984. In Brophy's model, volume-averaged particle and energy balance equations including primary electrons were used to derive expressions for the discharge loss as a function of the mass utilization efficiency in the thruster. Brophy's model was extended by Goebel [20,21] to include electrostatic ion confinement, primary confinement and thermalization, the anode sheath [22], and hollow cathode effects. This model utilizes magnetic field parameters obtained from a magnetic field solver that accurately models the magnetic boundary. Since the model assumes a uniform plasma in the volume inside the magnetic confinement in the discharge chamber, it is sometimes called a 0-dimensional (0-D) model.

The 0-D discharge chamber model to be described here [21] self-consistently calculates the neutral gas density, electron temperature, primary electron density, plasma density, plasma potential, discharge current, and ion fluxes to the boundaries of the discharge chamber. While the assumption of uniform plasma is not particularly accurate near the cathode plume, the majority of the plasma in the discharge chamber is relatively uniform, and the model predictions agree well with experimental results. The 0-D model solves for discharge loss as a function of the mass utilization efficiency, which is useful in plotting performance curves that best characterize the discharge chamber performance.

The particle flows and potential distribution in the thruster used in the 0-D model are shown schematically in Fig. 4-9. Mono-energetic primary electrons with a current I_e are assumed to be emitted from the hollow cathode orifice into the discharge chamber, where they ionize the background gas to produce a uniform plasma. Electrons produced in the ionization process and primary electrons that have thermalized with the plasma electrons create a Maxwellian plasma electron population that also contributes to the ionization. Due to the relatively high magnetic field produced by the magnets near the wall, the electron Larmor radius is much smaller than the dimensions of the discharge chamber, and both primary and plasma electrons are considered to be reflected from the boundary region between the magnetic cusps. The primary and plasma electrons can be lost at the magnetic cusps because the magnetic field lines are

essentially perpendicular to the surface. The number of electrons lost at the cusp depends on the local sheath potential and the effective loss area at the cusp. Ions produced in the discharge chamber can flow back to the hollow cathode, to the anode wall, or to the plane of the accelerator. At the accelerator, these ions are either intercepted and collected by the screen electrode with an effective transparency, T_g, or are extracted from the plasma through the grids to become beam ions. The screen grid transparency depends on the optical transparency of the grid and the penetration of the high voltage fields from the accelerator region into the screen apertures. While this transparency is an input to the discharge model, it is calculated by the ion optics codes described in Chapter 5.

In this model, the high-voltage power supply that accelerates the ions, called the screen supply, is connected to the anode. This means that the ions fall from the average plasma potential in the discharge chamber to form the beam. It is also possible to connect the screen supply to the screen and cathode, which means that the ion current in the beam must pass through the discharge supply. This changes the algebra slightly in calculating the discharge performance, but it does not change the results. The components of the particle and energy balance model are described in the following sections.

4.3.2 Magnetic Multipole Boundaries

Ring-cusp ion thrusters use alternating polarity permanent magnet rings oriented perpendicularly to the thruster axis, with the number of rings selected and optimized for different size thrusters [20]. This configuration provides magnetic confinement of the electrons with finite loss at the magnetic cusps, and electrostatic confinement of the ions from the anode wall due to the quasi-ambipolar potentials at the boundary from the transverse magnetic fields. Line-cusp thrusters also use high field magnets, but the magnets are configured in alternating polarity axial lines that run along the chamber wall. Asymmetries at the ends of the line cusps cause plasma losses and difficulties in producing a uniform symmetric field at the cathode exit, which adversely affects the electron confinement and thruster efficiency. Ring-cusp thrusters are the most commonly used discharge chamber design at this time due to their ability to produce high efficiency and uniform plasmas at the ion accelerator surface if properly designed.

A schematic representation of a section of a ring cusp magnetic multipole boundary is shown in Fig. 4-10. In this view, a cut along the axis through a six-ring boundary at the wall is made, leaving the ends of the alternating magnets visible. The magnetic field lines terminate at the magnet face, resulting in a cusp magnetic field with field lines perpendicular to the wall at the magnet.

Electrons that are incident in this area will be either reflected by the magnetic mirror, electrostatically repelled by the sheath potential, or lost directly to the anode. Electrons that are incident between the cusps encounter a transverse magnetic field and are reflected from the boundary. The contours of constant magnetic field shown on the right in Fig. 4-10 illustrate that the total field is essentially constant across the boundary at a distance sufficiently above the magnets, although the component of the field is changing from purely perpendicular at the cusp to purely parallel between the cusps.

An analysis of the magnetic field strength for various multipole boundaries was published by Forrester [23] and discussed by Lieberman [24]. Since the divergence of the magnetic field is zero, the field satisfies Laplace's equation, and the solution for the lowest-order mode at a distance from the magnets greater than the magnet separation can be expressed by a Fourier series. This gives a magnetic field strength above the magnet array described by

$$B_y(x,y) = \frac{\pi w B_o}{2d} \cos\left(\frac{\pi x}{d}\right) e^{-\pi y/d}, \qquad (4.3\text{-}1)$$

where B_o is the magnetic field at the surface of the magnet, d is the distance between the magnet centers, w is the magnet width, and the y-direction is perpendicular to the wall in Fig. 4-10. Due to localized magnet positions, the field has the periodic cosine behavior along the surface of the wall illustrated in the figure. In addition, the magnetic field decreases exponentially away from the wall all along the boundary.

At the cusp, the field actually decreases as $1/d^2$ due to the dipole nature of the permanent magnet. This rapid decrease in the field moving away from the magnet illustrates the importance of placing the magnets as close to the plasma

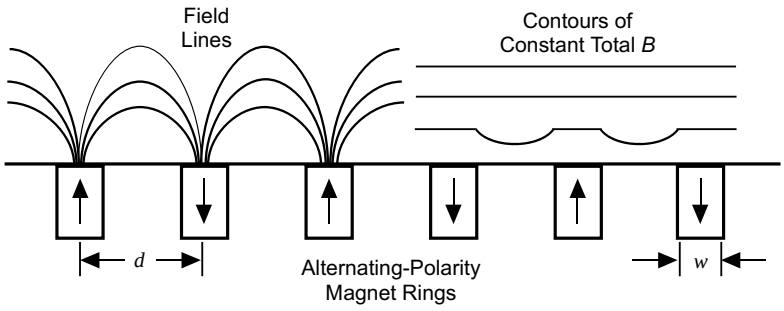

Fig. 4-10. Cross section (side) view of a six-ring-cusp magnetic multipole boundary showing the magnetic field lines and examples of contours of constant magnetic field.

as possible to maximize the field strength inside the discharge chamber for a given magnet size in order to provide sufficient field strength for primary and secondary electron confinement at the wall. Between the cusps, the dipole characteristics of the local field forces the field lines to wrap back around the magnets, which causes the magnetic field strength to have a maximum at a distance $y = 0.29*d$ from the wall, which will be derived in Section 4.3.4. The transverse maximum field strength produced between the cusps is important to provide electron and ion confinement, which improves the thruster efficiency.

While analytic solutions to the magnetic field provide insight into the field structure, the availability of commercial computer codes to calculate the fields accurately makes it much simpler to model the entire ring-cusp field. For example, Fig. 4-11 shows the contours of constant magnetic field measured and calculated using Maxwell three-dimensional (3-D) magnetic field solver [25] for the Nuclear Electric Xenon Ion Thruster System (NEXIS) [20] with six ring cusps. The measured and calculated values are within the measurement error. This type of plot shows clearly the localized surface-field characteristic of magnetic multipole boundaries, which leaves the majority of the inner volume essentially magnetic-field free. A large field-free region design significantly enhances the plasma uniformity and ion current density profile [20,26]. In this case, the 60-gauss magnetic field contour is closed throughout the inside surface of the thruster, which will be shown in the next section to provide good plasma confinement at the wall.

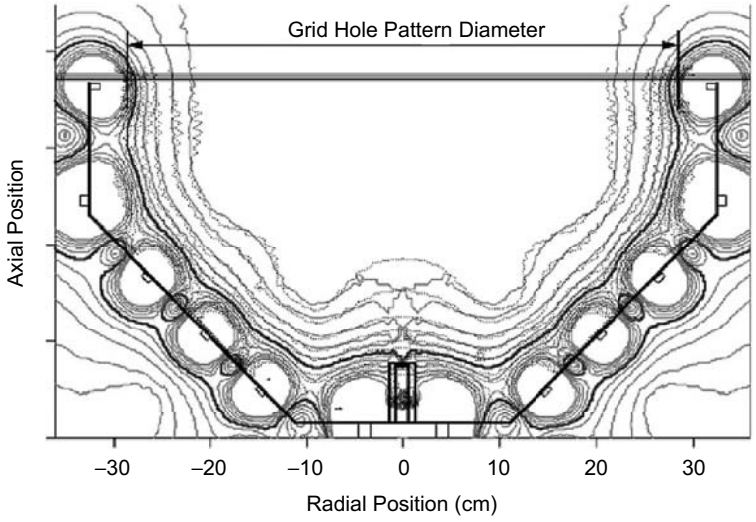

Fig. 4-11. Comparison of measured (dashed) and calculated (solid) magnetic field contours in the six-ring NEXIS thruster [20].

4.3.3 Electron Confinement

The primary electrons are injected into the discharge chamber from the hollow cathode. The discharge chamber can be viewed as a volume with reflecting boundaries and discrete loss areas for the electrons at the cusps where the magnetic fields lines are nearly perpendicular to the surface. The primary electrons then effectively bounce around in the chamber until they are either lost directly to the anode wall by encountering the finite loss area at the cusps, make an ionization or excitation collision, or are thermalized by coulomb interactions with the plasma electrons. The primary current lost directly to the anode cusps is given by

$$I_L = n_p e v_p A_p , \tag{4.3-2}$$

where n_p is the primary electron density, v_p is the primary electron velocity, and A_p is the loss area for the primaries.

The loss area for primary electrons at the cusp [27] is given by

$$A_p = 2\, r_p\, L_c = \frac{2}{B}\sqrt{\frac{2mv_p}{e}}\, L_c , \tag{4.3-3}$$

where r_p is the primary electron Larmor radius, B is the magnetic field strength at the cusp at the anode wall, v_p is the primary electron velocity, e is the electron charge, and L_c is the total length of the magnetic cusps (sum of the length of the cusps).

Using a simple probabilistic analysis, the mean primary electron confinement time can be estimated by

$$\tau_p = \frac{V}{v_p\, A_p} , \tag{4.3-4}$$

where V is the volume of the discharge chamber. The mean primary electron path length prior to finding a cusp and being lost to the wall is $L = v_p * \tau_p$. Likewise, the ionization mean free path is $\lambda = 1/n_o\sigma$, where σ represents the total inelastic collision cross section for the primary electrons. The probability that a primary electron will make a collision and not be directly lost to the anode is then

$$P = \left[1 - \exp^{-n_o \sigma L}\right] = \left[1 - \exp^{\left(-n_o \sigma V / A_p\right)}\right]. \qquad (4.3\text{-}5)$$

By providing strong magnetic field strengths at the cusp to minimize the primary loss area, the probability of a primary electron being lost directly to the anode can be made very small. Similarly, ion thrusters with large volumes and/or operated at higher internal gas densities will cause the primary electrons to undergo collisions and thermalization prior to being lost directly to the anode. Minimizing the energy loss associated with primaries being lost before making a collision in this way serves to maximize the efficiency of the thruster.

An example of the probability of a primary electron making a collision before finding a cusp is shown in Fig. 4-12 for the case of the NEXIS thruster designed with either 4 or 6 cusps [20]. For the design with 6 cusps, it is necessary to have cusp-field strengths approaching 2000 G at the surface of the anode in order to minimize primary loss. Designs with a smaller number of ring cusps, corresponding to a smaller primary anode collection area from Eq. (4.3-3), require less magnetic field strength to achieve the same benefit. However, it will be shown later that the number of cusps affects efficiency and uniformity, and that maximizing the probability of a primary making a collision before being lost is only one of the trade-offs in designing an ion thruster.

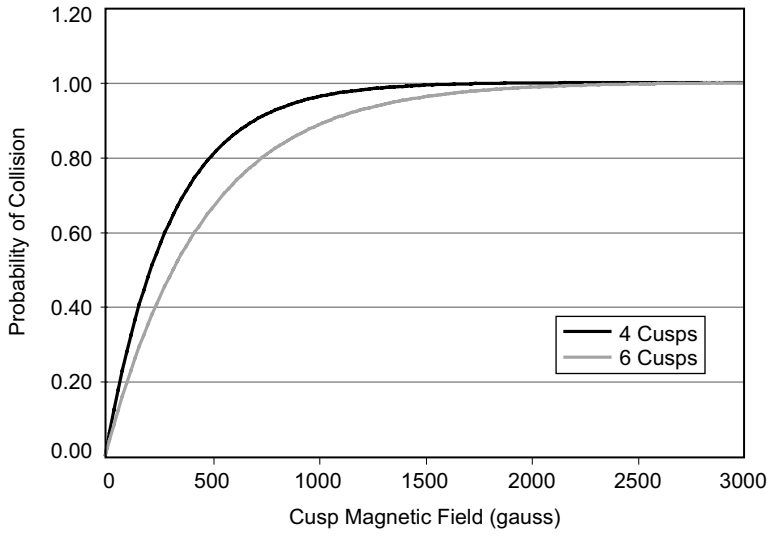

Fig. 4-12. Probability of primary electrons making a collision before being lost to the anode as a function of the cusp magnetic field strength for the NEXIS thruster design [20].

Since the primary electron current lost directly to the anode is generally minimized for best efficiency, the discharge current is carried to the anode mainly by the plasma electrons. The plasma electrons are almost exclusively lost at the magnetic cusps, but their motion is affected by the presence of ions that also penetrate the cusp. Therefore, ions and electrons are lost to a hybrid anode area [27] at the cusp given by

$$A_a = 4\, r_h\, L_c = 4\, \sqrt{r_e r_i}\; L_c\,, \tag{4.3-6}$$

where r_h is the hybrid Larmor radius, r_e is the electron Larmor radius, and r_i is the ion Larmor radius. The flux of plasma electrons, I_a, that overcomes the sheath at the anode is

$$I_a = \frac{1}{4}\left(\frac{8kT_e}{\pi\, m}\right)^{1/2} e\, n_e\, A_a\;\; \exp^{-e\phi/kT_e}\,, \tag{4.3-7}$$

where ϕ is the local plasma potential relative to the anode (essentially the anode sheath potential).

The plasma in the discharge chamber obeys particle conservation in that the current injected and produced in the discharge must equal the total current that leaves the discharge:

$$\sum\left(I_{\text{injected}} + I_{\text{produced}}\right) = \sum I_{\text{out}}\,. \tag{4.3-8}$$

The current injected into the discharge volume is the primary electron current, and the current produced is the ion and electron pairs from each ionization collision. The current lost to the anode is the sum of the direct primary loss, the plasma electron loss, and a fraction of the ion loss. There is also ion current lost to cathode potential surfaces and the accelerator structure from the balance of the ions produced in the discharge. The plasma potential will adjust itself such that the total electron current to the anode is equal to the total ion current out of the discharge. It will be shown in the following sections that changing the anode area via the magnet strength or number of magnet rings will change the plasma potential relative to the anode (essentially the anode sheath voltage), which affects both the energy loss though the sheath and the stability of the discharge.

4.3.4 Ion Confinement at the Anode Wall

Ions are typically unmagnetized in ion thruster discharge chambers because the magnetic field is relatively low throughout the bulk of the discharge chamber,

which results in a large ion Larmor radius compared to the thruster dimensions. For an unmagnetized plasma, the ion current flowing out the plasma volume in any direction is given by the Bohm current:

$$I_i = \frac{1}{2} n_i e \sqrt{\frac{kT_e}{M}} A , \tag{4.3-9}$$

where n_i is the ion density in the center of the discharge and *A* is the total ion loss area. The Bohm current also describes ion flow along magnetic field lines, which will be useful later in discussing other plasma generator types.

The electrons may or may not be magnetized in the main discharge chamber volume, but they are strongly affected by the magnet fields near the boundary in ring-cusp thrusters. The magnetized electrons then influence the ion motion near the boundaries by electrostatic effects. This causes the ion loss to the cusps to be the Bohm current to the hybrid area, given by Eq. (4.3-6), and a reduction in the Bohm current to the wall area between the cusps due to the ambipolar potentials that develop there. Since the cusp area is small compared to the rest of the anode surface area facing the plasma, the ion current to the hybrid cusp area often can be neglected. However, between the cusps the loss area is significant, and it is possible to analyze the electron and ion transport across the magnetic field to calculate the reduction in the ion velocity caused by the reduced transverse electron drift speed. This is then used to calculate the rate of ion loss to the anode compared to the unmagnetized Bohm current to the walls.

Ring cusp thrusters are designed with various numbers of rings, distances betweens the rings, and magnet sizes that determine the magnetic field strength in the discharge chamber transverse to the wall. The quasi-neutral plasma flow across this magnetic field to the wall is described by the diffusion equation with an ambipolar diffusion coefficient. Ambipolar diffusion across a magnetic field was analyzed in Section 3.6.3.2. The transverse ion velocity was found to be

$$v_i = \frac{\mu_e}{\left(1 + \mu_e^2 B^2 - \dfrac{\nu_{ei}}{\nu_e}\right)} \left(E + \frac{kT_e}{e} \frac{\nabla n}{n} \right). \tag{4.3-10}$$

Setting the transverse electric field *E* in the plasma to zero in Eq. (4.3-10) gives the case where the ambipolar electric field exactly cancels the pre-sheath electric field that normally accelerates the ions to the Bohm velocity. In this case, the ion velocity is just the ion thermal velocity $\left(\approx \sqrt{kT_i/M}\right)$, and the value of *B* in Eq. (4.3-10) is the minimum transverse magnetic field required to

reduce the electron mobility sufficiently to produce this effect. Due to the smaller ion velocity, the flux of ions passing through the transverse magnetic field is greatly reduced compared to the Bohm current. The ion flux that does reach the wall is finally accelerated to the Bohm velocity close to the anode wall to satisfy the sheath criterion. Ions are conserved in this model because ions that are inhibited from flowing to the anode wall due to the transverse fields instead flow axially toward the grids where there is no confinement.

However, it is not necessary to limit this analysis to the case of $E = 0$. If the magnetic field is smaller than the critical B that causes $E = 0$, then the transverse electron mobility increases and a finite electric field exists in the magnetic diffusion length l. The ions fall through whatever potential difference is set up by this electric field, which means that the ions are accelerated to an energy given by

$$\frac{1}{2} M v_i^2 = e\, E \cdot l. \tag{4.3-11}$$

The ambipolar flow in the transverse magnetic field changes the electric field magnitude in the pre-sheath region and reduces the acceleration of the ions toward the wall. In the limit of no magnetic field, the electric field must accelerate the ions to the Bohm velocity, which results in a net electric field in the plasma-edge region limited to

$$E = -\frac{M v_i^2}{e\, l}. \tag{4.3-12}$$

Note that the electric field sign must be negative for the ion flow in this region. Using Eq. (4.3-12) in Eq. (4.3-10), the minimum magnetic field to produce an ion velocity of v_i is

$$B = \frac{\nu_e m}{e} \sqrt{\frac{\left(kT_e - M v_i^2\right)}{v_i m \nu_e \ell} - \left(\frac{\nu}{1+\nu}\right)}, \tag{4.3-13}$$

where $\nu = \nu_{en} / \nu_{ei}$, and $kT_e \nabla n / en$ is approximately kT_e / el for l representing the length the ions travel radially in the transverse magnetic field between the cusps. The value of l can be estimated from calculations of the transverse magnetic field versus the distance from the wall between the cusps, and is usually on the order of 2 to 3 cm.

Alternatively, the modified electric field given in Eq. (4.3-12) can be inserted into Eq. (4.3-10) to produce an expression for the transverse ion velocity:

$$v_i^2 + \frac{el}{\mu_e M}\left(1 + {\mu_e}^2 B^2 - \frac{\nu_{ei}}{\nu_e}\right) v_i - \frac{kT_e}{M} = 0. \tag{4.3-14}$$

This quadratic equation can be easily solved to give

$$v_i = \frac{1}{2}\sqrt{\left[\frac{e\ell}{M\mu_e}\left(1 + \mu_e^2 B^2 - \frac{\nu_{ei}}{\nu_e}\right)\right]^2 + \frac{4kT_e}{M}} - \left[\frac{e\ell}{2M\mu_e}\left(1 + \mu_e^2 B^2 - \frac{\nu_{ei}}{\nu_e}\right)\right]. \tag{4.3-15}$$

The collision frequencies ($\nu_e = \nu_{en} + \nu_{ei}$ and $\nu = \nu_{en} / \nu_{ei}$) in these equations for xenon plasmas were given in Chapter 3, where the electron-neutral collision frequency is given in Eq. (3.6-12) and the electron-ion collision frequency is given in Eq. (3.6-14). It is possible to show that in the limit that *B* goes to zero and the flow is essentially collisionless, Eq. (4.3-15) reverts to the Bohm velocity.

Defining an ion confinement factor

$$f_c \equiv \frac{v_i}{v_{\text{Bohm}}}, \tag{4.3-16}$$

and since the Bohm velocity is $v_{\text{Bohm}} = \sqrt{kT_e / M}$, it is a simple matter to calculate the reduction in the expected flux of ions going to the anode due to the reduction in the Bohm velocity at a given magnetic field strength *B*. The ion current transverse to the magnetic field between the cusps to the anode is then given by

$$I_{ia} = \frac{1}{2} n_i \, e \sqrt{\frac{kT_e}{M}} \, A_{as} f_c, \tag{4.3-17}$$

where A_{as} is the total surface area of the anode exposed to the plasma.

There are two issues with using Eq. (4.3-17) to evaluate ion loss rate reduction between the cusps. First, the magnetic field in the ring-cusp geometry is not transverse to the wall everywhere. Near the cusp, the field transitions from

parallel to perpendicular to the wall, where the analysis above does not apply. However, the magnetic field strength in this region increases rapidly near the magnets and some fraction of the plasma electrons is reflected from the magnetic mirror. This serves to retard the ion flux electrostatically in a manner similar to the ambipolar diffusion case between the cusps described above. Ultimately, the ions are lost at the cusp with the Bohm current to the hybrid area, and it is usually found that the transition to this unimpeded ion flow to the wall occurs over an area that is small compared to the total area between the cusps.

The second issue with using Eq. (4.3-17) is that the diffusion thickness l is not known. However, this can be estimated for ring-cusp thrusters using a dipole model for the magnets. Consider the case of two rows of opposite polarity magnets, which is illustrated in part of Fig. 4-10. Each magnet has a dipole strength M per unit length, and the magnets are separated in the x-direction by a distance d. The magnetic field along the line perpendicular to the midline between the magnets is

$$\left|\mathbf{B}^{+}(y)\right| = \frac{q}{r} = \frac{q}{\sqrt{\frac{d^2}{4} + (y-\delta)^2}}, \tag{4.3-18}$$

where r is the length of the line from the point on the midline to the magnet, q is the number of magnetic dipoles, and δ is the half height of the magnet. The magnetic field on the centerline between the magnets has only an x-component. The x-component of the field from one magnet (positive polarity) is given by

$$B_x^{+}(y) = \left|\mathbf{B}^{+}(y)\right|\cos\theta = \frac{q\frac{d}{2}}{r^2} = \frac{q\frac{d}{2}}{\frac{d^2}{4} + (y-\delta)^2}. \tag{4.3-19}$$

The field in the x-direction from both magnets is then

$$B_x(y) = \frac{q\,d}{\frac{d^2}{4} + (y-\delta)^2} - \frac{q\,d}{\frac{d^2}{4} + (y+\delta)^2}, \tag{4.3-20}$$

and so the total field on the center line is

$$B(y) = \frac{2(2q\delta)yd}{\left(\frac{d^2}{4} + y^2\right)^2} = \frac{2Myd}{\left(\frac{d^2}{4} + y^2\right)^2}, \tag{4.3-21}$$

where the magnetization M is the number of magnetic dipoles times the length of the magnet.

The maximum magnetic field strength between the magnets, found from Eq. (4.3-21), then occurs at

$$y = \frac{d}{2\sqrt{3}} = 0.29d \approx l. \tag{4.3-22}$$

It is assumed that the diffusion length l is roughly this distance. This is not an unreasonable approximation, as illustrated in Fig. 4-13. The magnetic field decreases on each side of the maximum, but is nearly the full value over the length of about 0.3 of the distance between the magnets.

The maximum transverse field strength along the centerline between the magnets, often called the "saddle-point" field, can also be calculated from this simple derivation. Using Eq. (4.3-22) in Eq. (4.3-21), the maximum magnetic field is

$$B(y_{\max}) = 5.2\frac{M}{d^2}. \tag{4.3-23}$$

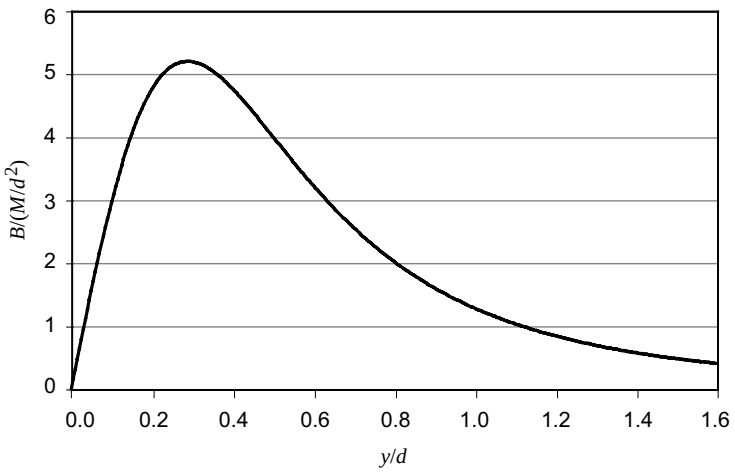

Fig. 4-13. Magnetic field strength as a function of distance above the magnets.

The dipole strength per unit length is

$$M = \frac{B_r V_m}{4\pi w}, \tag{4.3-24}$$

where B_r is the residual magnetic field of the magnet, V_m is the volume of the magnet, and w is the width of the magnet. For example, for two rows of magnets that have a residual magnetic field of 10,000 gauss, a volume per width of 0.6 cm^2, and a separation of 10 cm, the maximum transverse magnetic field is 24.8 gauss and occurs at a distance of 2.9 cm above the boundary.

As an example of the ion loss rate to the anode, the fraction of the Bohm current to the anode (I_{ia} / I_{Bohm}) is plotted in Fig. 4-14 as a function of the magnetic field at the saddle point for the NSTAR ion thruster [13]. At zero transverse magnetic field, the ion flux to the anode is the Bohm current. As the transverse field increases and reduces the electron mobility, the ions are slowed and the current loss decreases. In the NSTAR design, the last closed magnetic contour is about 20 gauss, and so roughly half of the ions initially headed radially toward the anode are lost. For closed magnetic field contours of at least about 50 gauss, the ion loss to the anode is reduced by nearly a factor of 10 compared to the unmagnetized Bohm current. This can make a significant difference in the efficiency of the plasma generator and the amount of discharge power required to produce the beam ions. Even though the ions are unmagnetized in these thrusters, it is clear that ambipolar effects make the ring-cusp magnetic fields effective in reducing the ion loss to the walls.

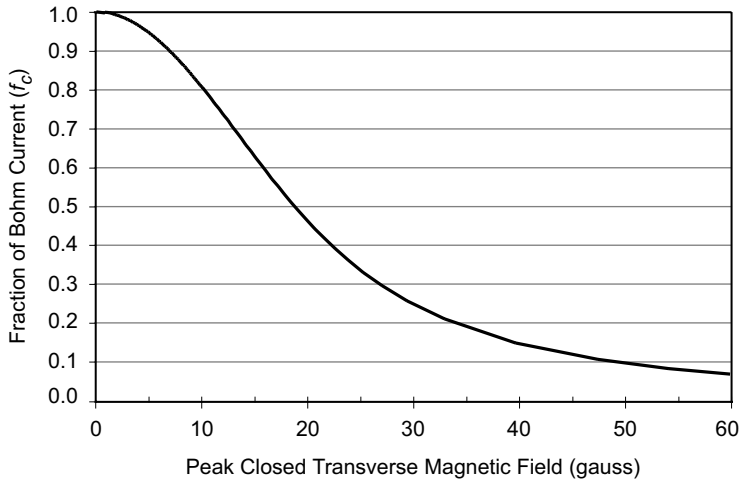

Fig. 4-14. Fraction of the Bohm current density to the anode wall as a function of the transverse magnetic field strength for the NSTAR ion thruster [13].

4.3.5 Ion and Excited Neutral Production

Ions in the discharge chamber are produced by both the primary electrons and by the tail of the Maxwellian distribution of the plasma electrons. The total number of ions produced in the discharge in particles per second is given by

$$I_p = n_o n_e \langle \sigma_i v_e \rangle V + n_o n_p \langle \sigma_i v_p \rangle V , \qquad (4.3\text{-}25)$$

where n_o is the neutral atom density, n_e is the plasma electron density, σ_1 is the ionization cross section, v_e is the plasma electron velocity, V is the plasma volume inside the discharge chamber, n_p is the primary electron density, and v_p is the primary electron velocity. The terms in the brackets are the ionization cross section averaged over the distribution of electron energies, which is usually called the reaction rate coefficient.

An example of ionization and excitation cross sections [28,29] used for electron impact on xenon is shown in Fig. 4-15. If it is assumed that the primary electrons are monoenergetic, then the reaction rate coefficient in Eq. (4.3-25) for primary ionization is just the cross section in Fig. 4-15 times the corresponding primary electron velocity. These data are listed for xenon in Appendix D. If the primaries have a distribution in energy, then the cross section must be averaged over that distribution. For Maxwellian electrons, this is calculated for xenon and listed in Appendix E.

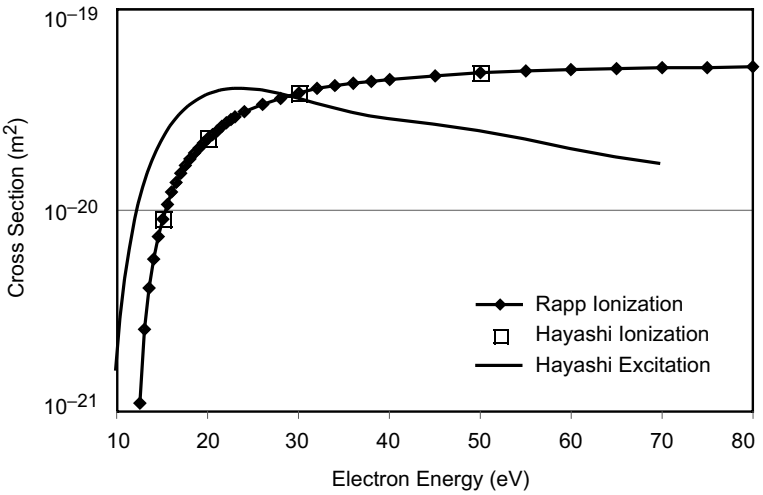

Fig. 4-15. Ionization and excitation cross sections for xenon [28,29].

Excited neutrals are also produced by both the primary electrons and the tail of the Maxwellian distribution of the plasma electrons. The total number of exited neutrals produced in the discharge in particles per second is given by

$$I^* = n_o n_e \left\langle \sigma_* v_e \right\rangle V + n_o n_p \left\langle \sigma_* v_p \right\rangle V \,, \qquad (4.3\text{-}26)$$

where σ_* is the excitation cross section. Again, the excitation cross section is averaged over the distribution in electron energies to produce the reaction rate coefficients in the brackets. The reaction rate coefficients calculated by averaging the ionization and excitation cross sections over the Maxwellian energy distribution are shown in Fig. 4-16 and listed in Appendix E. The rate of excitation is seen to exceed that of ionization for low electron temperatures (below about 9 eV). The ratio of excitation to ionization reaction rates for xenon is shown in Fig. 4-4. As previously described, at low electron temperatures, a significant amount of the energy in the discharge goes into excitation of the neutrals at the expense of ionization. This is one of the many reasons that the cost of producing an ion in ion thrusters is usually over ten times the ionization potential.

For inert gas propellants commonly used in ion thrusters, the second ionization potential is on the order of twice the first ionization potential. For example, the first ionization potential of xenon is 12.13 eV, and the second ionization potential is 21.2 eV. DC electron discharges that have electron energies in excess of 21.2 V can produce a significant number of double ions. In addition,

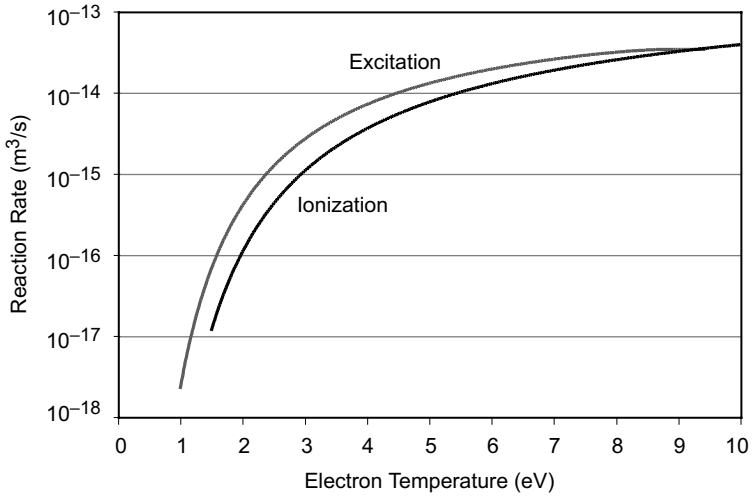

Fig. 4-16. Ionization and excitation reaction rates averaged over a Maxwellian electron distribution in a xenon plasma.

the tail of the Maxwellian electron distribution will also contain electrons with an energy that exceeds the second ionization potential, and significant numbers of double ions will be produced if the electron temperature in the discharge chamber is high.

The generation rate of double ions is determined in the same manner as single ions, discussed above, with different ionization cross sections [30]. The density of the double ions is determined by the continuity equation for that species,

$$\frac{dn^{++}}{dt} + \nabla \cdot \left(n^{++} v^{+} \sqrt{2} \right) = \dot{n}^{++}, \tag{4.3-27}$$

where it is assumed that due to the double ions' charge, the velocity will be increased over the singly ionized species by a square root of two. Defining the rate of double-ion production compared to single-ion production as

$$R^{++} = \frac{n^{++}}{n^{+}}, \tag{4.3-28}$$

the beam current density of single ions from the discharge plasma boundary through the ion optics (again with a transparency T_g) is

$$J_i^{+} = n^{+} e v_B^{+} T = n_i e v_B^{+} T_g \left(1 - R^{++} \right), \tag{4.3-29}$$

where n_i is the total ion density. The double-ion current density is likewise

$$J_i^{++} = n^{++} (2e) \left(\sqrt{2} v_B^{+} \right) T_g = \sqrt{8} n_i e v_B^{+} T_g R^{++}. \tag{4.3-30}$$

The total ion beam current is then the sum of the singly and doubly ionized particle currents.

As discussed in Chapter 2, the discharge propellant efficiency is the ratio of the propellant that becomes beam ions (of any charge) to the rate of propellant flow into the discharge chamber. Considering the effect of double ions, the propellant efficiency of the discharge chamber is then

$$\eta_{md} = \left(J_B^{+} + \frac{J_B^{++}}{2} \right) \frac{A_g}{e \dot{m}_d}, \tag{4.3-31}$$

where $\dot{m}_d$ is the mass flow into the discharge chamber and A_g is the area of the grids. In the event that there is a significant double-ion content in the discharge plasma, the beam current and the discharge chamber mass utilization efficiency must be corrected using these equations.

4.3.6 Neutral and Primary Densities in the Discharge Chamber

The ion and excited neutral production rates described by Eqs. (4.3-25) and (4.3-26) require knowledge of the neutral gas density in the discharge chamber. The neutral gas flow that escapes the chamber (the unionized propellant) is simply the gas injected into the discharge chamber minus the gas particles that are ionized and extracted to form the ion beam:

$$Q_{\text{out}} = Q_{\text{in}} - \frac{I_b}{e}. \tag{4.3-32}$$

The neutral gas that leaks through the grid is the neutral flux on the grids (in particles per second) times the grid optical transparency T_a and a conductance reduction term η_c known as the Clausing factor [31]:

$$Q_{\text{out}} = \frac{1}{4} n_o v_o A_g T_a \eta_c, \tag{4.3-33}$$

where v_o is the neutral gas velocity, A_g is the grid area, and η_c is the Clausing factor. The Clausing factor represents the reduced conductance of the grids for finite grid thicknesses and results from Clausing's original work on gas flow restriction in short tubes. For typical grid apertures with small thickness-to-length ratios, the Clausing factor must be calculated using Monte Carlo techniques, an example of which is given in Appendix G. In general, ion thruster grids will have Clausing factors on the order of 0.5.

The mass utilization efficiency of the thruster discharge chamber is defined as

$$\eta_{md} = \frac{I_b}{Q_{\text{in}} e}. \tag{4.3-34}$$

Equating Eqs. (4.3-32) and (4.3-33), using Eq. (4.3-34), and solving for the neutral gas density in the discharge chamber gives

$$n_o = \frac{4Q_{\text{in}}(1-\eta_{md})}{v_o A_g T_a \eta_c} = \frac{4\ I_B}{v_o e A_g T_a \eta_c} \frac{(1-\eta_{md})}{\eta_{md}}. \tag{4.3-35}$$

Flow is usually given in standard cubic centimeters per minute (sccm) or mg/s, and conversions from these units to number of particles per second, useful in Eq. (4.3-35), are given in Appendix B. The neutral pressure in the discharge chamber during operation of the thruster can also be found using this expression and the conversion from density to pressure given in Eq. (2.7-2), if the neutral gas temperature is known. In general, the neutral gas atoms collide with the anode wall and grids several times before being lost, and so the neutral gas can be assumed to have the average temperature of the thruster body in contact with the plasma. This temperature typically ranges from 200 to 300 deg C for operating thrusters.

The electron temperature in the discharge chamber can be found using particle balance of the ions. The total ion production rate, given by Eq. (4.3-25), must equal the total ion loss rate. The ion loss rate is given by the Bohm current in Eq. (4.3-9) with the area A representing the sum of all the surfaces that collect ions (cathode, anode, and grids), with the appropriate confinement factor f_c found in Eq. (4.3-16) multiplied by the anode surface area. Equating Eqs. (4.3-25) and (4.3-9) and using Eq. (4.3-35) for the neutral density gives

$$\frac{\sqrt{\frac{kT_e}{M}}}{\langle \sigma_i v_e \rangle V + \frac{n_p}{n_e} \langle \sigma_i v_p \rangle V} = \frac{2 n_o V}{A_i} = \frac{8 V \, Q_{\text{in}} (1 - \eta_{md})}{v_o A_g A_i T_a \eta_c} . \qquad (4.3\text{-}36)$$

If the total flow into the discharge chamber and the mass utilization efficiency are specified, and the primary electron density is calculated as described below, then Eq. (4.3-36) can be solved for the electron temperature. This is because the ionization and excitation reaction rate coefficients are functions of the electron temperature. Alternatively, if the beam current is specified, then the right-hand side of Eq. (4.3-35) can be used in Eq. (4.3-36) to find the electron temperature. Typically, curve fits to the ionization and excitation cross section and reaction rate data shown in Figs. 4-15 and 4-16 are used to evaluate the reaction-rate coefficients in a program that iteratively solves Eq. (4.3-36) for the electron temperature.

The primary electron density in Eq. (4.3-36) can be evaluated from the total primary electron confinement time in the discharge chamber. The emitted current I_e from the hollow cathode is

$$I_e = \frac{n_p \, e \, V}{\tau_t} , \qquad (4.3\text{-}37)$$

where τ_t is the total primary confinement time that addresses all of the primary electron thermalization and loss mechanisms. The ballistic confinement time for direct primary loss to the anode, τ_p, was given in Eq. (4.3-4). It is assumed that the primary electrons have undergone an inelastic collision with the neutral gas and have lost sufficient energy such that they are then rapidly thermalized with the plasma electrons. The mean time for a collision between the primary and a neutral gas atom to occur is given by

$$\tau_c = \frac{1}{n_o \sigma v_p}, \tag{4.3-38}$$

where σ is the total inelastic collision cross section. Using Eq. (4.3-35) for the neutral density, the mean collision time for primary electrons is

$$\tau_c = \frac{v_o e A_g T_a \eta_c \eta_m}{4\ \sigma v_p I_B (1-\eta_{md})} = \frac{v_o A_g T_a \eta_c}{4 \sigma v_p Q_{\text{in}} (1-\eta_{md})}. \tag{4.3-39}$$

Finally, primary electrons can also be thermalized by equilibrating with the plasma electrons. The time for primary electrons to slow into a Maxwellian electron population was derived by Spitzer [32] and is given by

$$\tau_s = \frac{\omega}{2 A_D l_f^2 G(l_f \omega)}, \tag{4.3-40}$$

where $\omega = \sqrt{2V_{pe}/m}$, eV_{pe} is the primary energy, $l_f = \sqrt{m/2kT_e}$ is the inverse mean velocity of the Maxwellian electrons, A_D is a diffusion constant given by

$$A_D = \frac{8\pi e^4 n_e \ln\Lambda}{m^2}, \tag{4.3-41}$$

and $\ln\Lambda$ is the collisionality parameter [33] given in Eq. (3.6-15). The function $G(l_f \omega)$ is defined in Appendix F, and a curve fit to Spitzer's tabulated values (in CGS units) for this function is provided.

The total primary electron confinement time can be found from

$$\frac{1}{\tau_t} = \frac{1}{\tau_p} + \frac{1}{\tau_c} + \frac{1}{\tau_s}. \tag{4.3-42}$$

Some care needs to be used in including the Spitzer slowing time because some ion thruster designs have a very non-monoenergetic primary energy distribution, which is not described well by Eq. (4.3-40).

The current emitted from the hollow cathode is

$$I_e = I_d - I_s - I_k\,, \tag{4.3-43}$$

where I_s is the screen current and I_k is the ion current back to the cathode. Using Eqs. (4.3-4) and (4.3-38) in Eq. (4.3-37), the primary electron density is given by

$$\begin{aligned} n_p &= \frac{I_e\,\tau_t}{eV} = \frac{I_e}{eV}\left[\frac{1}{\tau_p}+\frac{1}{\tau_c}+\frac{1}{\tau_s}\right]^{-1} \\ &= \frac{I_e}{eV}\left[\frac{v_p A_p}{V}+\frac{4\sigma v_p Q_{\text{in}}(1-\eta_{md})}{v_o A_s T_a \eta_c}+\frac{1}{\tau_s}\right]^{-1}. \end{aligned} \tag{4.3-44}$$

Assuming that the primary electron loss directly to the anode is negligible, the electron equilibration time is long, and the ion current flowing back to the cathode is small, then Eq. (4.3-44) can be written as

$$n_p = \frac{I_e v_o A_s T_a \eta_c}{4V\sigma v_p I_b}\frac{\eta_{md}}{(1-\eta_{md})} = \frac{(I_d - I_s) v_o A_s T_a \eta_c}{4V\sigma v_p I_b}\frac{\eta_{md}}{(1-\eta_{md})}. \tag{4.3-45}$$

This equation demonstrates the characteristic behavior of the primary electron density being proportional to the mass utilization efficiency divided by one minus the mass utilization efficiency originally described by Brophy [18,19]. This dependence is valid unless there are paths for the primary electrons to be lost other than just collisionally with the neutral gas, such as ballistically to the anode or by thermalization with the plasma electrons. The behavior of the primary electron density with changes in the mass utilization efficiency is shown in Fig. 4-17, where the primary electron density is normalized to the value at $\eta_{md} = 0$. As the neutral density decreases in the discharge chamber at higher mass utilization efficiencies, the primary electron density increases rapidly. At 90% mass utilization efficiency, the primary electron density in the discharge chamber is nine times higher than at 50% mass utilization efficiency. This strongly affects the ionization rate and the discharge loss behavior with neutral gas pressure, which will be shown later.

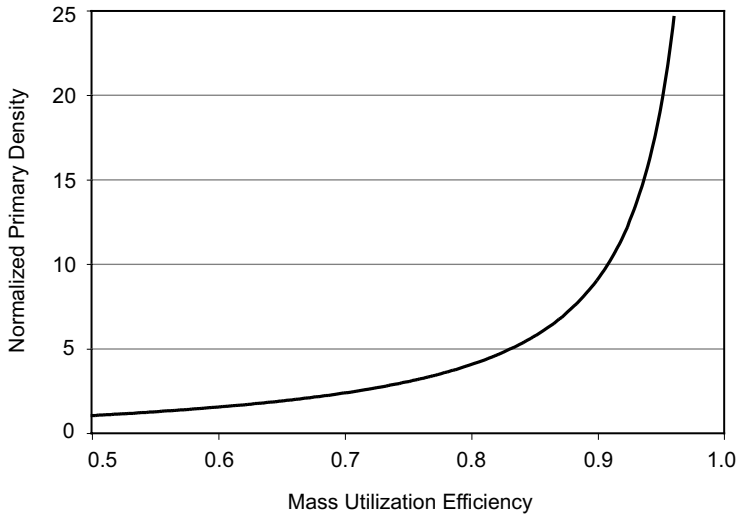

Fig. 4-17. Normalized primary electron density as a function of mass utilization efficiency.

4.3.7 Power and Energy Balance in the Discharge Chamber

The currents and potential distributions in the ring-cusp thruster discharge were shown in Fig. 4-9. The power into the discharge chamber is the emitted current from the hollow cathode multiplied by the voltage the electrons gain in the discharge chamber (V_k in Fig. 4-9):

$$P_{\text{in}} = I_e V_k = I_e \left(V_d - V_c + V_p + \phi \right), \tag{4.3-46}$$

where V_d is the discharge voltage, V_c is the cathode voltage drop, V_p is the potential drop in the plasma, and ϕ is the sheath potential relative to the anode wall. This power into the discharge is transferred from the primary electrons from the cathode into producing ions, excited neutrals, and Maxwellian electrons. The power leaving the discharge to the electrodes is from ions flowing to the anode, cathode, and screen plane, and from primary and plasma electrons flowing to the anode. The power out of the discharge is then the sum of these terms, given by:

$$\begin{aligned} P_{\text{out}} = {} & I_p U^+ + I^* U^* + \left(I_s + I_k \right)\left(V_d + V_p + \phi \right) \\ & + \left(I_b + I_{ia} \right)\left(V_p + \phi \right) + I_a \varepsilon_e + I_L \left(V_d - V_c + V_p + \phi \right), \end{aligned} \tag{4.3-47}$$

where I_p is the total number of ions produced in the discharge, U^+ is the ionization potential of the propellant gas, I^* is the number of excited ions produced in the discharge chamber, U^* is the excitation energy, I_s is the number of ions to the screen plane, I_k is the number of ions flowing back to the cathode, I_B is the beam current, I_a is the plasma electron current to the anode, T_e is the electron temperature, I_{ia} is the ion current to the anode, and I_L is the primary electron fraction lost to the anode. The plasma electron energy lost to the anode wall, ε_e, is $2kT_e/e+\phi$, which is derived in Appendix C. The ions fall through the pre-sheath potential from the center of the plasma to the sheath edge, such that V_p can be approximated as $kT_e/2e$. The ion energy to the anode, ε_i, is then $kT_e/2e+\phi$, which was given in Eq. (4.2-10).

With the screen grid connected to the cathode potential, the current emitted from the hollow cathode was given in Eq. (4.3-43) in terms of the other currents in the circuit. Likewise, conservation of particles flowing to the anode gives

$$I_a = I_d + I_{ia} - I_L, \tag{4.3-48}$$

where I_d is the discharge current measured in the discharge power supply. Equating the power into the discharge to the power out, using the particle balance equations in Eqs. (4.3-43) and (4.3-48), and solving for the beam current from the thruster gives:

$$\begin{aligned} I_b = & \frac{I_d\left(V_d - V_c + V_p - 2T_{eV}\right) - I_p U^+ - I^* U^*}{V_p + \phi} \\ & - \frac{\left(I_s + I_k\right)\left(2V_d - V_c + 2V_p + 2\phi\right)}{V_p + \phi} \\ & - \frac{I_{ia}\left(V_p + 2T_{eV} + 2\phi\right) + I_L\left(V_d - V_c + V_p - 2T_{eV}\right)}{V_p + \phi}, \end{aligned} \tag{4.3-49}$$

where T_{eV} is in electron volts.

The issue in evaluating Eq. (4.3-49) for the beam current produced by a given thruster design is that several of the current terms in the numerator contain the plasma density, which is not known. In addition, the beam current I_B is given

by the Bohm current averaged over the screen-grid plane times the effective transparency T_s of the screen grid:

$$I_b = \frac{1}{2} n_i e v_a A_s T_s \approx \frac{1}{2} n_e e \sqrt{\frac{kT_e}{M}} A_s T_s , \tag{4.3-50}$$

where n_i is the peak ion density at the screen grid, v_a is the ion acoustic velocity, A_s is the screen grid area, and T_s is the effective screen transparency with high voltage applied to the accelerator grids. In this equation, quasi-neutrality ($n_i \approx n_e$) is assumed. Equation (4.3-50) can be solved for the plasma density using Eq. (4.3-49) for the beam current, Eq. (4.3-2) for the primary electron loss current, and Eq. (4.3-17) for the ion loss to the anode wall:

$$n_e = \frac{\left(I_d - I_L\right)\left(V_d - V_c + V_p - 2T_{eV}\right)}{\frac{I_p}{n_e} U^+ + \frac{I^*}{n_e} U^* + \frac{(1-T_s) v_a A_s}{2} V' + \frac{v_a A_{as} f_c}{2}\left(V_p + 2T_{eV} + 2\phi\right)} , \tag{4.3-51}$$

where $V' = 2V_d - V_c + 2V_p + 2\phi$ and the screen grid current, I_s, is given by

$$I_s = \frac{(1-T_s)}{2} n_i e v_a A_s . \tag{4.3-52}$$

The plasma density is proportional to the discharge current decreased by the amount of direct primary loss to the anode ($I_d - I_L$), as expected. This relationship shows why implementing sufficient cusp magnetic field strength is critically important to the thruster performance.

Unfortunately, the ionization and excitation terms still contain n_p / n_e, so Eq. (4.3-52) must be solved iteratively for the plasma density. Once the plasma density is known, the beam current can be calculated from Eq. (4.3-50). If the flatness parameter, which is defined as the average current density divided by the peak, is known, then the peak plasma density and peak beam current density can be obtained. The flatness parameter is found by experimental measurements of the plasma and beam profiles, or by two-dimensional (2-D) models of the discharge that are discussed in Section 4.7.

4.3.8 Discharge Loss

The discharge loss in an ion thruster is defined as the power into the thruster divided by the beam current. This parameter then describes the power required to produce the beam current, which is a good figure of merit for the discharge

chamber performance. In DC-discharge thrusters, the discharge loss for the plasma generator is given by

$$\eta_d = \frac{I_d V_d + I_{ck} V_{ck}}{I_b} \approx \frac{I_d V_d}{I_b}, \tag{4.3-53}$$

where I_B is the beam current, I_{ck} is the current to the cathode keeper electrode (if any), and V_{ck} is the keeper bias voltage. The keeper power is typically negligible in these thrusters, but it is a simple matter to include this small correction. Combining Eqs. (4.3-53) and (4.3-49), the discharge loss is

$$\begin{aligned}\eta_d = & \frac{V_d\left[\frac{I_p}{I_b}U^+ + \frac{I^*}{I_b}U^* + \frac{\left(I_s + I_k\right)}{I_B}\left(2V_d - V_c + 2V_p + 2\phi\right)\right]}{V_d - V_c + V_p - 2T_{eV}} \\ & + \frac{V_d\left[\left(V_p + \phi\right) + \frac{I_{ia}}{I_b}\left(V_p + 2T_{eV} + 2\phi\right)\right]}{V_d - V_c + V_p - 2T_{eV}} \\ & + \frac{V_d\left[\frac{I_L}{I_b}\left(V_d - V_c + V_p - 2T_{eV}\right)\right]}{V_d - V_c + V_p - 2T_{eV}}.\end{aligned} \tag{4.3-54}$$

To evaluate the first current fraction in this equation, the ions are produced by both primary electrons and the energetic tail of the Maxwellian distribution of the plasma electrons. The total number of ions produced in the discharge, I_p, is given in Eq. (4.3-25), and the total number of excited neutrals produced in the discharge, I^*, is given in Eq. (4.3-26).

Using Eqs. (4.3-25) and (4.3-26) for the particle production and excitation, Eq. (4.3-50) for the beam current, and assuming $n_i \approx n_e$, the first current fraction in Eq. (4.3-54) is

$$\frac{I_p}{I_b} = \frac{2n_o n_e e\langle\sigma_i v_e\rangle V}{n_i e\sqrt{\frac{kT_e}{M}}A_s T_s} + \frac{2n_o n_p e\langle\sigma_i v_p\rangle V}{n_i e\sqrt{\frac{kT_e}{M}}A_s T_s}$$
$$= \frac{2n_o V}{\sqrt{\frac{kT_e}{M}}A_s T_s}\left(\langle\sigma_i v_e\rangle + \frac{n_p}{n_e}\langle\sigma_i v_p\rangle\right). \quad (4.3\text{-}55)$$

The second current fraction is likewise:

$$\frac{I^*}{I_b} = \frac{2n_o V}{\sqrt{\frac{kT_e}{M}}A_s T_s}\left(\langle\sigma_* v_e\rangle + \frac{n_p}{n_e}\langle\sigma_* v_p\rangle\right). \quad (4.3\text{-}56)$$

Neglecting the small amount of ion current backflowing to the hollow cathode, the third current fraction is

$$\frac{I_s}{I_b} = \frac{1-T_s}{T_s}. \quad (4.3\text{-}57)$$

The ion current that goes to the anode wall is, again, the Bohm current reduced by the confinement factor f_c, given in Eq. (4.3-17). In this model, the value of the confinement factor must be evaluated for the particular ion thruster discharge chamber being analyzed. However, for most ion thruster designs, if the 50 gauss contour is closed, it is possible to assume to first order that $f_c \approx 0.1$ and the ion loss to the anode surface area is essentially one-tenth of the local Bohm current. For a given confinement factor f_c, the fourth current fraction in Eq. (4.3-54) is

$$\frac{I_{ia}}{I_b} = \frac{\frac{1}{2}n_i e\sqrt{\frac{kT_e}{M}}A_{as} f_c}{\frac{1}{2}n_i e\sqrt{\frac{kT_e}{M}}A_s T_s} = \frac{A_{as} f_c}{A_s T_s}, \quad (4.3\text{-}58)$$

where A_{as} is the surface area of the anode facing the plasma in the discharge chamber.

The primary electron current lost to the anode, I_L, is given by Eq. (4.3-2). The last current fraction in Eq. (4.3-54) is then

$$\frac{I_L}{I_b} = \frac{n_p e v_p A_p}{\frac{1}{2} n_i e v_a A_s T_s} = \frac{2 n_p v_p A_p}{n_e v_a A_s T_s}. \tag{4.3-59}$$

The discharge loss can then be written

$$\begin{aligned} \eta_d = & \frac{V_d \left[\frac{I_p}{I_b} U^+ + \frac{I^*}{I_b} U^* + \frac{1 - T_s}{T_s} \left(2V_d - V_c + 2V_p + 2\phi \right) \right]}{V_d - V_c - 2T_{eV}} \\ & + \frac{V_d \left[\left(V_p + \phi \right) + \frac{A_{as} f_c}{A_s T_s} \left(V_p + 2T_{eV} + 2\phi \right) \right]}{V_d - V_c - 2T_{eV}} \\ & + \frac{V_d \left[\frac{2 n_p v_p A_p}{n_e v_a A_s T_s} \left(V_d - V_c + V_p - 2T_{eV} \right) \right]}{V_d - V_c + V_p - 2T_{eV}}. \end{aligned} \tag{4.3-60}$$

Equation (4.3-60) illuminates some of the design features that improve the discharge efficiency. Since the discharge voltage V_d appears in both the numerator and denominator of Eq. (4.3-60), there is no strong dependence of the discharge loss on voltage shown in this equation. However, increases in the discharge voltage raise the primary energy strongly, which increases the ionization rate and beam current. Therefore, higher discharge voltages always result in lower discharge losses. Higher screen grid transparency T_s, smaller ion confinement factor f_c (better ion confinement), smaller primary loss area A_p, and smaller wall surface area A_{as} all reduce the discharge loss. Lowering the plasma potential also reduces the discharge loss by reducing the energy lost to the anode by the plasma electrons, which is accomplished by reducing the anode loss area at the cusps.

The input data required to solve Eq. (4.3-60) are:

- Discharge voltage
- Discharge chamber surface area and volume
- Magnetic field design (magnetic field at the cusp and the closed contour field between the cusps)
- Grid area
- Grid transparency
- Gas temperature
- Cathode voltage drop

It is necessary to specify either the discharge current or the beam current in order to calculate the plasma density in the discharge chamber. The grid transparency is obtained from the grid codes (called “optics codes”). Several of these codes, such as the Jet Propulsion Laboratory (JPL) CEX ion optics codes [34,35] that we use, are described in Chapter 5. The cathode voltage drop is either measured inside the hollow cathode [36] or calculated using a separate 2-D hollow cathode plasma model [37] that will be described in Chapter 6.

Discharge chamber behavior is characterized by “performance curves,” which were described in Chapter 2 and are graphs of discharge loss versus mass utilization efficiency. These curves plot the electrical cost of producing beam ions as a function of the propellant utilization efficiency, and they give useful information on how well the plasma generator works. Performance curves are normally taken at constant beam current and discharge voltage so that the efficiency of producing and delivering ions to the beam is not masked by changes in the discharge voltage or average plasma density at the grids.

Calculating performance curves using Eq. (4.3-60) requires iteration of the solutions for the electron temperature, discharge current, and/or beam current in the above equations. To measure the discharge loss versus mass utilization in thrusters, the discharge current, total gas flow, and gas flow split between the cathode and main discharge chamber are normally varied to produce a constant beam current and discharge voltage as the mass utilization efficiency changes. This means that a beam current and mass utilization operating point can be specified, which determines the neutral gas density in the discharge chamber from Eq. (4.3-35) and the average plasma density in the discharge chamber from the Bohm current in Eq. (4.3-9). If an initial discharge current is then specified, the primary electron density can be calculated from Eq. (4.3-45) and the electron temperature obtained by finding a solution to Eq. (4.3-36). These parameters are used to solve for the discharge loss, which is evaluated from the given beam current, discharge voltage, and discharge loss. A program is iterated until a discharge current is found that produces the correct discharge loss at the specified beam current.

An example of performance curves calculated using this model and compared to measured curves for the NEXIS ion thruster [38] are shown in Fig. 4-18. The discharge loss was measured for three different discharge voltages during operation at 4 A of beam current. The 180-eV/ion discharge loss at the 26.5-V discharge voltage required that the cathode produce a discharge current of 27.8 A to generate the 4 A of ion beam current.

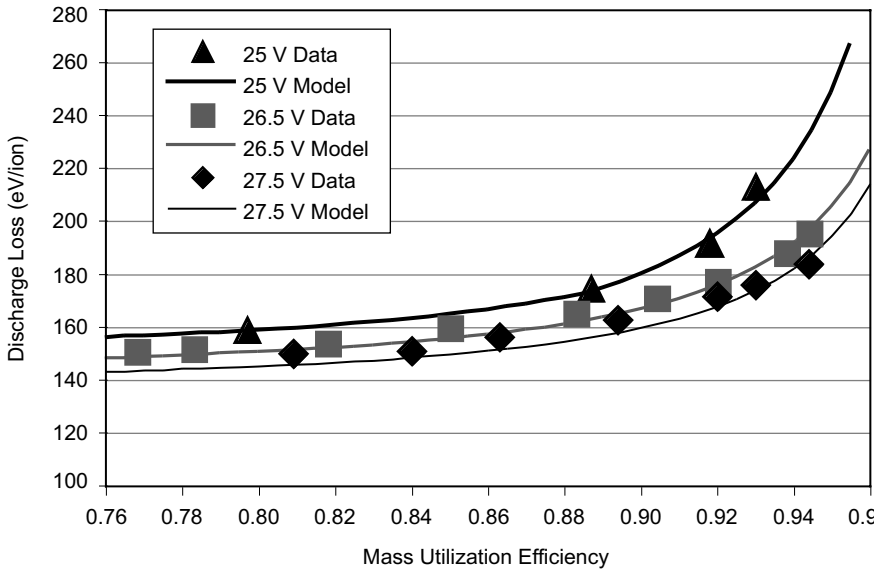

Fig. 4-18. Example of the discharge loss versus mass utilization efficiency for three discharge voltages in the NEXIS thruster [38].

The discharge model also matches the discharge loss data obtained from other thrusters. Figure 4-19 shows the discharge loss measured at JPL in a laboratory copy of the NSTAR thruster [39] operating at the full power (2.3 kW) TH15 throttle level. The model predictions agree with the thruster data if the measured 6.5-V cathode voltage drop in the NSTAR hollow cathode [40] is used for V_c. The ability of a 0-D model to match the NSTAR data is significant only in that the NSTAR plasma is not very uniform (flatness parameter ≈ 0.5) and contains over 20% double ions peaked on the axis. The 0-D model likely works in this case because the ionization is still dominated by the average volume effects, and the losses are still determined by the magnetic field structure at the wall, which 0-D models can capture sufficiently to give reasonably accurate results.

The shape of the performance curves is also important. As the mass utilization is increased, the neutral density in the discharge chamber decreases [see Eq. (4.3-35)] and more of the primary energy goes into heating the plasma electrons and energy loss directly to the anode, as was illustrated by the simplified model for the idealized thruster case in Section 4.2. Optimal thruster designs have flatter discharge performance curves that exhibit lower discharge losses as the mass utilization efficiency is increased. The model suggests that this is generally achieved in thrusters by designing for good primary and

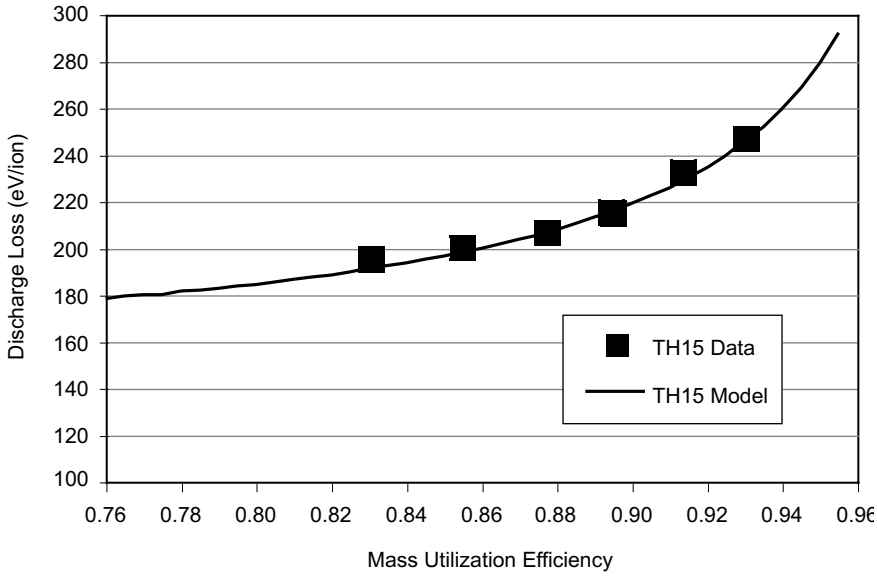

Fig. 4-19. Discharge loss versus mass utilization efficiency for the NSTAR thruster at the high power TH15 throttle point.

plasma electron confinement such that the convective losses are minimized at low neutral density and higher electron temperatures.

A significant challenge for most discharge models is handling the primary electrons correctly. For the case of monoenergetic primaries assumed in this model, the primary density is determined by collisional and ballistic (direct-to-anode) losses that change as a function of the neutral pressure, which is inversely proportional to the mass utilization efficiency. The primary electron density then varies strongly as the mass utilization efficiency is changed. However, if primary electrons are neglected altogether (i.e., assumed thermalized immediately in the cathode plume) so that the plasma in the discharge chamber is produced only by ionization by the high-energy tail of the Maxwellian electron population, the discharge loss is extremely high. This is shown in Fig. 4-20, where the discharge loss in the NEXIS thruster increases to over 240 eV/ion if the primary electron ionization effects are neglected. Likewise, if the primary electron density is independent of the neutral pressure, then the discharge loss curve in Fig. 4-20 has a steep slope resulting from an excessive number of primary electrons at low mass utilization (high pressure), which produces more ionization than actually occurs. Clearly, including the presence of primary electrons in the analysis is required for the model results to agree with the data, which, in turn, suggests that primary or energetic electrons and non-Maxwellian electron populations must exist in this type of thruster.

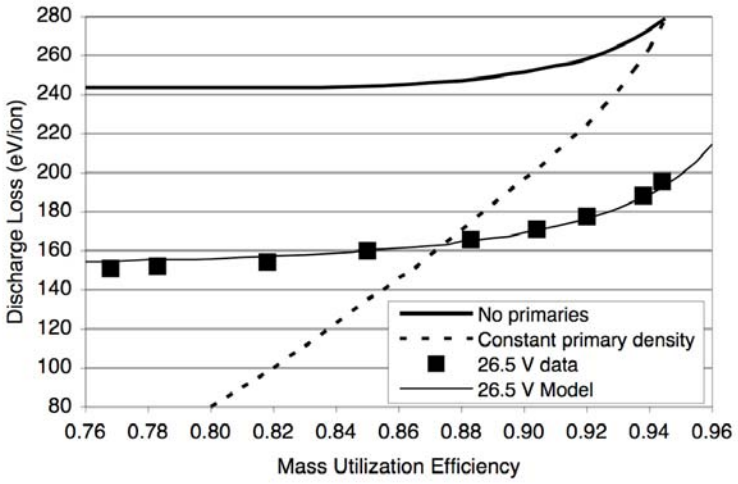

Fig. 4-20. Discharge loss predictions for the cases of no primary electron density and a constant primary electron density showing the poor agreement with the measurements.

Having a representative model of the discharge permits environmental changes to the thruster to also be understood. For example, the neutral gas temperature depends on the operating time of the thruster until equilibrium is reached, which can take hours in some cases, during which the discharge loss will vary [41]. The 0-D model predictions are shown in Fig. 4-21 for three different neutral gas temperatures. The discharge loss data points shown were measured for the NEXIS thruster operating at 26.5 V and 92% mass utilization efficiency at first turn on, after 1 hour, and after 10 hours. In this case, the thruster starts at essentially room temperature, and the model predicts that the discharge heats the thruster and neutral gas to about 470 K after about 10 hours of operation. While thruster thermal time constants are usually on the order of 1 hour, this long heating time was found to be related to the facility thermal time constant. This behavior of the discharge loss with time and temperature illustrates how characterization of the thruster must always be measured in thermal equilibrium, because the performance of the discharge chamber is strongly affected by the neutral gas density, which changes with the thruster temperature for a constant input flow rate.

4.3.9 Discharge Stability

There is a strong relationship between the discharge loss and the stability of the discharge. By inspection of Eq. (4.3-60), it is clear that the efficiency increases (discharge loss decreases) if the anode area for primary electrons A_p is minimized. While it is logical to assume that this is also true if the anode area

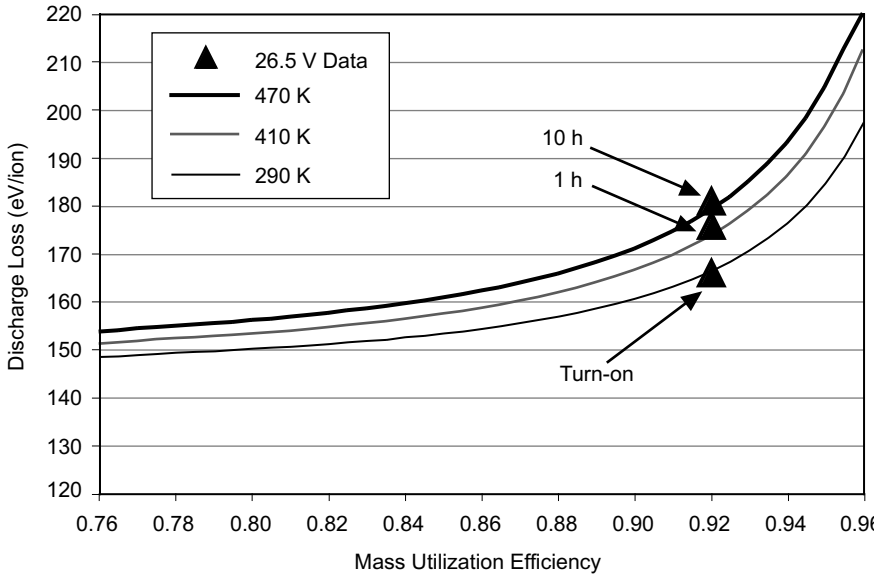

Fig. 4-21. Discharge loss versus mass utilization efficiency from the model for the NEXIS thruster [20] for three neutral gas temperatures,

for plasma electrons is minimized to reduce the energy loss from the Maxwellian-electron population, a dependence on A_a does not appear in Eq. (4.3-60). However, since the discharge current is carried to the anode primarily by the plasma electrons, the sheath potential at the anode wall in Eq. (4.3-7) is found to decrease as the anode area decreases for a given plasma electron current to the anode. A dependence on the sheath potential is seen in the discharge loss equation, which suggests that minimizing the sheath potential maximizes the efficiency. However, the anode area for plasma electrons cannot go to zero because the discharge current could not be collected by the anode, and the discharge would either interrupt or become unstable [22]. So there is some minimum anode area and plasma potential that can be tolerated for discharge stability.

The value of the plasma potential relative to the anode (the anode sheath voltage drop) can be calculated using the expression for the random electron flux to the anode given in Eq. (4.3-7). From current conservation in the discharge, an expression for the discharge current can also be found from the current to the anode [Eq. (4.3-48)]:

$$I_d = I_a + I_L - I_{ia}\,. \tag{4.3-61}$$

Using Eqs. (4.3-7), (4.3-2), and (4.3-17) for each of the three currents, and dividing by the beam current in Eq. (4.3-50), Eq. (4.3-61) becomes

$$\frac{I_d}{I_b} = \frac{\frac{1}{4}\left(\frac{8kT_e}{\pi\, m}\right)^{1/2} n_e A_a}{\frac{1}{2} n_e v_a A_s T_s} \exp^{-e\phi/kT_e} + \frac{n_p v_p A_p}{\frac{1}{2} n_e v_a A_s T_s} - \frac{\frac{1}{2} n_e v_a A_{as} f_c}{\frac{1}{2} n_e v_a A_s T_s}. \quad (4.3\text{-}62)$$

Solving for the plasma potential gives

$$\phi = \frac{kT_e}{e} \ln\left[\frac{\left(\frac{2M}{\pi m}\right)^{1/2} \frac{A_a}{A_s T_s}}{\frac{I_d}{I_b} + \frac{A_{as} f_c}{A_s T_s} - \frac{2 n_p v_p A_p}{n_e v_a A_s T_s}}\right]. \quad (4.3\text{-}63)$$

By inspection of Eq. (4.3-63), it is clear that as the anode area A_a decreases, the plasma potential also decreases. If the anode area is made too small, then the plasma potential will go negative relative to the anode potential. This is called a positive-going (or "electron accelerating") anode sheath, and is illustrated in Fig. 4-22. In this case, the anode area at the cusps is insufficient to collect the total discharge current by collection of the entire incident random electron flux over the cusp area. The plasma then biases itself to pull in electrons in the Maxwellian distribution that are not initially headed toward the anode, which delivers more current to satisfy the discharge current and charge balance requirements. The plasma electron current collected by the anode then becomes

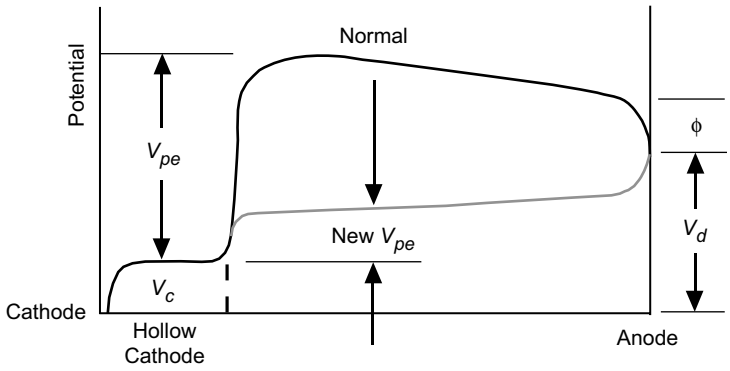

Fig. 4-22. Transition of the plasma potential to negative relative to the anode due to an anode area decrease, which results in a lower primary electron energy.

$$I_a = \frac{1}{4}\left(\frac{8kT_e}{\pi m}\right)^{1/2} en_e A_a \; e^{e\phi/kT_e}\left[1 - erf\left(\frac{-e\phi}{kT_e}\right)^{1/2}\right]^{-1}, \qquad (4.3\text{-}64)$$

where the potential ϕ is now a negative number. If the potential goes sufficiently negative relative to the anode, the current density can reach a factor of two higher than the one-sided random electron flux normally collected in order to satisfy the discharge current requirement.

However, once the potential goes sufficiently negative relative to the anode to repel the ions (about T_i), then the anode area for the plasma electron is not the hybrid area, but is just twice the plasma electron Larmor radius times the cusp length, similar to Eq. (4.3-3) for the primary loss area. This results in a significant decrease in the cusp anode area A_a in Eq. (4.3-63) for negative plasma potentials, which further lowers the plasma potential relative to the anode. Examining the potential distribution in the plasma in Fig. 4-22, the transition from the normal negative-going sheath to a negative plasma potential (positive-going anode sheath) will subtract from the primary electron energy V_{pe} at a given discharge voltage. The ionization rate then decreases, and the discharge collapses into a high impedance mode or oscillates between this mode and a positive potential typically on power supply time constants as the supply tries to reestablish the discharge by increasing the anode voltage.

The stability of the plasma discharge at a given operating point (discharge current, beam current, neutral density in the discharge chamber, etc.) is therefore determined by the magnetic field design. For example, in Fig. 4-23, plasma potential is plotted as a function of the strength of the cusp magnetic field for an arbitrary thruster design with two different numbers of ring cusps. The cusp field strength enters into the anode area A_a in Eq. (4.3-6), into the primary electron loss area A_p in Eq. (4.3-3), and into the plasma potential in Eq. (4.3-63). The model predicts that a four-ring design would be unstable (when the potential goes negative relative to the anode) for cusp magnetic fields greater than 2000 G. Since strong magnetic fields are desirable from a primary electron and ion confinement point of view, additional rings are required to maintain a positive plasma potential. A six-ring design increased the anode area sufficiently to raise the plasma potential at the 2000-G magnet design point. An analysis of the discharge loss from Eq. (4.3-60) indicates that the improved stability associated with the larger anode area of the six-ring design comes with a loss in efficiency. The trade-off between efficiency and stability is an important aspect of ion thruster design.

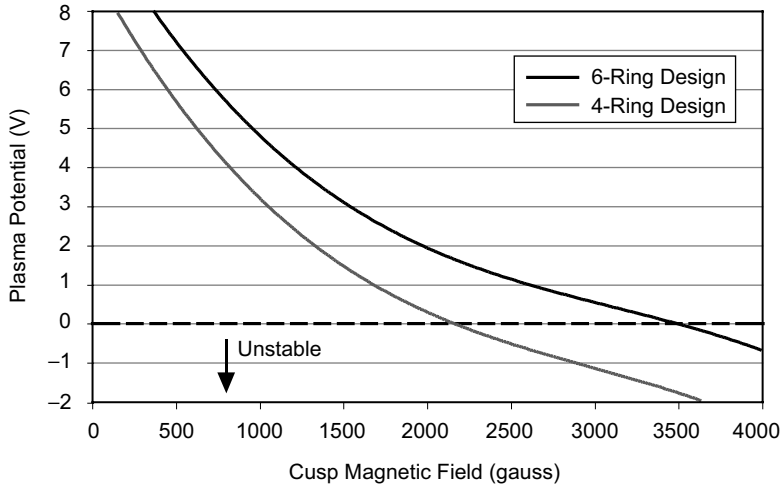

Fig. 4-23. Plasma potential versus cusp magnetic field strength for a thruster design with 4 and 6 rings.

4.3.10 Recycling Behavior

Ion thrusters clear momentary faults or breakdowns in the high voltage accelerator grids by momentarily turning off the high voltage, an event called recycling. In order to restart the thruster, the accelerator grid ("accel grid") voltage must be turned back on to avoid electron backstreaming into the thruster as the screen voltage is reapplied. If the plasma discharge is left on during this sequence, the negatively biased accel grid collects nearly the entire ion beam current at the applied accel voltage until the screen voltage is re-established. This can lead to excessive power loading and even erosion of the accel grid if a significant number of recycles are encountered. Therefore, it is standard procedure to also either turn off the discharge during recycling or cut it back to a low level such that the accel grid current surge is acceptably low during reestablishing of the beam voltages. The discharge current is then raised to the desired level with the screen voltage ramp-up.

The main issue with this process is that the thruster discharge often goes into oscillation during the cutback condition or upon restarting in the recycle sequence. When the high voltage is turned off in a recycle, ions that would have left the discharge chamber as beam ions now strike and neutralize on the accel grid, and some fraction flows back into the discharge chamber as neutral gas. This raises the neutral gas pressure in the discharge chamber, which has two effects. First, a higher neutral pressure collisionally thermalizes the primary electrons more rapidly, which can lead to a reduction in the plasma potential [22]. Second, lowering the discharge current while raising the neutral pressure

leads to a lower impedance discharge and a lower discharge voltage. These two effects will be shown next to cause a reduction in the plasma potential, and thrusters designed for low discharge loss with a minimum plasma potential at the nominal operating point can encounter negative plasma potentials and discharge instability during recycling.

The time-dependent behavior of the pressure in the discharge chamber from the high-voltage-off event can be calculated using molecular dynamics, and the subsequent time-dependent plasma potential for stability can be evaluated using the 0-D model. The time-dependent pressure [42] in the thruster is given by

$$V\frac{dP}{dt} = Q_{\text{in}} - C\Delta P\,, \tag{4.3-65}$$

where V is the discharge chamber volume, P is the pressure in the thruster discharge chamber, C is the conductance of the grids, and ΔP is the pressure drop across the grids. The initial pressure just before the start of the recycle, when the thruster is operating normally, is found from Eq. (4.3-35) and the conversion of neutral density to pressure in Eq. (2.7-2):

$$P_o = 4.1\times 10^{-25}\,\frac{T_o Q_{\text{in}}(1-\eta_m)}{v_o e A_g T_a \eta_c}\,. \tag{4.3-66}$$

With the high voltage off, the ions and neutrals flow to the grid region, where a small fraction exits through the accel aperture to escape, and the majority strike the upstream side of the grids or the grid aperture barrel wall and flow back into the thruster. Since the grid conductance is defined as the flow divided by the pressure drop [42], the final pressure after steady state has been achieved is

$$P_f = \left(1-T_a\right)\frac{Q_{\text{in}}}{C}\,, \tag{4.3-67}$$

where C is the conductance of the grids and the downstream pressure from the grids has been neglected as small. The conductance of the grids can be estimated from the molecular conductance of a thin aperture [42] times the Clausing factor for the finite thickness grids. The conductance is then

$$C = 3.64\left(\frac{T}{M_a}\right)^{1/2} T_a A_g \eta_c \text{ [liters/s]}, \tag{4.3-68}$$

where M_a is the ion mass in atomic mass units (AMU), and the effective open area of the grids is the optical transparency of the accel grid, T_a, times the grid

area, A_g. Integrating Eq. (4.3-67) from the initial pressure to the final pressure gives

$$P(t) = P_f - (P_f - P_o)e^{-t/\tau_g}, \tag{4.3-69}$$

where $\tau_g = V/C$ is the gas flow time constant for filling the thruster chamber. To use Eq. (4.3-69) to find the final pressure, the gas flow rate has to be converted from particles per second to torr-l/s by multiplying the neutral gas flow in Eq. (4.3-67) by 2.81×10^{-20}.

Figure 4-24 shows an example of the pressure increase with time calculated in the NEXIS thruster discharge chamber from the start of a recycle. The pressure in the discharge chamber during normal operation is in the mid-10^{-5} torr range due to the large grid area and high mass utilization efficiency. During a recycle, the pressure in the discharge chamber reaches equilibrium in about 60 ms, with the pressure increasing almost an order of magnitude once the high voltage is turned off. This magnitude of pressure increase in the thruster once the high voltage is turned off is consistent with the ≈90% mass utilization efficiency of many thruster designs.

The plasma potential response to pressure changes in the discharge chamber calculated using the 0-D model for two different discharge voltages is shown in Fig. 4-25(a) for a given magnetic field design. During the recycle, the discharge current is reduced (called "cutback"), which reduces the discharge voltage and

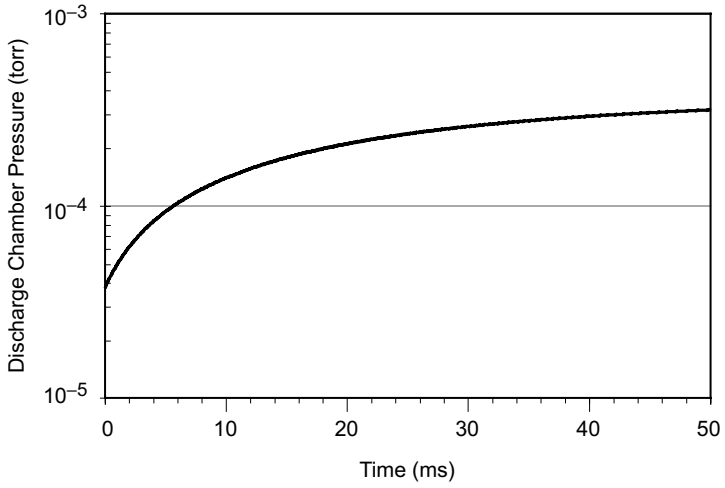

Fig. 4-24. Example of the pressure rise in the NEXIS thruster [20] calculated during a recycle.

thereby the plasma potential. The model indicates that the plasma potential reduction and subsequent unstable operation is the result of the lower discharge voltage, and does not occur directly due to the discharge current being lower. This analysis shows that a given thruster design that produces a stable discharge under normal conditions can go unstable due to negative plasma potentials as the pressure rises and the discharge voltage decreases.

The plasma potential calculated using Eq. (4.3-63) for two magnet designs is shown in Fig. 4-25(b) for the 23-V NEXIS case, which illustrates the effect of the smaller anode area reducing the plasma potential at a given pressure. In this case, increasing the anode area permitted the discharge current to be cutback

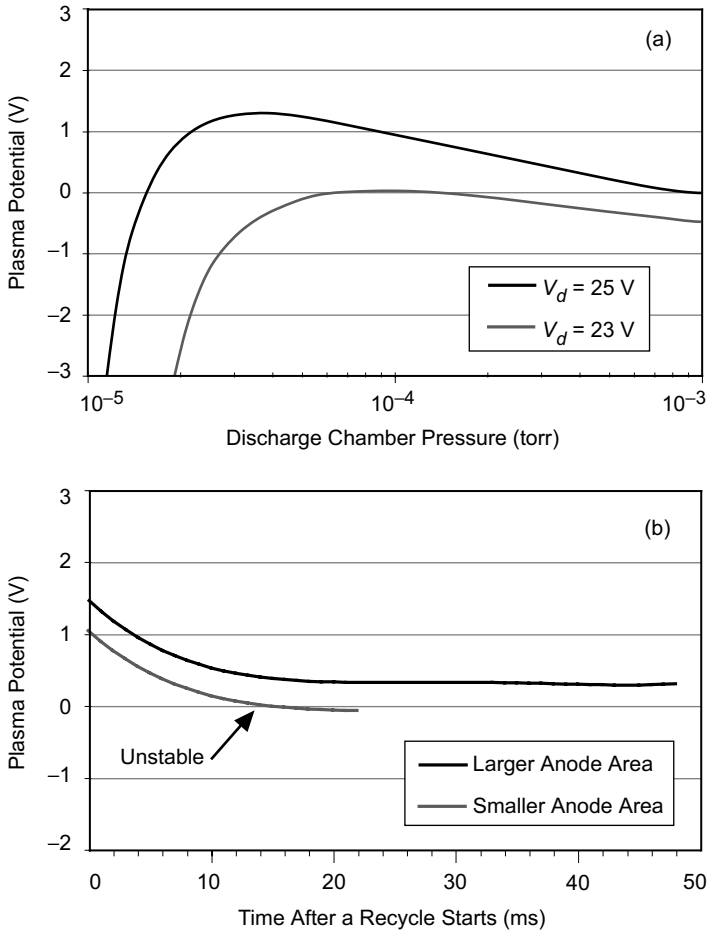

Fig. 4-25. Plasma potential as a function of pressure for two different discharge voltages (a), and plasma potential versus time (b) showing instability of the smaller anode area design at a given pressure.

during the recycle to the desired level without oscillating, which facilitates re-starting the high voltage. Of course, the larger anode area increased the loss in the discharge chamber and raised the discharge loss. This trade-off is often required to provide good performance and stable discharge operation.

4.3.11 Limitations of a 0-D Model

While the 0-D models described in this chapter provide useful information on the design parameters of ion thrusters and give good insight into the plasma production and loss mechanisms, there are several limitations to their use. First, 0-D models assume that the electron and neutral densities are uniform and averages the ion production throughout the volume of the discharge chamber. For ion thrusters with significantly non-uniform plasmas, this leads to inaccuracies in the average plasma density and beam current calculated by the 0-D model that can be handled only by multi-dimensional discharge chamber models. Second, the source of the gas in actual discharge chambers is from the localized hollow cathode aperture and the gas manifold inside the discharge chamber. The neutral density, therefore, is never completely uniform, and variations in the neutral density can affect the transport, diffusion, and ionization rates in the discharge chamber.

Third, ion thrusters with localized electron sources like hollow cathodes have strongly varying primary electron densities within the discharge chamber. As shown earlier, the primary electron density strongly affects the ionization rate, and so localized sources of primaries produce non-uniform plasmas that the 0-D models cannot address. In addition, these models utilize a monoenergetic primary energy. A distribution in the primary electron energy has been measured in some ion thrusters [43,44], which changes the ionization and primary electron thermalization rates compared to the monoenergetic calculations presented here. While primary electron energy distributions can be incorporated in 0-D models, this has not been attempted to date.

Finally, the 0-D model assumed that the monoenergetic primary electrons have an energy of $e(V_d - V_c + \phi)$. For typical discharge voltages of 25 V and cathode voltage drops of 5 to 10 V, this means that potentially none of the primaries has sufficient energy to doubly ionize xenon, which has an ionization potential of 21.2 V. Double ions can then only be produced by the tail of the plasma electron distribution. For electron temperatures of 3 to 5 eV, less than 1% of the electrons have sufficient energy to produce double ions. Since the double-ion content in NSTAR thrusters has been reported to exceed 20%, a monoenergetic primary electron energy results in a model that cannot accurately address double-ion production. While including primary electrons is necessary to obtain agreement between the 0-D models and experimental results, knowledge of the

correct energy distribution and even spatial variation in the primaries is required, and is better handled by 2-D models discussed in Section 4.7.

4.4 Kaufman Ion Thrusters

The formulation of particle and energy balance models just described applies to any ion thruster geometry where the electron loss can be defined by a finite anode electrode area collecting electrons at a fraction of the random electron flux depending on the sheath voltage. One class of thrusters still in use, the Kaufman ion thruster shown schematically in Fig. 4-26, features a strongly diverging axial magnetic field that shields a cylindrical anode electrode located near the wall of the discharge chamber. In this case, electron transport to the anode is determined by cross-field diffusion.

In Section 3.6, the flux of electrons due to cross-field diffusion is given by

$$\Gamma_e = nv_\perp = \mu_\perp n\mathbf{E} - D_\perp \nabla n. \tag{4.4-1}$$

For the case of Kaufman thrusters, the perpendicular diffusion coefficient is likely to be close to the Bohm diffusion coefficient [45]:

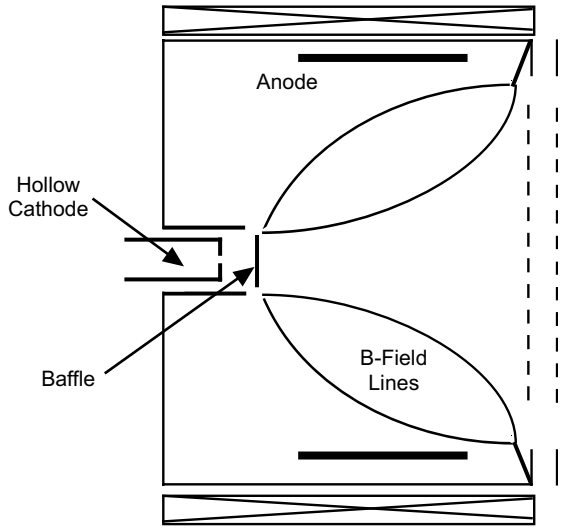

Fig. 4-26. Schematic of a Kaufman ion thruster showing the hollow cathode with a baffle, and the anode protected by magnetic fields produced by an external solenoid coil.

$$D_B = \frac{1}{16}\frac{kT_e}{eB}. \tag{4.4-2}$$

The electron current collected by the anode is the flux that diffuses through the magnetic field times the Boltzman factor at the sheath:

$$I_a = \left(\mu_\perp n\mathbf{E} - D_\perp \nabla n\right) eA_{as} e^{-e\phi/kT_e}, \tag{4.4-3}$$

where A_{as} is again the anode surface area exposed to the plasma discharge. The actual current distributions and potential distribution in a Kaufman thruster are the same as for the DC discharge thruster shown in Fig. 4-9. However, there are several terms that were analyzed for ring-cusp thrusters that can be neglected in Kaufman thrusters.

First, if the axial magnetic field in the discharge chamber is on the order of 100 G, then the Larmor radius for, say, 20-eV primaries is 1.5 mm. Since the magnetic field lines do not intersect the anode and primaries are too energetic to participate in the collective instabilities that drive Bohm diffusion, the primary electrons must make collisions in order to cross the magnetic field to be lost. That means that the fraction of the primary electron current loss directly to the anode in ring-cusp thrusters, I_L, can be neglected, which is an advantageous feature of Kaufman thrusters.

Second, the plasma flow across the magnetic field is still governed by ambipolar effects. As was shown in Section 4.3.4, if the transverse magnetic field strength is in excess of about 50 G in typical ion thruster discharge chambers, then the radial electric field in the plasma (in the magnetic field region) is near zero and the ion loss rate is on the order of one-tenth the Bohm current toward the wall. This means that the ion current to the anode term, I_{ia}, can also be neglected to first order. Since the discharge current collected through the anode leg of the discharge power supply connection was given in Eq. (4.3-61) as the plasma electron current minus the ion current and plus the primary current, the discharge current is now just

$$I_d = I_a = -D_\perp \nabla n\, eA_{as} e^{-e\phi/kT_e}. \tag{4.4-4}$$

Third, the ion current flowing back towards the hollow cathode was neglected in our treatment of ring-cusp thrusters because the hollow cathode exit area in contact with the plasma was so small. In Kaufman thrusters, a baffle is placed on axis in front of the cathode to force the primary electrons off axis to flatten the density profile. Since the magnetic field is strongly divergent, the axial plasma density gradient is significant and the plasma density in contact with the

baffle can be high. For these reasons, the ion current to the cathode, I_k, can no longer be neglected.

The power into the plasma is given by Eq. (4.3-46), and the power out of the discharge is given by

$$P_{\text{out}} = I_p U^+ + I^* U^* + I_s\left(V_d + \varepsilon_i\right) + I_k\left(V_d + \varepsilon_i\right) + I_b\varepsilon_i + I_{ia}\varepsilon_i + I_a\varepsilon_e, \quad (4.4\text{-}5)$$

where ε_i is the ion energy leaving the plasma, which is written here from Eq. (4.3-10) as $T_{eV}/2 + \phi$, and ε_e is the electron energy removed from the plasma, which is written from Eq. (4.3-9) as $2T_{eV} + \phi$. Equating the power in to the power out again and solving for the discharge loss gives

$$\eta_d = \frac{V_d\left[\frac{I_p}{I_b}U^+ + \frac{I^*}{I_b}U^* + \phi + \frac{T_{eV}}{2} + \frac{\left(I_s + I_k\right)}{I_b}\left(2V_d - V_c + 2\phi + \frac{T_{eV}}{2}\right)\right]}{V_d - V_c - 2T_{eV}}. \quad (4.4\text{-}6)$$

The first current ratio, I_p / I_b, is given by Eq. (4.3-55), and the second current ratio, I^* / I_b, is given by Eq. (4.3-56). The current ratio, I_s / I_b, is given by Eq. (4.3-57), and the last current ratio is

$$\frac{I_k}{I_b} = \frac{\frac{1}{2}n_k e\sqrt{\frac{kT_e}{M}}A_k}{\frac{1}{2}n_i e\sqrt{\frac{kT_e}{M}}A_s T_s} = \frac{n_k A_{sa}}{n_e A_s T_s}, \quad (4.4\text{-}7)$$

where n_k is the plasma density at the cathode baffle. The discharge loss for Kaufman thrusters is then

$$\eta_d = \frac{V_d\left[\frac{I_p}{I_b}U^+ + \frac{I^*}{I_b}U^* + \phi + \frac{T_{eV}}{2} + \left(\frac{1 - T_s}{T_s} + \frac{n_k A_{sa}}{n_e A_s T_s}\right)\left(2V_d - V_c + 2\phi + \frac{T_{eV}}{2}\right)\right]}{V_d - V_c - 2T_{eV}}. \quad (4.4\text{-}8)$$

The plasma potential in Eq. (4.4-8) is found from solving Eq. (4.4-4):

$$\phi = \frac{kT_e}{e}\ln\left[\frac{-D_\perp \nabla n\, e A_{as}}{I_d}\right], \quad (4.4\text{-}9)$$

and the electron temperature is found from the solution to ion particle balance in Eq. (4.3-36) in a similar manner as for ring-cusp thrusters. The negative sign in Eq. (4.4-9) appears problematic in the natural log function, but the density gradient ∇n is negative going outward from the plasma. The primary electron density is calculated from Eq. (4.3-45), with the ballistic loss term neglected as described above since primaries are not lost directly to the anode. Finally, the plasma volume term in the ion and excited neutral production rates can be assumed to be the volume of a cone from the baffle to the grids because the plasma is well confined by the strongly diverging magnetic field. Since the 0-D model assumes relatively uniform plasma, estimates for the radial gradient of the plasma density in the magnetic field region near the anode and the additional cathode voltage drop due to the baffle must be made for Eq. (4.4-8) to be accurate.

As an example, take a conceptual Kaufman thruster with a 20-cm-diameter screen grid with 80% transparency and a 25-cm-diameter anode with 25 cm between the grids and the baffle. Assuming that the average magnetic field strength in the thruster is about 50 G, the discharge loss from Eq. (4.4-8) is plotted in Fig. 4-27 for two values of the cathode voltage drop. In this case, the cathode voltage drop is higher than in a ring-cusp thruster because it includes the potential drop in the baffle region. The discharge loss is strongly dependent on this value because it directly affects the primary electron energy. Discharge losses in this range at mass utilization efficiencies of about 90% have been reported in the literature for Kaufman thrusters through the years [46–48],

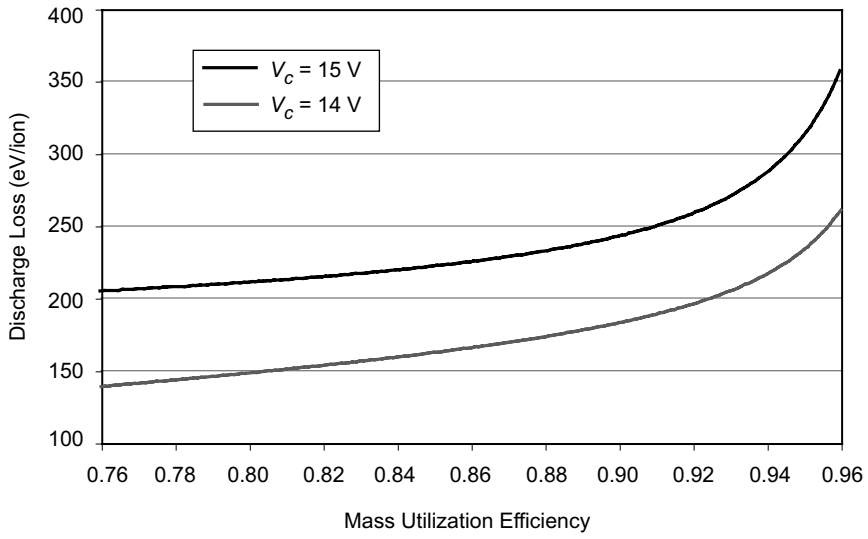

Fig. 4-27. Discharge loss calculated for Kaufman thruster example.

suggesting that the 0-D model can produce reasonable predictions of the discharge loss if the cross-field diffusion is handled properly.

The need for higher discharge voltages in Kaufman thrusters, compared to ring-cusp thrusters, is illustrated in Fig. 4-28, where the discharge loss is plotted for the Kaufman thruster example above with two cases of the discharge voltage at a constant (total) cathode voltage drop of 16 V. Low discharge loss is achieved for the 35-V discharge voltage case, but decreasing the discharge voltage to 30 V causes the discharge loss to increase dramatically. This is because the primary electron energy in the discharge chamber is near the threshold energy for ionization at this discharge voltage, and the discharge efficiency decreases as more ionization is required from the plasma electrons. In addition, the lower discharge voltage causes the plasma potential to go significantly negative relative to the anode potential ($\approx T_e$), which will cause the discharge to become unstable.

While Kaufman-type thrusters are considered to be the first ion thruster to achieve good discharge production performance, they now compete with ring-cusp thrusters for application in modern electric propulsion systems. This is because of several constraints in Kaufman thruster design. First, the strong axial magnetic field restricts electron motion to the anode to cross-field diffusion, which requires either high neutral pressures in the discharge chamber for electron-neutral collisional diffusion and, thereby, low mass utilization efficiency, or relies on collective instabilities to increase the diffusion rate to

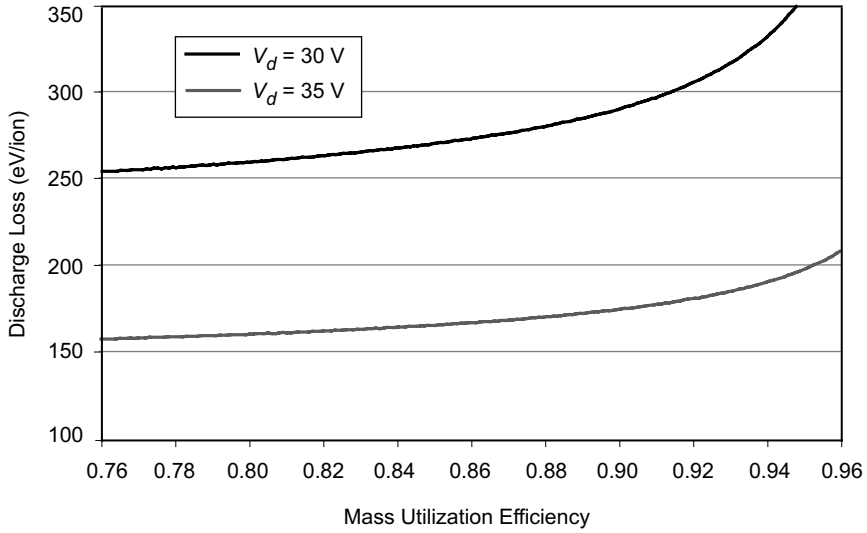

Fig. 4-28. Discharge loss calculated for Kaufman thruster example at two discharge voltages.

obtain sufficient electron loss to support the discharge. The instabilities are usually related to $\mathbf{E} \times \mathbf{B}$ driven instabilities and Bohm diffusion [24], which create significant noise in the discharge that can appear in the beam current. Second, the baffle required to force the primary electrons off axis to produce a more uniform plasma profile is susceptible to ion bombardment sputtering and plasma losses in the dense plasma region near the cathode. This has historically limited the life of these types of thrusters, although alternative materials can mitigate this problem. In addition, the primary electrons are injected purely off axis, which means that the plasma profile, and hence the beam profile, can be hollow or peaked depending on the cross-field diffusion and mobility throughout the discharge chamber.

Finally, the thruster size, shape, and magnetic field strength is limited to regimes where the magnetic field is sufficient to confine ions by electrostatic ambipolar effects to obtain good efficiency, and yet the magnetic field is not so high that the cross-field diffusion cannot provide adequate electron current for the discharge to be stable. If the field is too strong or the anode area in contact with the plasma is too small, the plasma potential goes negative relative to the anode to pull the electrons out of the discharge. Inspection of Fig. 4-22 shows that if the plasma potential is negative relative to the anode, then the primary energy is decreased at a given discharge voltage, which strongly affects the discharge efficiency [22]. Since the discharge voltage cannot be arbitrarily increased due to ion sputtering of the baffle and screen electrodes, in addition to excessive double-ion production, this will significantly reduce the discharge efficiency. In the case of negative plasma potentials, the electron loss to the anode has the form [22]

$$I_a = -D_\perp \nabla n \, e A_{as} e^{e\phi/kT_e} \left[1 - erf\left(\frac{-e\phi}{kT_e} \right)^{1/2} \right]^{-1}, \qquad (4.4\text{-}10)$$

where ϕ is a negative number in this case. The negative plasma potential increases the current to the anode area A_{as} by pulling some of the electrons from the plasma population that were headed away from the anode. While up to a factor of two more electron current theoretically can be drawn compared to the case for the case of positive plasma potentials, in practice drawing even the random electron flux can strongly deplete or perturb the Maxwellian population and affect the plasma discharge. The geometry of Kaufman thrusters for good efficiency is limited to configurations where the plasma potential in the discharge chamber is not allowed to go negative relative to the anode, which constrains the design space for the electrodes and fields.

4.5 rf Ion Thrusters

The ion thrusters described in the previous sections utilize a thermionic hollow cathode and DC discharge power supply to inject hot electrons into the discharge chamber to ionize the propellant gas. To eliminate any potential life or power supply issues with the hollow cathode and DC-electron discharge, an alternative thruster design utilizes electromagnetic fields to heat the plasma electrons that, in turn, ionize the injected gas. One method to achieve this goal is to use an inductive plasma generator, which is normally called a radio-frequency, or rf, ion thruster. In this case, low frequency rf voltage is applied to an antenna structure around or in the plasma, and the rf energy is coupled to the electrons.

The simplest configuration for an rf ion thruster is shown schematically in Fig. 4-29. An rf coil is wrapped around an insulating chamber with a gas feed. The chamber can be cylindrical, hemispherical, or conical in shape and is connected to an ion accelerator structure that is the same as those used for electron-bombardment ion thrusters with either two or three grids. The plasma floats relative to the first grid, and the high voltage is applied between the two grids to accelerate ions that flow through the first grid and form the beam. The rf coil is connected to an rf power supply that provides the power to generate the plasma. There is usually no applied magnetic field in rf ion thrusters, although one can be applied in principle to improve the discharge performance. As in other ion thruster designs, the entire discharge chamber is enclosed in a metallic screen or structure to eliminate electron collection from the space plasma, and a neutralizer cathode is connected to provide net charge neutralization of the beam.

The coil wrapped around the insulating thruster body can be modeled as a solenoid with N turns, and the rf voltage applied to it drives an rf current in the

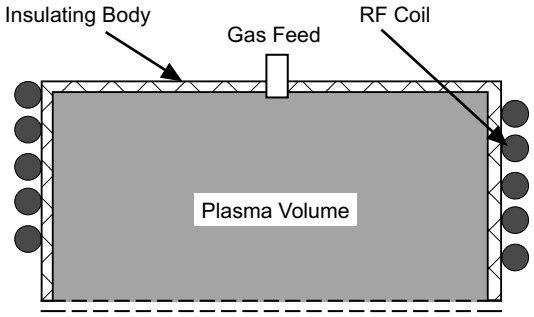

Fig. 4-29. Schematic of an rf ion thruster showing induction coil, insulating body, gas feed and two-grid accelerator structure.

coil. Typical frequencies used in rf ion thrusters are in the range of 1 MHz. At these frequencies, the penetration of the fields from the coil at the boundary is limited by the skin depth in the plasma [24], which is on the order of or slightly less than the radius of most rf ion thrusters at the plasma densities required to produce xenon ion current densities in excess of 1 mA/cm^2. This produces an attenuation of the electric and magnetic fields toward the axis, and the majority of plasma interaction with the fields occurs off axis closer to the boundary.

The axial magnetic field inside the coil induced by the rf current, neglecting end effects, is

$$B_z = \frac{NI}{\mu_o} e^{i\omega t}, \tag{4.5-1}$$

where I is the rf current in the coil, μ_o is the permeability of the vacuum, ω is the cyclic frequency ($2\pi f$) of the rf, and t is the time. From Maxwell's equation, the time-varying magnetic field creates a time-varying electric field:

$$\nabla \times \mathbf{E} = -\frac{\partial \mathbf{B}}{\partial t}. \tag{4.5-2}$$

The induced rf electric field in the rf thruster geometry is then in the azimuthal direction:

$$E_\theta = -\frac{i\omega r}{2} B_{zo} e^{i\omega t}, \tag{4.5-3}$$

where r is the distance from the axis and B_{zo} is the peak axial rf magnetic field from Eq. (4.5-1). A finite electric field is generated spatially off axis inside the thruster.

The induced electric field exists in one direction ($\pm\theta$ direction) for roughly half a period, which for a 1-MHz frequency is 0.5 microseconds. The electrons, however, don't see the oscillating component of the electric field because they transit the interaction region close to the antenna in a time much less than this value. For example, a 5-eV electron will travel a distance of about 1 meter in 1 microsecond, and so can traverse the electric field region many times within a half cycle. Therefore, electrons traversing the induced electric field region "see" a DC electric field and are accelerated. If they make a collision prior to leaving the region, they can then retain some or all of the velocity imparted by the electric field and are heated.

The criteria for the rf plasma generator to provide net heating of the electrons is that a sufficient number of electrons make a collision within the electric field interaction region. If the interaction region is, say, a few centimeters across, the mean free path should be on this order. The probability of an electron making a collision is given by

$$P = 1 - \exp^{-x/\lambda} = 1 - \exp^{-n_o \sigma x}. \tag{4.5-4}$$

Using Eq. (2.7-2) to convert from neutral density to pressure, the minimum pressure at a temperature T in the plasma chamber of an rf thruster for breakdown to occur is

$$P_{\min}[\text{torr}] = \frac{-1.04 \times 10^{-25}\ T}{\sigma\ x} \ln(1 - P). \tag{4.5-5}$$

For example, the minimum pressure for starting the rf-generated plasma is plotted in Fig. 4-30, where room temperature (290 K) xenon gas with a xenon atomic radius of 1.24 Å in a 5-cm-long interaction region is assumed. If 10% of the electrons must make an electron-neutral collision within a 5-cm interaction region to provide sufficient heating for sustaining ionization and breakdown to proceed, then the minimum pressure in the thruster is about 1×10^{-3} torr. Minimum pressures in the range of 10^{-3} to 10^{-2} torr are commonly reported in the literature for rf plasma sources to ignite the plasma. Once the plasma source is ignited, the required electron collisions to provide the heating in the rf

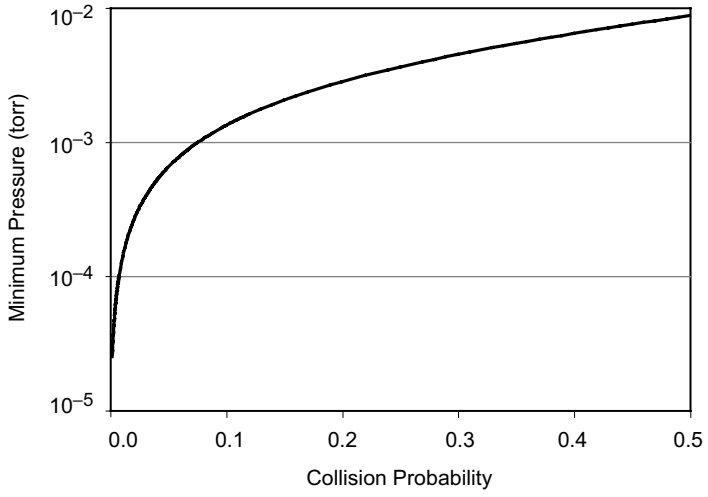

Fig. 4-30. Minimum pressure for starting a xenon rf thruster with a 5-cm interaction zone as a function of the probability of an electron having a collision.

electric fields can be supplemented by coulomb collisions between the plasma electrons, which reduce the operating pressure requirement and permit high mass utilization efficiency to be achieved.

Starting an inductive plasma discharge can also be problematic because initially there are few free electrons present to interact with the rf fields and ionize the fill gas. Prior to the plasma ignition, there is no load on the rf circuit driving the coil and the reactive power stored in the inductive components in the rf matching network grows, which increases the voltage across the coil and induces higher electric fields inside. If the minimum gas pressure is provided, the discharge will ignite when the field is either large enough to excite the few electrons naturally present in the chamber or causes field emission to occur. Another method for ignition is to inject electrons from a spark generator, small cathode, or the neutralizer cathode (with the accel voltage turned off momentarily) into the discharge chamber to provide the seed electrons for interaction with the rf electric fields.

If the antenna in rf thrusters is directly exposed to the plasma, ions in the discharge can be accelerated by the rf voltage on the surfaces and sputter-erode the antenna. This can ultimately limit the life of rf thrusters. This problem is minimized by either encasing the antenna in an insulator [49] or by making the thruster body an insulating material and mounting the antenna exterior to the plasma volume [50]. In this case, the rf voltage across the coil is shielded from the plasma, and the ions are not accelerated to high energy before striking the insulator. Mounting rf antennas outside insulating-material walls such as quartz or alumina is common practice in inductive plasma generators used in the semiconductor processing industry. An example of this arrangement applied to a radio-frequency ion thruster (RIT)-XT thruster [50] is shown in Fig. 4-31. In this case, the body of the thruster is constructed of a conical (or hemispherical) alumina insulator, and a high-conductivity-material (typically copper) antenna is coiled around the insulator. As long as the alumina body is not significantly coated by conductive layers and remains an insulator, the rf fields will couple through the wall and generate plasma.

This type of ion thruster is readily analyzed by particle and energy balance models because they do not have localized electron sources (hollow cathodes); the rf fields simply heat the Maxwellian electron distribution that provides the ionization, and the plasma in the discharge chamber is very uniform. In the energy balance equation, it is assumed that the power absorbed by the plasma is simply given by P_{abs}. Ions generated in the plasma volume drift to the interior surfaces in the thruster, and only electrons in the tail of the Maxwellian distribution have sufficient energy to overcome the potential difference

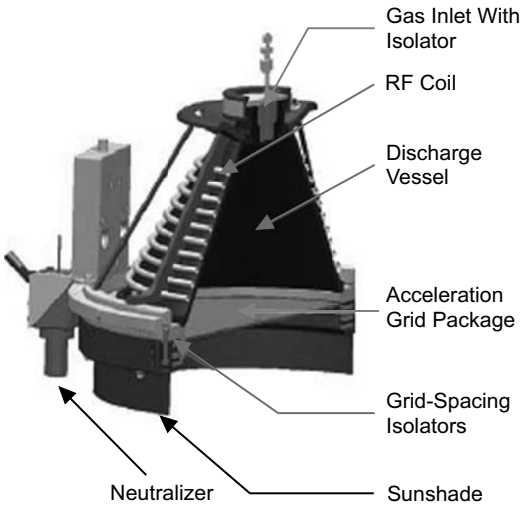

Fig. 4-31. rf ion thruster design showing the alumina body, exterior rf coil, accelerator grid assembly and neutralizer cathode. The antenna system is enclosed in a metal "plasma shield" to eliminate electron collection from the space plasma (from [50]).

between the plasma and the wall. The power out of the plasma equals the power absorbed, which is given by

$$P_{\text{abs}} = I_p U^+ + I^* U^* + \left(I_s + I_w + I_b\right)\left(\frac{T_{eV}}{2} + \phi\right) + I_a\left(2T_{eV} + \phi\right), \qquad (4.5\text{-}6)$$

where the electron and ion energy loss terms are shown explicitly. Equating the input power to the output power, the discharge loss is then

$$\begin{aligned}\eta_d &= \frac{P_{\text{abs}}}{I_b} \\ &= \frac{I_p}{I_b}U^+ + \frac{I^*}{I_b}U^* + \left(\frac{I_s}{I_b} + \frac{I_w}{I_b} + 1\right)\left(\frac{T_{eV}}{2} + \phi\right) + \frac{I_a}{I_b}\left(2T_{eV} + \phi\right).\end{aligned} \qquad (4.5\text{-}7)$$

The ionization and excitation is now only due to the plasma electrons, so the first current fraction in Eq. (4.5-7), using Eq. (4.3-50) and assuming quasi-neutrality ($n_i \approx n_e$), is

$$\frac{I_p}{I_b} = \frac{2n_o\langle\sigma_i v_e\rangle V}{\sqrt{\frac{kT_e}{M}}A_s T_s}, \qquad (4.5\text{-}8)$$

and the second current fraction is likewise:

$$\frac{I^*}{I_b} = \frac{2n_o \left\langle \sigma_* v_e \right\rangle V}{\sqrt{\frac{kT_e}{M}} A_s T_s}. \tag{4.5-9}$$

The screen current-to-beam current ratio is given in Eq. (4.3-57) as $(1-T_s)/T_s$.

The ion current that goes to the wall is the Bohm current to the wall area A_w reduced by radial confinement provided by any applied or induced magnetic fields. The fourth current ratio is then

$$\frac{I_w}{I_b} = \frac{\frac{1}{2} n_i v_a A_w f_c}{\frac{1}{2} n_i v_a A_s T_s} = \frac{A_w f_c}{A_s T_s}, \tag{4.5-10}$$

where f_c is again a confinement factor for the reduction in the Bohm velocity due to ambipolar effects in the ion and electron flows to the wall. Since there are no applied DC potentials in the discharge chamber and all the walls float, the electron current out is the same as the ion current out:

$$I_a = I_s + I_w + I_b. \tag{4.5-11}$$

Plasma potential in the expression for the discharge loss [Eq. (4.5-7)] can be evaluated by equating the total ion and electron currents exiting the plasma:

$$\frac{n_i}{2}\sqrt{\frac{kT_e}{M}}(A_w f_c + A_s) = \frac{n_e}{4}\sqrt{\frac{8kT_e}{\pi\, m}}\left[A_w + (1-T_s)A_s\right]\exp^{-e\phi/kT_e}. \tag{4.5-12}$$

Solving for the plasma potential gives

$$\phi = \frac{kT_e}{e}\ln\left[\frac{A_w + (1-T_s)A_s}{A_w f_c + A_s}\sqrt{\frac{2M}{\pi\, m}}\right]. \tag{4.5-13}$$

If the wall area is large compared to the screen area, or the grid transparency is small compared to 1, this turns into the normal equation for floating potential:

$$\phi = \frac{kT_e}{e}\ln\left[\sqrt{\frac{2M}{\pi\, m}}\right], \tag{4.5-14}$$

which for xenon is $5.97 * T_e$.

Using Eqs. (4.5-8) through (4.5-11), the discharge loss for rf ion thrusters can then be written

$$\eta_d = \frac{2n_o \langle \sigma_i v_e \rangle V}{\sqrt{\frac{kT_e}{M}} A_s T_s} \left(U^+ + U^* \frac{\langle \sigma_* v_e \rangle}{\langle \sigma_i v_e \rangle} \right) + \left[\frac{1 - T_s}{T_s} + \frac{A_w f_c}{A_s T_s} + 1 \right] \left(2.5 T_{eV} + 2\phi \right), \tag{4.5-15}$$

where the plasma potential ϕ is given by Eq. (4.5-13) in eV.

The electron temperature is found, again, by equating the ion production and loss terms

$$n_o n_e e \langle \sigma_i v_e \rangle V = \frac{1}{2} n_i e \sqrt{\frac{kT_e}{M}} \left(A_w f_c + A_s \right). \tag{4.5-16}$$

The electron temperature is then found from the solution to

$$\frac{\sqrt{\frac{kT_e}{M}}}{\langle \sigma_i v_e \rangle} = \frac{2n_o V}{A_w f_c + A_s}. \tag{4.5-17}$$

As an example, assume that the rf ion thruster has a 20-cm grid diameter, an 18-cm-deep conical ceramic discharge chamber, a grid transparency of 80%, and that it produces 2 A of beam current in xenon. Figure 4-32 shows the calculated discharge loss as a function of the mass utilization efficiency from Eq. (4.5-15), assuming no applied or induced magnetic fields and, therefore, no plasma confinement. A discharge loss of about 450 eV/ion is predicted at 90% mass utilization efficiency. This is a very high discharge loss, and it can be seen in Fig. 4-32 that the majority of the energy loss is carried out by the ions and electrons flowing to the floating-potential walls. This is because the Maxwellian electron temperature required to produce the ions that flow to the entire interior surface area of the discharge chamber at 90% mass utilization efficiency [from the solution of Eq. (4.5-17)] is 5 eV, and the plasma potential to achieve net ambipolar flow is, therefore, nearly 30 V. The high sheath potential required to self-confine the electrons for particle balance and the large

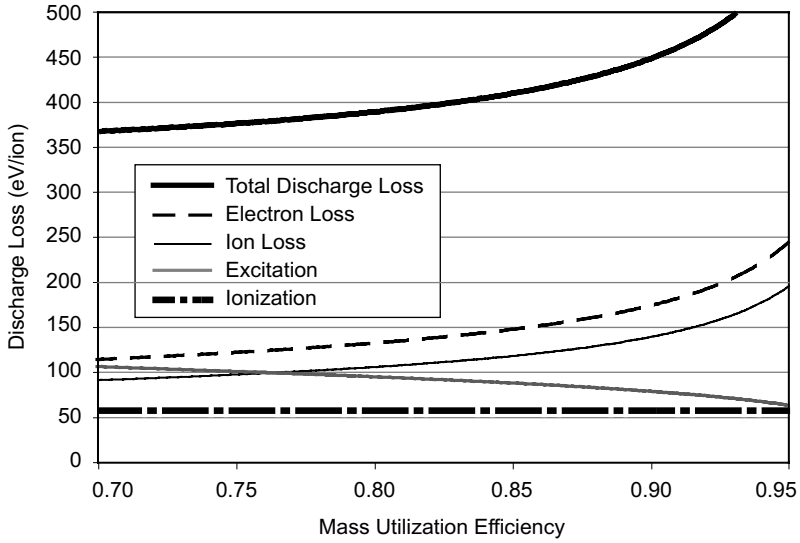

Fig. 4-32. Discharge loss calculated for the example rf ion thruster and the contribution from the four energy loss mechanisms.

plasma loss area ($A_w + A_s$) carry significant energy to the discharge chamber wall, causing a relatively high discharge loss.

The discharge loss performance of rf ion thrusters typically reported in the literature [50] is much lower than that found in our example. This is because even though these thrusters do not usually have an applied DC magnetic field, the rf coil forms a solenoid around the dielectric discharge chamber and the rf current flowing in the antenna coil induces an alternating current (AC) magnetic field in the interior of the discharge chamber with a frequency at the rf oscillator frequency. In most typical rf thrusters, this frequency is on the order of 1 MHz. The ion acoustic speed $\sqrt{kT_e/M}$ at $T_e = 5$ eV is 1.9 km/s, and so in a 1-μs cycle, the ions can only move less than 2 mm, which implies that the ions can be considered stationary on the magnetic-field cycle time. The electrons are certainly not stationary in the period, but the ion space charge will hold the electrons in place during a cycle. Therefore, the AC magnetic field from the rf coil can provide some confinement for the plasma [51] and reduce the flux to the discharge chamber walls. The magnetic field induced by the rf coil depends on the coil size and amount of power. For example, assume that the coil occupies 1 turn per centimeter (100 turns/m), and the coil impedance is 50 ohms. For an input power of 500 W, this would result in 10 A of rf current flowing in the coil. For simplicity, assume the rf coil forms a solenoid and the magnetic field inside a solenoid (neglecting end effects) is

$$B[\text{gauss}] = 10^4 \mu_o \, N \, I, \qquad (4.5\text{-}18)$$

where μ_0 is the permeability of free space, equal to $4\pi \times 10^{-7}$ henries/m; N is the number of turns per meter; and I is the coil current in amperes. For this rf thruster example, a magnetic field of 12.6 G is produced. While this sounds like a low field, it is an axial field induced in the majority of the interior of the thruster depending on the plasma skin depth, which is large in these low density plasmas.

The reduction in the ion velocity flowing radially to the wall for the situation of a transverse magnetic field and ambipolar flows was analyzed in Section 4.3.5. Figure 4-33 shows the reduction in the radial Bohm current (f_c) from evaluating Eq. (4.3-15) for the condition when the diffusion length is now essentially the thruster radius. Fields on the order of 10 G throughout the thruster volume can reduce the ion and electron loss to the discharge chamber wall by over a factor of two. While the rf magnetic field strength decreases with radius due to the finite length of the antenna coil (solenoid end effects), the field strength near the axis is still sufficient to reduce the ion loss rate [51].

The discharge loss calculated by the 0-D model for our 20-cm rf thruster example is shown in Fig. 4-34 as a function of rf magnetic field induced in the plasma. The discharge loss is reduced from the case of no magnetic confinement ($B = 0$) of 450 eV/ion at 90% mass utilization to a value of

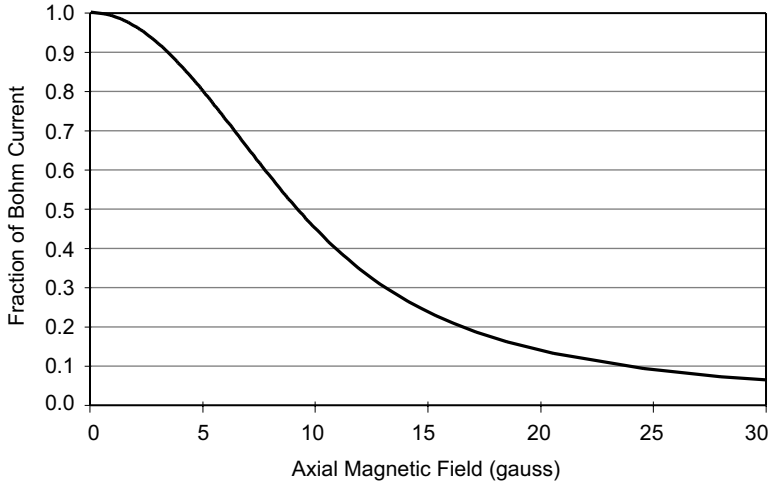

Fig. 4-33. Ion confinement factor (the fraction of the Bohm current to the wall) as a function of the induced magnetic field in the discharge chamber volume.

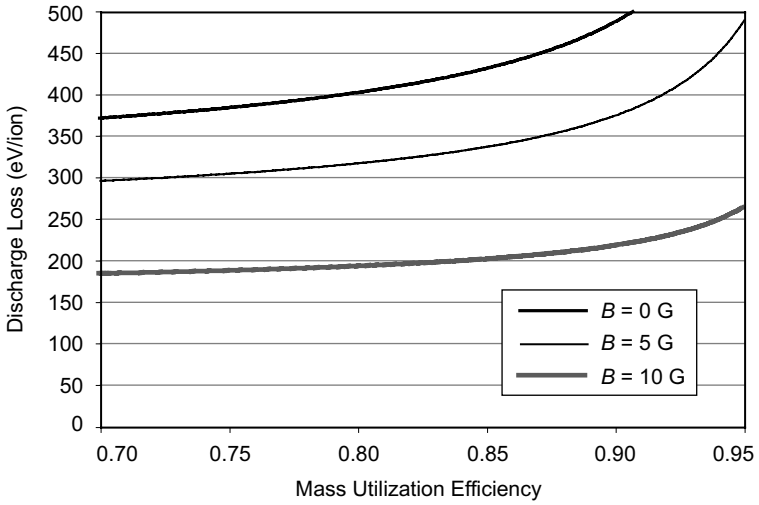

Fig. 4-34. rf ion thruster discharge loss versus mass utilization efficiency for three values of the induced magnetic field in the discharge chamber.

230 eV/ion if 10 G is induced in the chamber. This is a significant reduction in the calculated loss and is the key to rf ion thruster discharge performance.

To produce the 2-A beam in our 20-cm thruster example at 230 eV/ion, a total input power to the antenna of 460 W is required to be absorbed by the plasma. Since the rf power supplies are typically 90% efficient in this frequency range, the input power to the thruster PPU would be about 511 W. This predicted performance is in good agreement with the data about this size of rf thruster found in the literature [50], suggesting that a 0-D particle and energy balance model can provide reasonably accurate performance predictions.

One advantage of rf ion thrusters is that they have only Maxwellian electrons and ambipolar ion and electron loss rates, which simplifies the discharge loss expressions and makes it easy to analyze the few geometric parameters to optimize the discharge loss. An example of the process is as follows: First, specifying the required beam current and current density determines the grid diameter in any ion thruster. Ion optics codes then determine the grid transparency. Once the grid design is set, a Monte-Carlo gas code is used to evaluate the Clausing factor introduced in Eq. (4.3-33). Assuming a conical or cylindrical discharge chamber shape of a given length immediately specifies the loss areas and plasma volume. Then, specifying the mass utilization efficiency gives the neutral density, and the electron temperature can be found from Eq. (4.5-17) with an initial confinement factor assumption. These values are the input parameters to the discharge loss given by Eq. (4.5-15), which provides the

required input rf power to the antenna assuming that the antenna efficiency and coupling (reflected power) are known. The approximate induced AC magnetic field can then be calculated from Eq. (4.5-18) and the ion confinement factor f_c, found as in Section 4.3.4. A simple iteration then gives the final discharge loss and rf power.

It should be noted that as the discharge chamber length decreases, the antenna axial extent also decreases, which reduces the electric field interaction region and decreases the AC axial magnetic field strength due to end effects in the solenoid coil. The ability to breakdown the neutral gas initially and then couple the rf energy to the electrons efficiently may be compromised as the length decreases, which would also affect the discharge loss scaling.

A disadvantage of rf ion thrusters is that the antenna must be insulated from the plasma, and the insulator is then subject to ion bombardment and material deposition. Dielectric discharge chambers are susceptible to mechanical problems in fabrication, environmental testing and launch, and life issues from coating of the insulator surface with conducting layers. The structural issue has been addressed on some flight units by the use of a ceramic discharge chamber with an exterior mounted antenna structure to provide the rigidity required for launch survival. While the discharge loss in rf ion thrusters is typically higher than that found for well-designed electron-bombardment ion thrusters such that the total efficiency is lower, the simplified design of rf thrusters makes it easier to analyze them and predict the performance than most other ion thruster configurations. The rf thruster design concept eliminates any potential discharge cathode life issues and utilizes fewer power supplies to operate the discharge. These factors make rf ion thrusters very competitive for future spaceflight applications.

4.6 Microwave Ion Thrusters

An alternative to producing the plasma in the thruster with electron discharges or rf induction heating of the electron population is to generate the plasma using electromagnetic fields at microwave frequencies. This eliminates life issues associated with the discharge hollow cathode, and the lack of applied DC voltages in the discharge chamber can potentially reduce the sputter erosion of electrodes exposed to the plasma as compared with that of DC electron discharges. However, electromagnetic waves can propagate and be absorbed in plasmas only under certain conditions. For example, if the microwave frequency is too high or the plasma density too low, the microwave radiation is reflected completely from the plasma. If the conditions are such that the microwaves do propagate in the plasma, the microwave energy is coupled to the plasma by resonant heating of the electrons in a magnetic field in the

presence of collisions. The required magnetic field to achieve this resonance is significant, and the pressure required to achieve sufficient collisions to start the discharge can be relatively high. These effects impact the plasma generator design and performance.

The propagation of microwaves in a plasma can be understood by examining the dispersion relationship. The behavior of microwaves in the thruster plasma is described by Maxwell's Equations:

$$\nabla \times \mathbf{E} = -\frac{\partial \mathbf{B}}{\partial t} \tag{4.6-1}$$

$$\nabla \times \mathbf{B} = \mu_o \left(\mathbf{J} + \varepsilon_o \frac{\partial \mathbf{E}}{\partial t} \right). \tag{4.6-2}$$

The electromagnetic behavior is analyzed by linearizing these two equations using

$$\mathbf{E} = \mathbf{E}_0 + \mathbf{E}_1 \tag{4.6-3}$$

$$\mathbf{B} = \mathbf{B}_0 + \mathbf{B}_1 \tag{4.6-4}$$

$$\mathbf{J} = \mathbf{j}_0 + \mathbf{j}_1 , \tag{4.6-5}$$

where $\mathbf{E}_0$, $\mathbf{B}_0$, and $\mathbf{j}_0$ are the equilibrium values of the electric and magnetic fields and currents, and $\mathbf{E}_1$, $\mathbf{B}_1$ and $\mathbf{j}_1$ are the perturbed values in the electromagnetic fields and current. Linearizing Eqs. (4.6-1) and (4.6.2), and realizing that the equilibrium values have no curl or time dependence and that $\varepsilon_o \mu_o = 1/c^2$ in a vacuum, gives

$$\nabla \times \mathbf{E}_1 = -\frac{\partial \mathbf{B}_1}{\partial t} \tag{4.6-6}$$

$$c^2 \nabla \times \mathbf{B}_1 = \frac{\mathbf{j}_1}{\varepsilon_o} + \frac{\partial \mathbf{E}_1}{\partial t} . \tag{4.6-7}$$

Taking the curl of Eq. (4.6-6) gives

$$\nabla \times \nabla \times \mathbf{E}_1 = \nabla \left(\nabla \cdot \mathbf{E}_1 \right) - \nabla^2 \mathbf{E}_1 = -\nabla \times \frac{\partial \mathbf{B}_1}{\partial t} , \tag{4.6-8}$$

and the time derivative of Eq. (4.6-7) gives

$$c^2 \nabla \times \frac{\partial \mathbf{B}_1}{\partial t} = \frac{1}{\varepsilon_o} \frac{\partial \mathbf{j}_1}{\partial t} + \frac{\partial^2 \mathbf{E}_1}{\partial t^2}. \tag{4.6-9}$$

Combining Eq. (4.6-9) with Eq. (4.6-8) results in

$$\nabla\left(\nabla \cdot \mathbf{E}_1\right) - \nabla^2 \mathbf{E}_1 = -\frac{1}{\varepsilon_o c^2} \frac{\partial \mathbf{j}_1}{\partial t} - \frac{1}{c^2} \frac{\partial^2 \mathbf{E}_1}{\partial t^2}. \tag{4.6-10}$$

Assuming that the microwaves are plane waves that vary as

$$\mathbf{E} = E\ e^{i(kx - \omega t)} \tag{4.6-11}$$

$$\mathbf{j} = j\ e^{i(kx - \omega t)}, \tag{4.6-12}$$

where $k = 2\pi / \lambda$ and ω is the cyclic frequency $2\pi f$, then Eq. (4.6-10) becomes

$$-k\left(k \cdot \mathbf{E}_1\right) + k^2 \mathbf{E}_1 = \frac{i\omega}{\varepsilon_o c^2} \mathbf{j}_1 + \frac{\omega^2}{c^2} \mathbf{E}_1. \tag{4.6-13}$$

The electromagnetic waves are transverse waves, so $k \cdot \mathbf{E}_1 = 0$ and Eq. (4.6-13) becomes

$$\left(\omega^2 - c^2 k^2\right) \mathbf{E}_1 = \frac{-i\omega}{\varepsilon_o} \mathbf{j}_1. \tag{4.6-14}$$

Since these waves are in the microwave frequency range, the ions are too massive to move on these fast time scales and the perturbed current $\mathbf{j}_1$ can come only from electron motion. The perturbed electron current density in a plasma is

$$\mathbf{j}_1 = -n_e e \mathbf{v}_{e1}, \tag{4.6-15}$$

where n_e is the plasma density and $\mathbf{v}_{e1}$ is the perturbed electron velocity. If the applied magnetic field is zero or the perturbed electric field is parallel to the applied magnetic field (so called "O-waves"), the equation of motion for the perturbed electron motion is

$$m \frac{\partial \mathbf{v}_{e1}}{\partial t} = -e \mathbf{E}_1. \tag{4.6-16}$$

Solving for the perturbed electron velocity, assuming plane waves, and inserting this into Eq. (4.6-15), the perturbed current is

$$\mathbf{j}_1 = -n_e e \frac{\varepsilon_o \mathbf{E}_1}{i\omega m} . \tag{4.6-17}$$

Inserting Eq. (4.6-17) into Eq. (4.6-14) and solving for the frequency gives the dispersion relation for electromagnetic waves in a plasma:

$$\omega^2 = \frac{n_e e^2}{\varepsilon_o m} + c^2 k^2 = \omega_p^2 + c^2 k^2 , \tag{4.6-18}$$

where the definition of the electron plasma frequency $\omega_p^2 = n_e e^2 / \varepsilon_o m$ has been used.

This expression can be solved for the wavelength of the microwaves in the plasma

$$\lambda = \frac{2\pi c}{\sqrt{\omega_p^2 - \omega^2}} = \frac{c}{\sqrt{f_p^2 - f^2}} , \tag{4.6-19}$$

where f_p is the real plasma frequency and f is the microwave frequency. If the microwave frequency exceeds the plasma electron frequency, the wavelength becomes infinitely long and the wave becomes evanescent (it will not propagate into the plasma) and is reflected. This condition, called cutoff, determines the maximum plasma density into which a microwave source can inject power to produce the plasma. Table 4-1 shows the cutoff frequency for a range of plasma densities and the ion current density from a xenon plasma at an electron temperature of 3 eV. As an example, if the ion thruster design requires an ion

Table 4-1. Cutoff frequencies for several plasma densities, and the corresponding ion current density from a xenon plasma at T_e = 3 eV.

Plasma Density (cm^{-3})	Cutoff Frequency (GHz)	J (mA/cm^2)
10^9	0.285	0.0118
10^{10}	0.900	0.118
10^{11}	2.846	1.184
10^{12}	9.000	11.84
10^{13}	28.460	118.4

current density to the grids of, say, 1.2 mA/cm^2, then a frequency in excess of 2.85 GHz must be used to produce the plasma or else some or all of the microwave power will be reflected.

The microwave energy is coupled to the plasma by electron cyclotron resonance heating, where the microwave frequency corresponds to the cyclic frequency of the electrons in a magnetic field. The resonant frequency is the electron cyclotron frequency, which was derived in Chapter 3:

$$\omega_c = \frac{|q|B}{m}. \tag{4.6-20}$$

The cyclic cyclotron frequency is easily calculated using a convenient formula of $\omega_c = 2.8$ GHz/kG. In the plasma, the actual microwave frequency is $f_c = eB/2\pi m$, which is given in Table 4-2 for several magnetic field values. If it is assumed that the microwave energy is deposited into the volume of a plasma immersed in the magnet field, the maximum plasma density (and corresponding ion current density to the grids) to avoid cutoff is shown for each of the magnetic field values. To produce current densities in excess of 1 mA/cm^2 of xenon to the accelerator grids from a 3-eV electron temperature plasma requires magnetic fields in excess of 1000 gauss, and values closer to 2000 G are required to avoid cutoff for slightly higher ion current densities to the grids. This is a significant magnetic field to produce in the discharge chamber volume.

The use of microwave radiation enables direct heating of the plasma electrons, but for the wave to add energy to the electrons, collisions must occur.

Table 4-2. Electron cyclotron frequencies for several magnetic field levels, the corresponding maximum plasma density before cutoff, and the maximum ion current density to the grids from a 3 eV electron temperature xenon plasma.

Magnetic Field (G)	Cyclotron Frequency f_c (GHz)	Maximum Plasma Density (cm^{-3})	Maximum Ion Current Density (mA/cm^2)
100	0.28	9.68×10^8	0.012
500	1.40	2.42×10^{10}	0.286
1000	2.80	9.68×10^{10}	1.146
2000	5.60	3.87×10^{11}	4.58
3000	8.40	8.71×10^{11}	10.31
4000	11.20	1.55×10^{12}	18.34

Otherwise, the energy received by an electron during acceleration on each half-cycle of its cyclotron motion is taken back by deceleration of the electron in the field on the next half-cycle. Therefore, there is a minimum pressure at which sufficient collisions occur to ignite the plasma and sustain the discharge. The probability of a collision occurring is

$$P = \left[1 - \exp^{-n_o \sigma\, x}\right] = \left[1 - \exp^{\left(-x/\lambda_{en}\right)}\right], \tag{4.6-21}$$

where x is the path length of the electron in the neutral gas with a density of n_o, and λ_{en} is the electron-neutral collision mean-free-path. An electron entering the interaction region gyrates around the magnetic field lines due to its perpendicular velocity and travels along the magnetic field line due to its parallel velocity.

While the electron cyclotron heating tends to spin-up the electron motion around the field lines, collisions tend to scatter the motion along the direction of the field lines and thermalize the electrons into a Maxwellian distribution, sometimes with a high-energy bump or tail driven by the resonance. The collisionality requirements to achieve heating can be found from examining the path length of an electron at a temperature T_e spiraling along a field line. The distance that the electron travels when gyrating around the field lines is given by the Larmor radius, which was derived in Chapter 3:

$$r_L = \frac{v_\perp}{\omega_c} = \frac{m v_\perp}{|q|\, B} = \frac{1}{B}\sqrt{\frac{2 m v_\perp}{e}}. \tag{4.6-22}$$

The time for an electron to leave the microwave interaction region of length L is

$$t = \frac{L}{v_{||}}, \tag{4.6-23}$$

where $v_{||}$ is the parallel electron velocity along the field line. The number N of gyrations that an electron makes in the interaction region is the microwave frequency f multiplied by the time in the resonant region. The path length of the perpendicular gyration of the electron is then

$$L_g = 2\pi\, r_L N = 2\pi\, r_L\, f \frac{L}{v_{||}}. \tag{4.6-24}$$

The total path length of the helical motion of the electron is

$$L_T = \sqrt{L_g^2 + L^2} = \sqrt{\left(\frac{2\pi\, r_L\, f L}{v_{\|}}\right)^2 + L^2}\ . \qquad (4.6\text{-}25)$$

Using this value for the path length x of the electron in Eq. (4.6-21) gives the probability of a collision with the neutral gas. Figure 4-35 shows this probability calculated for xenon gas at room temperature for electrons with a temperature of 2 eV in two different interaction lengths. To achieve the order of 10% of the electrons colliding with neutral gas atoms in a 5- to 10-cm-long resonance region requires an internal pressure of at least 10^{-3} torr. In reality the electrons must make multiple collisions within the interaction region because the energy gain in a single gyration is small. However, this pressure is similar to that found for rf thrusters to achieve sufficient collisions to start or sustain a discharge, for essentially the same reasons. Again, once the plasma is started, coulomb collisions will aid in transferring the electron motion in the microwave fields into heating, which reduces the pressure required to operate the plasma generator and permits higher mass utilization efficiencies to be achieved.

As was shown in Tables 4-1 and 4-2, a high magnetic field (>1 kG) and a high microwave frequency (>2.8 GHz) are required to produce sufficient plasma density to deliver reasonable current densities (>1mA/cm^2 in xenon) to the grids in microwave thrusters. Due to the difficulty in producing these high magnetic fields throughout the discharge chamber volume, the resonance region is often localized to a small zone inside the thruster volume, and the plasma is allowed

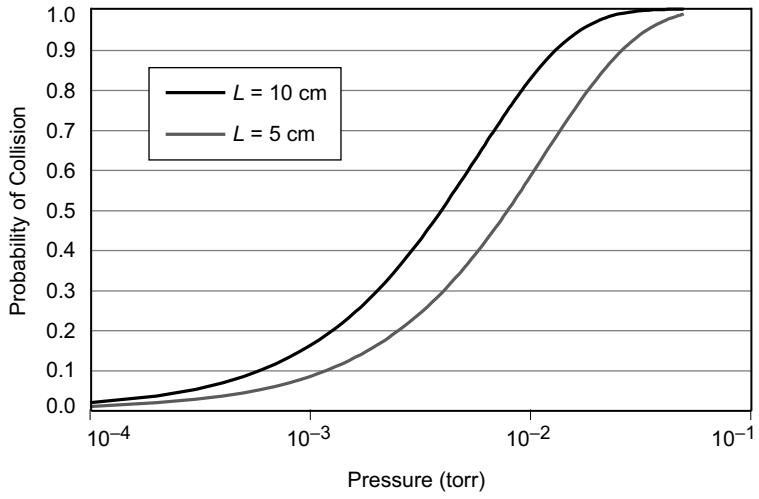

Fig. 4-35. Probability of an electron-neutral collision before leaving the resonance zone length indicated as a function of neutral pressure for 2-eV electrons.

to expand to the grids along divergent magnetic field lines. Figure 4-36 shows an ECR plasma source where a stronger magnetic field region resonant with 2.4-GHz radiation (produced by commercial magnetron microwave sources) is restricted to the rear of the discharge chamber. Of course, expanding the plasma from the resonance region to the grids decreases the plasma density and current density, so even higher magnetic fields and frequencies than just mentioned are normally required in the interaction region to produce over $1\ \mathrm{mA/cm^2}$ to the grids.

The microwave radiation in this ECR plasma source is coupled into the rear of the discharge chamber through a waveguide window, and a quartz liner is used in the resonant region to ensure that the hot electrons are not lost directly to the metal walls of the chamber. The magnetic field in this geometry is produced by electromagnets, with a strong divergence in the field to spread the plasma over the grid region at the exit of the discharge chamber. This is a common geometry for industrial ion sources and plasma sources used in plasma processing, and the performance of the plasma generator is well known.

The performance of this style of microwave ion thruster can be examined with a 0-D model. Assume that the magnetic field is sufficiently strong that radial losses can be neglected. This assumption implies that the plasma is frozen on the field lines such that the density decreases linearly with the area increase as the field expands. This simplifies the model to the case of a straight cylindrical source with no radial losses. The plasma is lost axially to both the screen area A_s and the rear wall area A_w. Since there is no DC applied field, the plasma floats relative to the internal surfaces, the electrons are lost to the axial rear wall area and the collection area of the screen grid given by $(1-T_s)A_s$. Neglecting

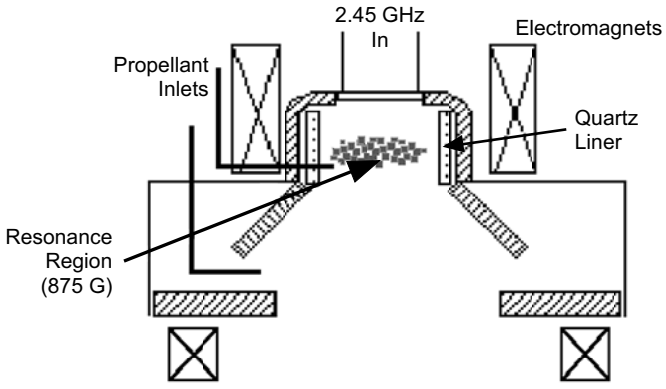

Fig. 4-36. Schematic of microwave ion source with a volume-resonance zone of strong magnetic field produced by electromagnets.

the cost of producing the microwave radiation, the power absorbed by the plasma is equal to the power lost:

$$P_{\text{abs}} = I_p U^+ + I^* U^* + \left(I_s + I_w + I_b\right)\left(\frac{T_{eV}}{2} + \phi\right) + I_a\left(2T_{eV} + \phi\right), \quad (4.6\text{-}26)$$

where I_s is the ion current collected by the screen grid, I_w is the ion current collected by the entire wall, and the ion energy loss is, again, $T_e/2 + \phi$. The amount of energy lost by electrons to the wall assumes that the electrons have a Maxwellian distribution, which may underestimate the energy lost due to the high energy tail in the electron distribution generated by the resonant ECR heating. The discharge loss is the power in (or out) divided by the beam current:

$$\begin{aligned}\eta_d &= \frac{P_{\text{abs}}}{I_b} \\ &= \frac{I_p}{I_b} U^+ + \frac{I^*}{I_b} U^* + \left(\frac{I_s}{I_b} + \frac{I_w}{I_b} + 1\right)\left(\frac{T_{eV}}{2} + \phi\right) + \frac{I_a}{I_b}\left(2T_{eV} + \phi\right).\end{aligned} \quad (4.6\text{-}27)$$

The first three current fractions in this equation are given by Eqs. (4.3-55), (4.3-56), and (4.3-57), respectively. The fourth current fraction is given by

$$\frac{I_w}{I_b} = \frac{\frac{1}{2} n_i e v_a A_w}{\frac{1}{2} n_i e v_a A_s T_s} = \frac{A_w}{A_s T_s}, \quad (4.6\text{-}28)$$

where the wall area A_w is the rear wall area only. The plasma potential is found again from charge conservation by equating the total ion and electron current:

$$\frac{n_i e}{2}\sqrt{\frac{kT_e}{M}}(A_w + A_s) = \frac{n_e e}{4}\sqrt{\frac{8kT_e}{\pi\, m}}\left[A_w + (1 - T_s)A_s\right]\exp^{-e\phi/kT_e}. \quad (4.6\text{-}29)$$

Solving for the plasma potential gives

$$\phi = \frac{kT_e}{e}\ln\left[\frac{A_w + (1 - T_s)A_s}{A_w + A_s}\sqrt{\frac{2M}{\pi\, m}}\right], \quad (4.6\text{-}30)$$

which is different from that found for rf ion thrusters because there is no ion confinement factor due to the induced magnetic fields from the antenna (the

ions are assumed perfectly confined radially due to the strong magnetic field). The electrons are lost to the rear wall and the screen grid, so the final current fraction in Eq. (4.6-27) is

$$\frac{I_a}{I_b} = \frac{\frac{1}{4}\sqrt{\frac{8kT_e}{\pi\, m}} n_e e\left[A_w + (1-T_s)A_s\right]}{\frac{1}{2} n_i e \sqrt{\frac{kT_e}{M}} A_s T_s} \exp^{-e\phi/kT_e}. \tag{4.6-31}$$

Using Eq. (4.6-30) for the plasma potential, this becomes

$$\frac{I_a}{I_b} = \frac{A_w + A_s}{A_s T_s}. \tag{4.6-32}$$

The discharge loss is then

$$\begin{aligned}\eta_d = {} & \frac{2n_o \left\langle \sigma_i v_p \right\rangle V}{\sqrt{\frac{kT_e}{M}} A_s T_s} \left(U^+ + U^* \frac{\left\langle \sigma_* v_e \right\rangle}{\left\langle \sigma_i v_e \right\rangle} \right) \\ & + \left[\frac{1-T_s}{T_s} + \frac{A_w}{A_s T_s} + 1 \right] \left(\frac{T_{eV}}{2} + \phi \right) + \frac{A_w + A_s}{A_s T_s} \left(2T_{eV} + \phi \right),\end{aligned} \tag{4.6-33}$$

with the plasma potential given by Eq. (4.6-30). The electron temperature and neutral density are solved in the same manner as previously for the other types of thrusters. The discharge loss for a generic microwave ion thruster producing 1 A of xenon ions from a 20-cm-diameter grid with 80% transparency is shown in Fig. 4-37 for several thruster lengths. Discharge losses on the order of 200 eV/ion are predicted. This discharge loss is twice that of our idealized ion thruster in Section 4.2 because both the ideal and the microwave source cases assumed ionization by Maxwellian electrons and perfect radial confinement, but the microwave source case includes plasma loss to the rear wall. While the assumption of negligible radial loss is reasonable due to the strong magnetic fields, some additional loss is expected in this direction that will degrade the actual discharge loss somewhat. The large loss area for plasma to the beam area and rear wall tend to drive up the plasma potential to maintain net ambipolar flows and charge balance, which increases the discharge loss compared to well-designed DC discharge thrusters.

Microwave ion source designers mitigate the back wall losses by imposing a stronger magnetic field upstream of the resonance zone. This creates a magnetic mirror, which was described in Chapter 3, that confines the plasma electrons

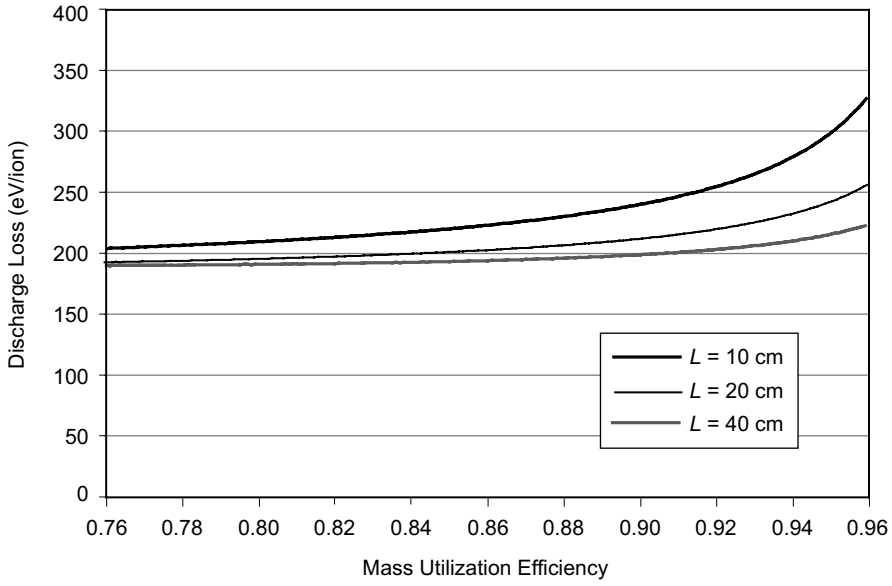

Fig. 4-37. Discharge loss versus mass utilization efficiency for our microwave thruster example with perfect radial confinement.

and reduces the axial losses. Because the magnetic moment (defined as $mv^2/2B$) is invariant along the field lines, electrons with sufficient initial perpendicular velocity are reflected from the increasing magnetic field as their parallel energy is converted into rotational energy. The electrons that are lost have a parallel velocity of

$$v_{\|} > v_{\perp}\sqrt{R_m - 1}, \tag{4.6-34}$$

where R_m is the mirror ratio given by $B_{\max}/B_m$. For example, if the mirror ratio is 5, only electrons with a parallel velocity twice that of their perpendicular velocity will be lost. If the electrons have a Maxwellian distribution with a temperature T_e, then the number of particles with $v_{\|} > 2v_{\perp}$ is $e^{-2} = 13.5\%$, so a large majority of the population is reflected. Since the cyclotron heating adds perpendicular energy to the electrons, mirror ratios of 4 to 6 are very efficient in confining the heated electrons that produce ionization.

The ion source shown in Fig. 4-36 utilizes electromagnets to produce the high field over a significant volume and also to create the confining mirror ratio. However, the power required to operate the electromagnets in this design increases the effective discharge loss and limits the electrical efficiency of the device in thruster applications. In addition, it is difficult to create large area

plasmas with good uniformity using microwave excitation due to the strong magnetic fields that confine the plasma and influence the profile. This leads to other magnetic configurations to produce the plasma using microwave ECR techniques.

In a volume-ionization ECR source, like that shown in Fig. 4-36, a significant fraction of the discharge chamber must be filled with a strong magnetic field to satisfy the resonance condition. If this field is produced by a solenoid, the electrical power required to achieve a sufficient field strength can represent a significant energy cost to the thruster. Likewise, if the field is produced by permanent magnets, the weight of the magnetic material required to produce this field can represent a significant weight penalty for the thruster. This problem can be mitigated by using magnetic multipole boundaries that produce strong magnetic fields at the discharge chamber wall using ring or line-cusp magnet configurations. Figure 4-38 shows the field lines between two magnet rings and the regions of strong magnetic field close to the magnet where the resonant condition is satisfied. Injection of the microwave radiation between the cusps, either by cutoff waveguides inserted between the rows [52], by slotted waveguides run along the rows [53], or by antenna structures placed between the rows, will couple the microwaves to the high magnetic field interaction region.

While this geometry eliminates the solenoidal magnet coils and minimizes the size of the permanent magnets required to produce the resonant field strength, there are several issues remaining. First, the magnetic field strength in the cusp region decreases as one over the distance from the surface squared. This means that very strong magnets are required to produce the resonant field at any significant distance from the wall. Second, electrons that gain energy from the

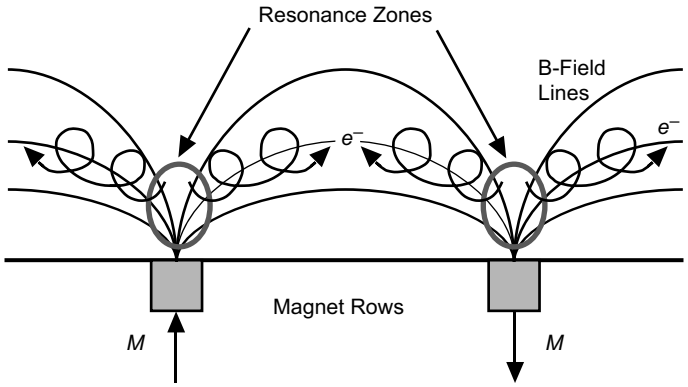

Fig. 4-38. Magnetic field lines and electron cyclotron resonant zone in a ring-cusp wall geometry.

microwaves can be easily lost along the field lines to the wall due to their finite parallel velocity. This means that optimal ECR designs using permanent multipole magnets will have the resonance region as far from the wall as possible and will produce a large mirror ratio approaching the wall to reflect the electrons to avoid excessive direct loss.

Nevertheless, wall losses are a concern in this configuration because the plasma production is a surface effect that is confined to the boundary region, as is the loss. Electrons that are heated in the resonance zone sufficiently to ionize the propellant gas generate plasma on the near-surface magnetic field lines. Coupling the plasma from the resonance region or the surface magnetic layer into the volume of the thruster is problematic due to the reduced cross-field transport. In the other thruster designs discussed in this chapter, the ion production was a volume effect and convective loss a surface effect, so thruster efficiency scaled as the volume-to-surface ratio. This means that larger DC and rf discharge thrusters can be made more efficient than smaller ones. Microwave thrusters, on the other hand, don't scale in the same manner with size because large amounts of plasma must be produced and transported from the surface region to fill the volume of larger thrusters, which can impact the discharge loss. In addition, the plasma density is limited by both cutoff and the magnitude of the resonant field, and so high current density ion production requires very high magnetic fields and high microwave frequencies. Therefore, microwave thrusters have been limited to date to lower current densities and smaller sizes than the other thrusters discussed here. However, work continues on scaling microwave thrusters to larger sizes and higher efficiencies.

The most successful design of a microwave thruster to date is the MUSES-C 10-cm ECR thruster [53–55], which is shown schematically in Fig. 4-39 from [54]. In this case, extremely strong samarium cobalt (SmCo) magnets are used to close the resonance field at the operating frequency between the magnets. This produces heating away from the wall and traps the electrons on the field lines due to an achievable mirror ratio of 2 to 3 in this geometry. The thruster volume is also minimized, with the plasma production region close to the grids. This configuration produces over 1 mA/cm^2 of xenon ions over the active grid region using a 4.2-GHz microwave source with a discharge loss of about 300 eV per ion at over 85% mass utilization efficiency [53].

Finally, there are several other components intrinsic to these thrusters that contribute to the difficulty of achieving high efficiency and compact size in a microwave thruster subsystem. Sources of microwave frequencies in the gigahertz range, such as traveling-wave tubes (TWT) and magnetrons, have efficiencies in the 50% to 70% range, and the power supply to run them is usually about 90% efficient. This represents nearly a factor of two in-line loss

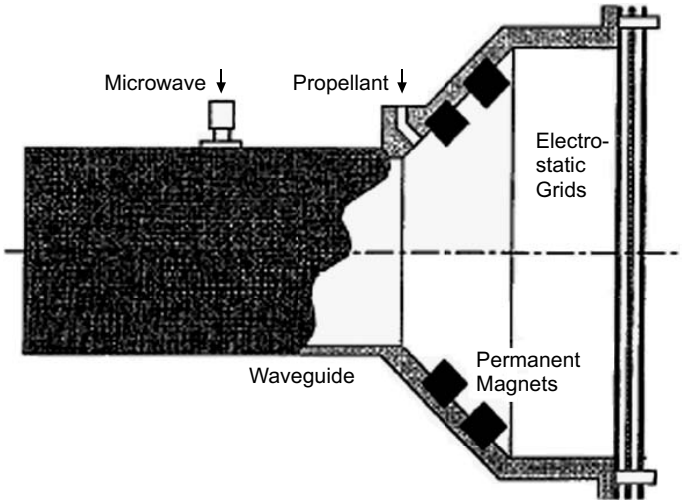

Fig. 4-39. Schematic of the MUSES-C 10-cm microwave source showing the strong magnets and small volume characteristic of these thrusters (from [54]).

of the electrical power delivered to the thruster that must be accounted for in the total discharge cost of the subsystem. The plasma is typically a difficult load to match well, and reflection of 10% to 30% of the microwave energy back into the recirculator (which absorbs the reflected power from the source in the case of mismatch or faults) is typical. The microwave source and recirculator usually represent a significant mass and volume addition to the ion thruster system. An examination of Table 4-1 shows that, in order to avoid cutoff and produce ion current densities to the grids of 1 to 2 mA/cm^2, microwave sources in the 4- to 6-GHz range are required. At this time, space TWTs in this frequency range are limited in power capability to the order of a few hundred watts. For a given discharge loss, this limits the total ion current that can be produced by a microwave thruster. While microwave thrusters hold the promise of eliminating the need for thermionic cathodes used in DC-discharge thrusters and of doing away with the requirement for dielectric discharge chambers in rf thrusters, producing high-efficiency, high-thrust ion propulsion systems based on this technology can be challenging. This is certainly an area for future research.

4.7 2-D Computer Models of the Ion Thruster Discharge Chamber

The analytical models described above can generally explain the behavior and predict the overall discharge chamber performance of well-defined configurations, but multi-dimensional computer models are required to predict

thruster performance parameters such as plasma profile and double-ion content, and to examine the details of different designs. Multi-dimensional modeling of the discharge chamber requires detailed models of discharge chamber walls and magnetic fields as well as of neutral propellant gas, ions, and primary and secondary plasma electrons [56–58]. Because the important physical mechanisms are different, each species (neutral gas, ions, and primary and secondary electrons) is modeled differently. For example, most neutral gas atoms travel in straight lines until they hit a wall or are ionized, so the neutral models can take advantage of simple straight-line trajectories to develop neutral density profiles. On the other hand, primary electron trajectories are dominated by rotation around magnetic field lines, and typically particle-tracking techniques are used to determine the density and spatial distributions. Ion and secondary electron behaviors are obtained using fluid equations due to the relatively collisional behavior of the species. Therefore, ion thruster discharge models that require computer codes that use both fluid and particle-tracking models are known as "hybrid" codes.

Figure 4-40 shows a generic flow diagram for an ion thruster hybrid model [58]. From the thruster inputs (geometry), a mesh is generated inside the discharge chamber. A magnetic field solver determines the field everywhere in the chamber. Depending on the type of mesh used, the mesh generator may be iterated with the magnetic field solver to align the mesh points with the magnetic field lines. Aligning the magnetic field line simplifies the plasma diffusion calculations since the equations can be separated into parallel and perpendicular components, which can result in improved code accuracy for a sufficiently fine mesh. A neutral gas model, such as the "view-factor" model described below, determines the neutral density throughout the volume. The "ionization model" uses the magnetic field and electric field to compute the trajectories of primary electrons and their collisions with other plasma components (i.e., neutrals, ions, secondary electrons), which create ions and serve to dissipate the primary electron energy. The ionization model also determines the collisions due to secondary electrons. The ion optics model determines the transparency of the ion optics to neutrals and ions, as described in detail in Chapter 5. The ion diffusion model uses the magnetic field information and plasma properties to determine the motion of the plasma. The electron thermal model determines the energy balance for the electrons to find the distribution of temperatures of the secondary electron population. These processes are iterated until a convergent solution is found.

4.7.1 Neutral Atom Model

Accurate knowledge of the neutral gas is required in multi-dimensional plasma codes to predict the beam profiles, details of discharge plasma behavior, and

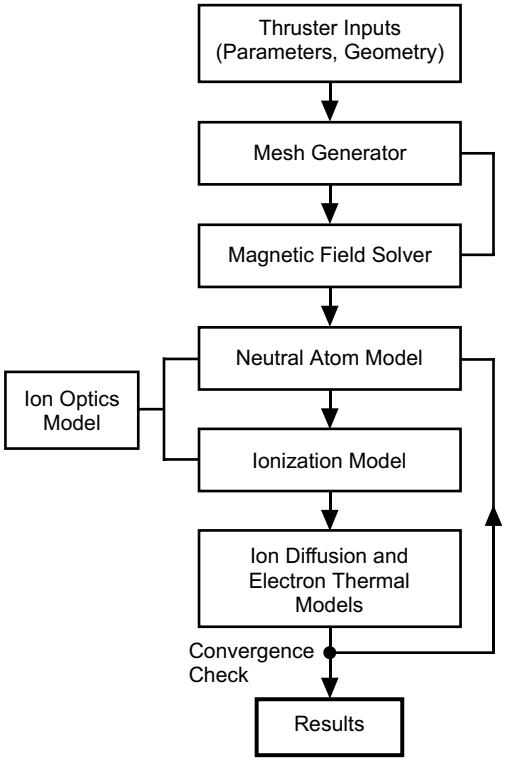

Fig. 4-40. Hybrid 2-D ion thruster discharge model flow diagram and components overview.

thruster performance. For example, many thrusters utilize localized sources and sinks of the neutral gas that produce non-uniform neutral density profiles that must be considered to understand performance.

Ion thrusters operate at internal pressures on the order of 1×10^{-4} torr or lower in order to achieve good mass utilization efficiency. In this pressure range, the neutral gas can be considered to be collisionless, and simple Knudesen-flow models are normally used to determine the average neutral gas density inside the thruster. Assuming surface adsorption, propellant atoms collide with the chamber walls and are re-emitted with a cosine distribution at the wall temperature. Collisions with the wall act to thermalize the gas to the wall temperature. Inside the discharge volume, the neutral atoms collide with electrons and ions. Some neutral atoms are “heated” by charge exchange that transfers the local ion energy to the neutral, but this process has little effect on the average gas temperature. The spatial distribution of the neutral density is dependent on the gas injection regions (sources), gas reflux from the walls, loss

of gas out the ion optic apertures, and the internal “loss” of neutral particles by ionization.

Wirz and Katz [58] developed a technique that accurately predicts the neutral gas density profiles in ion thrusters. Their model utilizes a three-dimensional generalization of the view factor formulation used in thermal models [59]. The view factor approach assumes that neutral particles travel in straight lines between surfaces, and that, after hitting a surface, they are emitted isotropically. In this technique [60], a 3-D boundary mesh and a 2-D internal mesh in the thruster discharge chamber are created for an axisymmetric discharge. The steady-state neutral fluxes are determined by balancing the injection sources, re-emission from the walls, loss through the ion optics, and loss due to ionization. The local neutral density at each of the internal mesh points is calculated by integrating its view factor from the source points (all the other mesh points in the thruster), which includes the “loss” of neutrals between the source and the mesh point due to ionization by the plasma. The ionization losses affect the neutral gas analogous to absorption diminishing the intensity of a light ray. The neutral gas code and the rest of the model components, discussed below, are iterated until a stable solution for the neutral density at each mesh point is found. One advantage of this model is that the neutral gas temperature can be tracked after the gas interacts with the wall temperatures specified at the boundary mesh points. Also, this technique is much faster than a Monte Carlo code since it requires a single matrix solution, allowing the coupling of the neutral and plasma codes to quickly determine both neutral and plasma density profiles.

An example of the axisymmetric boundary (“wall”) and internal meshes for the NSTAR ion thruster from Wirz and Katz [58] is shown in Fig. 4-41. Gas enters from the hollow cathode at the center rear and the propellant injection manifold at the front corner of the discharge chamber. The neutral gas density calculated from this code for the NSTAR thruster in its high-power TH15 mode is shown in Fig. 4-42. The neutral density is highest near the injection sources at the hollow cathode and the propellant injection manifold. The neutral gas is the lowest on axis near the grids due to the NSTAR feed arrangement; however, as discussed below, the high primary electron density found in this region of the thruster produces significant ionization and “burns-out” the neutral gas. This result is critically important because the production of doubly ionized atoms increases dramatically in regions where the neutral gas is burned out and most of the electron energy goes into secondary ionization of the ions in the discharge chamber [58].

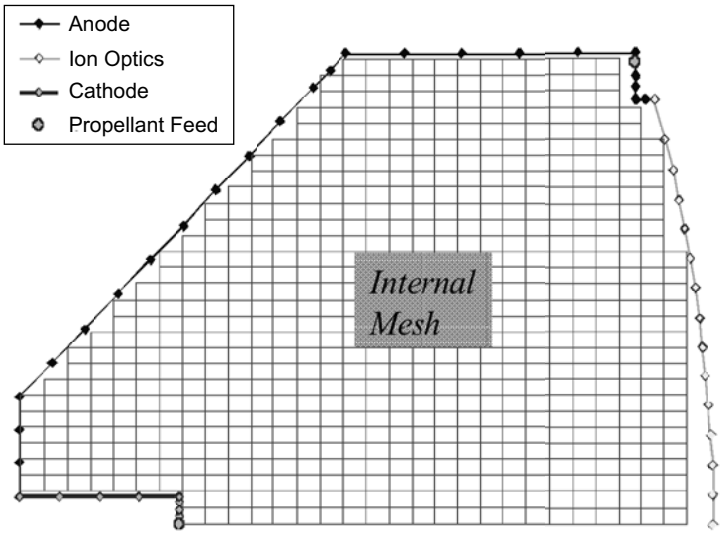

Fig. 4-41. Rectangular internal mesh in an ion thruster (from [58]).

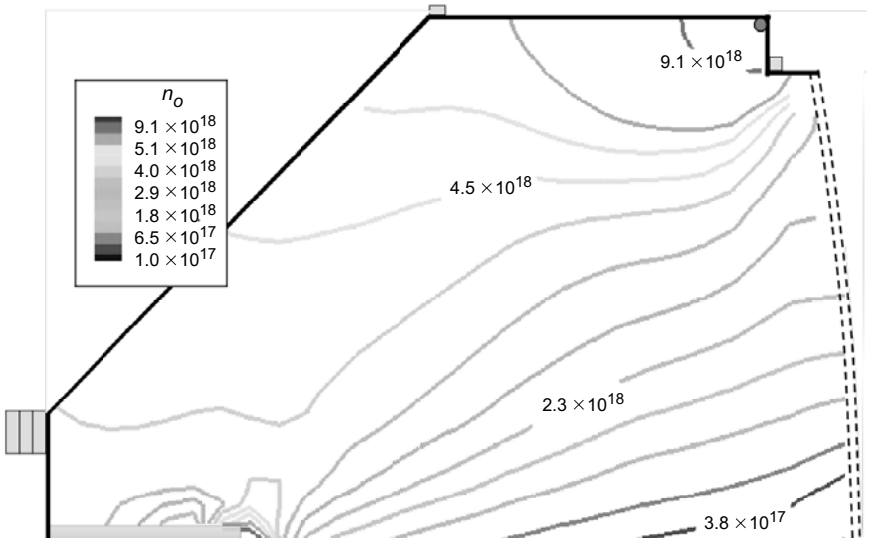

Fig. 4-42. 2-D neutral gas density profiles predicted in the NSTAR thruster for TH15 by Wirz-Katz model using the view-factor code technique [58].

4.7.2 Primary Electron Motion and Ionization Model

Particle simulation methods have been applied to the modeling of primary electron motion in ion thruster discharge chambers [58,61,62]. In particle simulations, the primary electrons are represented by particles, or macro-particles that represent a large number of primary electrons, that move in discrete time steps based on their initial conditions, applied boundary conditions, and internal electric and magnetic fields. Monte Carlo techniques are used to introduce the particles from the cathode exit into the computational domain at randomized velocities indicative of the cathode emission characteristics. During each time step, the local fields are recalculated based on the new particle position and velocity, and the particles move based on the local forces. Monte Carlo techniques typically are used to handle collisions between the particles. This procedure is repeated through many time steps until the particle is lost, after which the next particle is introduced at a unique initial velocity condition.

The primary electron motion between collisions is treated as the motion of a charged particle in the presence of an electromagnetic field, which is described by the Lorentz equation

$$m\frac{\partial \mathbf{v}}{\partial t} = q(\mathbf{E} + \mathbf{v} \times \mathbf{B}). \tag{4.7-1}$$

Wirz and Katz [58] developed an improved Boris-type particle-pushing algorithm [63] in which the motion of the particles can be described with an implicit particle-pushing algorithm, where the Lorentz forces on the particle are decomposed into electric and magnetic forces. The primary's kinetic energy is assumed to be unchanged in an elastic collision, and the particle-scattering angle is estimated by a 3-D probabilistic hard sphere scattering model [58]. In an inelastic collision, some fraction of the primary energy goes into excitation or ionization of the neutrals. Additional energy loss paths exist, as previously discussed, such as coulomb collision thermalization and anomalous processes associated with instabilities. A typical primary trajectory in the NSTAR thruster from the Wirz code [58] is shown in Fig. 4-43, where the primaries are well confined by the strong axial magnetic field component in this thruster, and collisional effects eventually scatter the primary into the cusp loss cone. Arakawa and Yamada's model for primary electron motion is derived from the Euler–Lagrange equations for the Lagrangian of a charge particle in a magnetic field [61]. However, this technique is computationally more intensive and does not improve the results in comparison with the improved Boris algorithm.

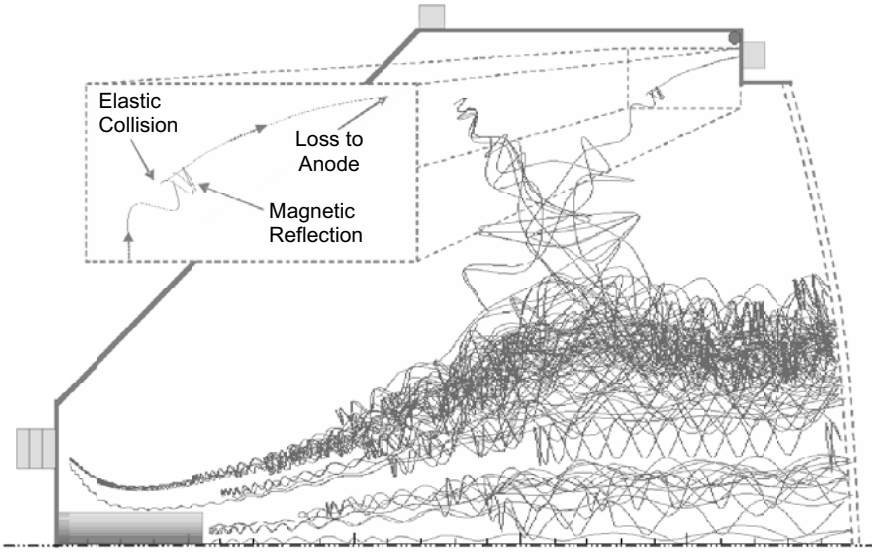

Fig. 4-43. Example primary electron trajectory calculated inside the NSTAR discharge chamber (from [60]).

The primary electron density calculated by Wirz [60] for the TH15 operating condition is shown in Fig. 4-44 and reveals that the magnetic field configuration of NSTAR tends to trap the primary electrons from the cathode on the thruster axis. This trapping of primary electrons, combined with the low neutral density on axis, causes a relatively high rate of production of double ions along the thruster axis.

The ion and secondary electron transport may be treated by an ambipolar ion diffusion equation derived from the single-ion and electron continuity and momentum equations. The steady-state continuity equation for ions is

$$\frac{\partial n}{\partial t} + \nabla \cdot \left(n\mathbf{v} \right) = \dot{n}_s, \tag{4.7-2}$$

where $\dot{n}_s$ is the ion source term. The momentum equation for ions and electrons is

$$m\left[\frac{\partial \left(n\mathbf{v} \right)}{\partial t} + \nabla \cdot \left(n\mathbf{vv} \right) \right] = nq(\mathbf{E} + \mathbf{v} \times \mathbf{B}) - \nabla \cdot \mathbf{p} - nm\sum_n \langle n_n \rangle \left(\mathbf{v} - \mathbf{v}_n \right), \tag{4.7-3}$$

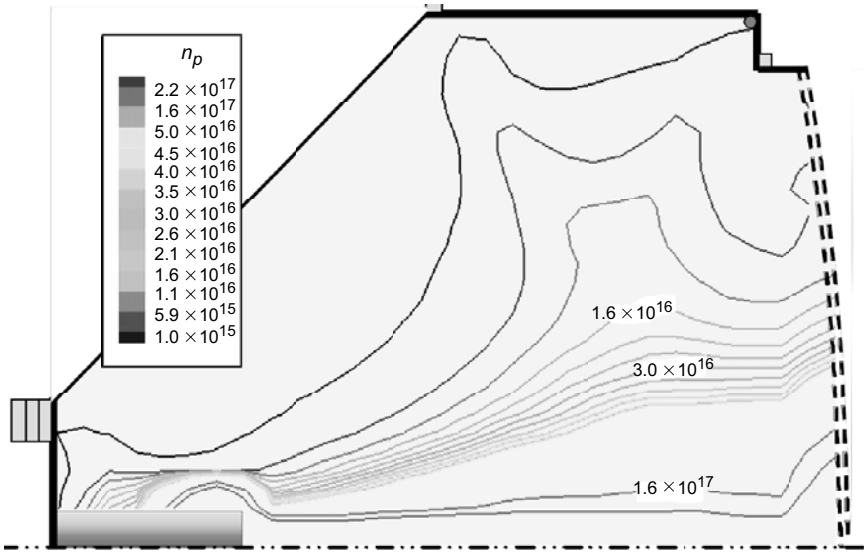

Fig. 4-44. Primary electron density (m^{-3}) for NSTAR throttle level TH15 [60].

where the subscript '*n*' represents the other species in the plasma. Equations (4.7-2) and (4.7-3) can be combined to create a plasma diffusion equation

$$-\mathbf{D}_a \nabla^2 n = \dot{n}_s \,, \tag{4.7-4}$$

where $\mathbf{D}_a$ is the ambipolar diffusion coefficient. The diffusion coefficient is separated into parallel and perpendicular components, such that

$$\begin{aligned} \mathbf{D}_a &= \begin{bmatrix} D_{\|a} & 0 \\ 0 & D_{\perp a} \end{bmatrix} \\ D_{\|a} &= \frac{\mu_e D_i + \mu_i D_e}{\mu_i + \mu_e} \\ D_{\perp a} &= \frac{\mu_e D_{\perp i} + \mu_i D_{\perp e}}{\mu_i + \mu_e}, \end{aligned} \tag{4.7-5}$$

where the species mobilities and diffusion coefficients are determined by separately equating the parallel and cross-field fluxes of ions and electrons [64]. This simplified plasma diffusion equation assumes uniform ion and secondary electron production rates and temperatures; a derivation that does include these simplifying assumptions is given by Wirz [60].

The thermal electron energy conservation equation is derived by multiplying the Boltzmann equation by $mv^2/2$ and integrating over velocity to give

$$\frac{\partial}{\partial t}\left(\frac{nm}{2}\mathbf{v}^2+\frac{3}{2}nkT\right)+\nabla\cdot\left[\left(\frac{nm}{2}\mathbf{v}^2+\frac{5}{2}nkT\right)\mathbf{v}+\mathbf{q}\right]=en\mathbf{E}\cdot\mathbf{v}+\mathbf{R}\cdot\mathbf{v}+Q_e+Q_c, \tag{4.7-6}$$

where viscous effects are ignored and **R** is the mean change of momentum of electrons due to collisions with other species. This equation is combined with the electron fluxes to the boundaries and thermal conductivity to determine the total energy loss to the boundaries. Temperatures calculated from the electron energy equation are shown in Fig. 4-45 for the NSTAR thruster. The strong on-axis confinement of the primaries in NSTAR tends to locally heat the plasma electron population, generating a high on-axis plasma temperature.

4.7.3 Discharge Chamber Model Results

The 2-D discharge chamber model developed by Wirz and Katz [58] has been verified against beam profile and performance data for the 30-cm NSTAR thruster. The model results for the NSTAR thruster at throttle condition TH15 are plotted in Fig. 4-46, where the beam current density profile calculated by the model agrees well with experimental data obtained during the 8200-hour-

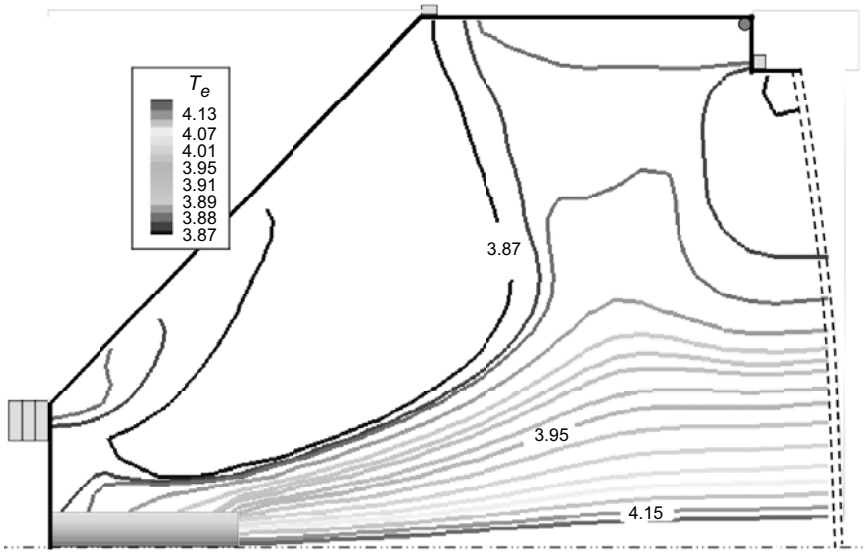

Fig. 4-45. Secondary electron temperatures (eV) for NSTAR thruster at TH15 [60].

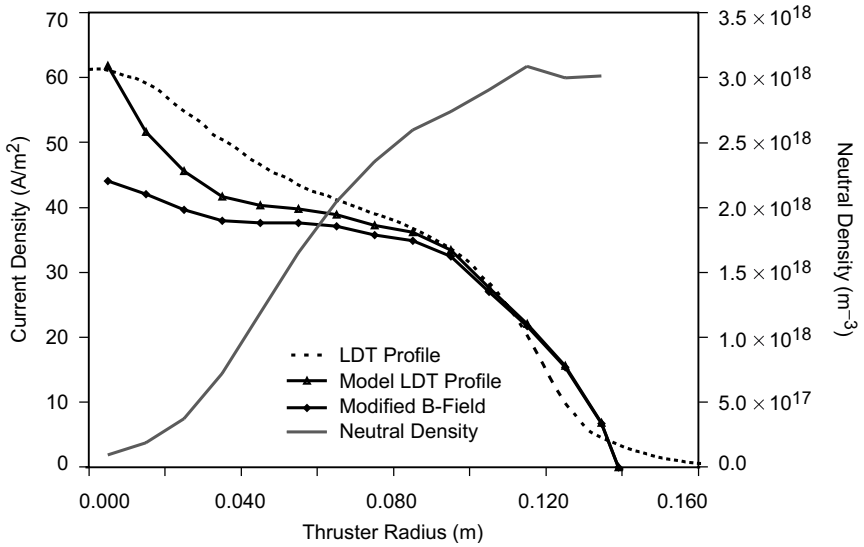

Fig. 4-46. Beam and neutral density profiles at the NSTAR grid [60].

long duration test [65]. The peaked plasma profile is due to the strong confinement of the electrons from the cathode by the NSTAR magnetic configuration, which depletes the neutral gas on axis and produces a significant number of double ions. The modified B-field profile in Fig. 4-46 is an example of the model prediction for the case of a modified magnetic field geometry that makes it easier for primary electrons to move away from the thruster axis. The ion density calculated by the Wirz–Katz model for the NSTAR magnetic is shown in Fig. 4-47. As suggested by the primary density and plasma electron temperatures in Figs. 4-44 and 4-45, the plasma density is strongly peaked on axis. Finally, the double-to-total ion ratio distribution throughout the discharge chamber is shown in Fig. 4-48. These results agree with experimental data that suggest the on-axis peak in the NSTAR beam profile is due to high centerline double-ion content.

Analysis by the Wirz–Katz model results shows that the original NSTAR magnetic field configuration tends to trap primary electrons on axis, which increases local electron temperature, ionization rate, and the generation of double ions in this region. This trapping of primary electrons also manifests in a neutral atom depletion on axis, as was shown in Fig. 4-46. The “modified” configuration in this figure shows the power of a good computer model to improve ion thruster design. By allowing the primary electrons to move away from the thruster axis, the ionization is spread more uniformly throughout the discharge chamber. The flatter profile results from a decrease in primary

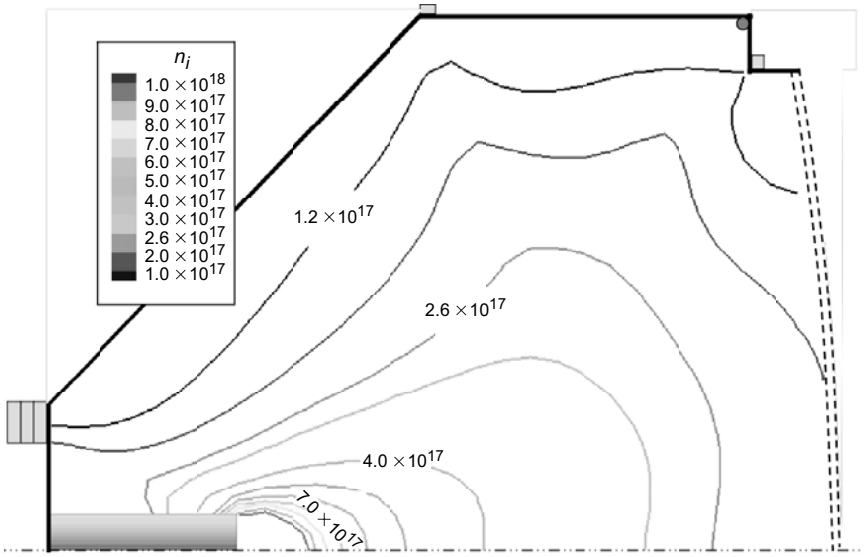

Fig. 4-47. Ion plasma density (m^{-3}) for the NSTAR at throttle level TH15 [60].

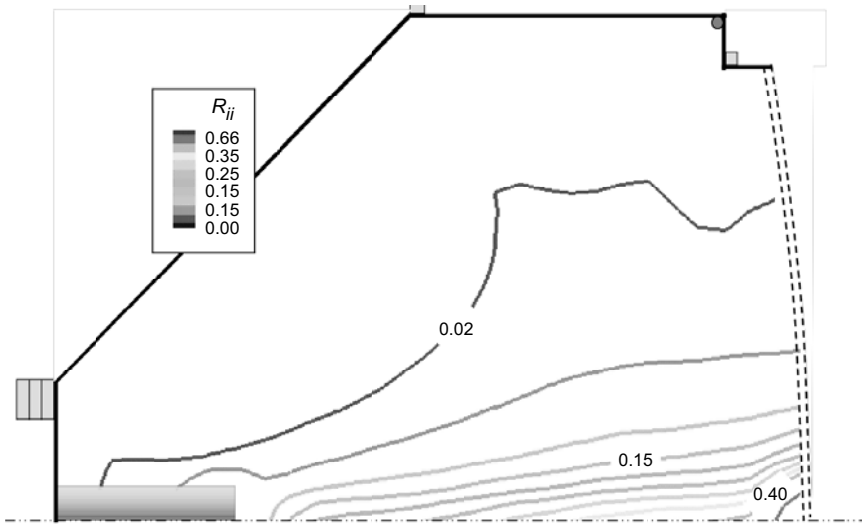

Fig. 4-48. Double ion density ratio (n^{++}/n^{+}) for NSTAR operating at a power level of TH15 [60].

electron density, and hence double-ion content, on the thruster centerline. Wirz and Goebel [66] developed "modified" NSTAR designs that guide primary electrons away from the thruster centerline to improve the profile. These designs were validated by experiments [67], and also resulted in lower double-ion content and higher neutral density along the thruster axis as predicted by the model.

References

[1] H. R. Kaufman, "An Ion Rocket with an Electron-Bombardment Ion Source," *NASA Technical Note*, D-585, January 1961.

[2] P. D. Reader, *NASA Technical Note*, TN D-1162, 1962.

[3] R. T. Bechtel, "Discharge Chamber Optimization of the Sert-II Thruster," *Journal of Spacecrafts and Rockets*, vol. 5, p. 795–800, 1968.

[4] W. Knauer, R. L. Poeschel, and J. W. Ward, "The Radial Field Kaufman Thruster," AIAA-1969-259, 7th Electric Propulsion Conference, Williamsburg, Virginia, March 3–5, 1969.

[5] R. D. Moore, "Magneto-Electrostatic Contained Plasma Ion Thruster," AIAA-1969-260, 1969.

[6] J. S. Sovey, "Improved Ion Containment Using a Ring-Cusp Ion Thruster," *Journal of Spacecraft*, vol. 21, pp. 488–495, 1984.

[7] J. S. Sovey and H. J. King, "Status of 30-cm Mercury Ion Thruster Development," NASA TMX-71603, October 1974.

[8] T. D. Masek, R. L. Poeschel, C. R. Collett, and D. E. Snelker, "Evolution and Status of the 30-cm Engineering Model Ion Thruster," AIAA-1976-1006, International Electric Propulsion Conference, Key Biscayne, Florida, November 14–17, 1976.

[9] V. K. Rawlin, "Operation of the J-Series Thruster Using Inert Gases," AIAA-1982-1929, International Electric Propulsion Conference, New Orleans, Louisiana, November 17–19, 1982.

[10] J. R. Beattie and J. N. Matossian, "Inert-Gas Ion Thruster Technology," NASA CR191093, March 1993.

[11] J. R. Beattie and R. L. Poeschel, "Ring-Cusp Ion Thrusters," Paper 84-71, *International Electric Propulsion Conference*, May 1984.

[12] J. N. Matossian and J. R. Beattie, "Characteristics of Ring-Cusp Discharge Chambers," *Journal of Propulsion and Power*, vol. 7, pp. 968–974, 1991.

[13] M. J. Patterson, T. W. Haag, V. K. Rawlin, and M. T. Kussmaul, "NASA 30-cm Ion Thruster Development Status," AIAA-1994-2849, 30th Joint Propulsion Conference, Indianapolis, Indiana, June 1994.

[14] J. R. Beattie, J. N. Matossian, and R. R. Robson, "Status of Xenon Ion Propulsion Technology," *Journal of Propulsion and Power*, vol. 7, pp. 145–150, 1990.

[15] T. D. Maske, "Plasma Properties and Performance of Mercury Ion Thrusters," *AIAA Journal*, vol. 9, pp. 205–212, 1971.

[16] J. Ward and T. Masek, "A Discharge Computer Model for an Electron Bombardment Thruster," AIAA-1976-1009, AIAA International Electric Propulsion Conference, Key Biscayne, Florida, November 14–17, 1976.

[17] J. N. Matossian and J. R. Beattie, "Model for Computing Volume Averaged Plasma Properties in Electron-Bombardment Ion Thrusters," *Journal of Propulsion and Power*, vol. 5, pp.188–196, 1989.

[18] J. R. Brophy, *Ion Thruster Performance Model*, NASA CR-174810, Ph.D. Thesis, Colorado State University, Fort Collins, Colorado, December 1984.

[19] J. R. Brophy and P. J. Wilbur, "Simple Performance Model for Ring and Line Cusp Ion Thrusters," *AIAA Journal*, vol. 23, no. 11, pp. 1731–1736, 1985.

[20] D. M. Goebel, J. E. Polk, and A. Sengupta, "Discharge Chamber Performance of the NEXIS Ion Thruster," AIAA-2004-3813, 40th AIAA Joint Propulsion Conference, Fort Lauderdale, Florida, July 11–14, 2004.

[21] D. M. Goebel, R. E. Wirz, and I. Katz, "Analytical Ion Thruster Discharge Performance Model," AIAA-2006-4486, 42nd Joint Propulsion Conference, Sacramento, California, July 10–13, 2006.

[22] D. M. Goebel, "Ion Source Discharge Performance and Stability," *Physics of Fluids*, vol. 25, no. 6, pp. 1093–1102, 1982.

[23] A. T. Forrester, *Large Ion Beams*, New York: John Wiley and Sons, 1988.

[24] M. Lieberman and A. Lichtenberg, *Principles of Plasma Discharges and Materials Processing*, New York: John Wiley and Sons, 1994.

[25] Maxwell 3-D is a product of Ansoft Corp., http://www.ansoft.com/products/em/max3d/overview.cfm.

[26] R. E. Wirz and D. M. Goebel, "Ion Thruster Discharge Performance per Magnetic Field Geometry," AIAA-2006-4487, 42nd Joint Propulsion Conference, Sacramento, California, July 10–13, 2006.

[27] K. Leung, N. Hershkowitz, and K. MacKenzie, "Plasma Confinement by Localized Cusps," *Physics of Fluids*, vol. 19, no. 7, pp. 1045–1053, 1976.

[28] D. Rapp and P. Englander-Golden, "Total Cross Sections for Ionization and Attachment in Gases by Electron Impact. I. Positive Ionization," *The Journal of Chemical Physics*, vol. 43, no. 5, pp. 1464–1479, 1965.

[29] M. Hayashi, "Determination of Electron-Xenon Total Excitation Cross-Sections, from Threshold to 100-eV, from Experimental Values of Townsend's a," *Journal of Physics D: Applied Physics*, vol. 16, pp. 581–589, 1983.

[30] R. R. Peters, P. J. Wilbur, and R. P. Vahrenkamp, "A Doubly Charged Ion Model for Ion Thrusters," *Journal of Spacecraft and Rockets*, vol. 14, no. 8, pp. 461–468, 1977.

[31] P. Clausing, "The Flow of Highly Rarefied Gases Through Tubes of Arbitrary Length," *Journal of Vacuum Science and Technology*, vol. 8, pp. 636–646, 1971.

[32] L. Spitzer, *Physics of Fully Ionized Gases*, New York: Interscience Publishers, p. 80, 1956.

[33] D. L. Book, *NRL Plasma Formulary*, Naval Research Laboratory, Washington D.C., pp. 33–34, 38, 1987.

[34] J. R. Brophy, I. Katz, J. E. Polk, and J. R. Anderson, "Numerical Simulations of Ion Thruster Accelerator Grid Erosion," AIAA Paper 2002-4261, 38th Joint Propulsion Conference, July 7–10, 2002.

[35] J. J. Anderson, I. Katz, and D. Goebel, "Numerical Simulation of Two-Grid Ion Optics Using a 3D Code," AIAA-2004-3782, 40th Joint Propulsion Conference, Ft. Lauderdale, Florida, July 2004.

[36] D. M. Goebel, K. Jameson, I. Katz, and I. Mikellades, "Hollow Cathode Theory and Modeling: I. Plasma Characterization with Miniature Fast-Scanning Probes," *Journal of Applied Physics*, vol. 98, no. 10, 113302, 2005.

[37] I. Mikellades, I. Katz, D. M. Goebel, and J. E. Polk, "Hollow Cathode Theory and Modeling: II. A Two-Dimensional Model of the Emitter Region," *Journal of Applied Physics*, vol. 98, no. 10, 113303, 2005.

[38] J. E. Polk, D. M. Goebel, I. Katz, J. Snyder, A. Schneider, L. Johnson, and A. Sengupta, "Performance and Wear Test Results for a 20-kW Class Ion Engine with Carbon-Carbon Grids," AIAA-2005-4393, 41st Joint Propulsion Conference, Tucson, Arizona, July 10–13, 2005.

[39] J. R. Brophy, "NASA's Deep Space 1 Ion Engine," *Review of Scientific Instruments*, vol. 73, pp. 1071–1078, 2002.

[40] K. K. Jameson, D. M. Goebel, and R. M. Watkins, "Hollow Cathode and Keeper-Region Plasma Measurements," AIAA-2005-3667, 41st AIAA Joint Propulsion Conference, Tucson, Arizona, July 10–13, 2005.

[41] P. J. Wilbur and J. R. Brophy, "The Effect of Discharge Chamber Wall Temperature on Ion Thruster Performance," *AIAA Journal*, vol. 24, no. 2, pp. 278–283, 1986.

[42] J. M. Lafferty, *Foundations of Vacuum Science and Technology,* New York: John Wiley and Sons, 1998.

[43] Y. Hayakawa, K. Miyazaki, and S. Kitamura, "Measurements of Electron Energy Distributions in a 14-cm Diameter Ring Cusp Ion Thruster," *Journal of Propulsion and Power*, vol. 8, pp. 118–126, 1992.

[44] D. Herman, "Discharge Cathode Electron Energy Distribution Functions in a 40-cm NEXT-type Ion Engine," AIAA-2005-4252, 41st AIAA Joint Propulsion Conference, Tucson, Arizona, July 10–13, 2005.

[45] D. Bohm, Chapter 1, *The Characteristics of Electric Discharges in Magnetic Fields*, edited by A. Guthrie and R. Wakerling, New York: McGraw-Hill, pp. 1–76, 1949.

[46] N. L. Milder, "A Survey and Evaluation of Research on the Discharge Chamber Plasma of a Kaufman Thruster," AIAA-69-494, 5th Propulsion Joint Specialist Conference, U.S. Air Force Academy, Colorado Springs, Colorado, June 9–13, 1969.

[47] H. R. Kaufman, "Performance of Large Inert-Gas Thrusters," AIAA-81-0720, 15th International Electric Propulsion Conference, Las Vegas, Nevada, April 21–23, 1981.

[48] T. Ozaki, E. Nishida, Y. Gotoh, A. Tsujihata, and K. Kajiwara, "Development Status of a 20 mN Xenon Ion Thruster," AIAA-2000-3277, 36th Joint Propulsion Conference, Huntsville, Alabama, July 16–19, 2000.

[49] W. F. Divergilio, H. Goede, and V. V. Fosnight, "High Frequency Plasma Generators for Ion Thrusters," NASA #CR-167957, November 1981.

[50] H. J. Leiter, R. Killinger, H. Bassner, J. Miller, R. Kulies, and T. Fröhlich, "Evaluation of the Performance of the Advanced 200 mN Radio Frequency Ion Thruster RIT_XT," AIAA-2002-3836, 38th Joint Propulsion Conference, Indianapolis, Indiana, July 7–10, 2002.

[51] M. Tuszewski, "Inductive Electron Heating Revisited," *Physics of Plasmas*, vol. 4, pp. 1922–1928, 1997.

[52] H. Goede, "30-cm Electron Cyclotron Plasma Generator," *Journal of Spacecraft*, vol. 24, no. 5, p. 437, 1987.

[53] H. Kuninaka and S. Satori, "Development and Demonstration of a Cathode-less Electron Cyclotron Resonance Ion Thruster," *Journal of Propulsion and Power*, vol. 14, pp. 1022–1026, 1998.

[54] H. Kuninaka, I. Funaki, and K. Toki, "Life Test of Microwave Discharge Ion Thrusters for MUSES-C in Engineering Model Phase," AIAA-99-2439, 35th Joint Propulsion Conference, Los Angeles, California, June 20–24, 1999.

[55] H. Kuninaka, I. Funaki, K. Nishiyama, Y. Shimizu, and K. Toki, "Results of 18,000 Hour Endurance Test of Microwave Discharge Ion Thruster Engineering Model," AIAA-2000-3276, 36th Joint Propulsion Conference, Huntsville, Alabama, July 16–19, 2000.

[56] Y. Arakawa and K. Ishihara, "A Numerical Code for Cusped Ion Thrusters," IEPC-91-118, 22nd International Electric Propulsion Conference, Viareggio, Italy, October 14–17, 1991.

[57] Y. Arakawa and P. J. Wilbur, "Finite Element Analysis of Plasma Flows in Cusped Discharge Chambers," *Journal of Propulsion and Power*, vol. 7, no. 1, pp. 125–128, 1991.

[58] R. Wirz and I. Katz, "Plasma Processes in DC Ion Thruster Discharge Chambers," AIAA-2005-3690, 41st AIAA Joint Propulsion Conference, Tucson, Arizona, July 10–13, 2005.

[59] R. Siegel and J. R. Howell, *Thermal Radiation Heat Transfer*, 4th Edition, New York: Taylor & Francis, pp. 226–227, 2002.

[60] R. Wirz, "Discharge Plasma Processes of Ring-Cusp Ion Thrusters," Ph.D. Dissertation, Aeronautics, California Institute of Technology, Pasadena, California, 2005.

[61] Y. Arakawa and T. Yamada, "Monte Carlo Simulation of Primary Electron Motions in Cusped Discharge Chambers," AIAA-1990-2654, 21st International Electric Propulsion Conference, Orlando, Florida, July 18–20, 1990.

[62] S. Mahalingam and J. A. Menart, "Primary Electron Modeling in the Discharge Chamber of an Ion Engine," AIAA-2002-4262, 38th Joint Propulsion Conference, Indianapolis, Indiana, July 7–10, 2002.

[63] J. P. Boris, "Relativistic Plasma Simulations-Optimization of a Hybrid Code," Proc. 4th Conf. on Numerical Simulation of Plasmas, NRL Washington, Washington DC, 1970.

[64] S. I. Braginskii, "Transport Processes in Plasmas," *Reviews of Plasma Physics*, vol. 1, pp. 205–311, 1965.

[65] J. Polk, J. R. Anderson, J. R. Brophy, V. K. Rawlin, M. J. Patterson, J. Sovey, and J. Hamley "An Overview of the Results from an 8200 Hour Wear Test of the NSTAR Ion Thruster," AIAA Paper 99-2446, 35th Joint Propulsion Conference, Los Angeles, California, 1999.

[66] R. E. Wirz and D. M. Goebel, "Ion Thruster Discharge Performance per Magnetic Field Geometry," AIAA-2006-4487, 42nd Joint Propulsion Conference, Sacramento, California, July 10–13, 2006.

[67] A. Sengupta, "Experimental Investigation of Discharge Plasma Magnetic Confinement in an NSTAR Ion Thruster," AIAA-2005-4069, 41st Joint Propulsion Conference, Tucson, Arizona, July 10–13, 2005.

Homework Problems

1. Show the conditions under which the ambipolar velocity of the ions flowing to the wall in a transverse magnetic field reverts to the Bohm velocity.

2. An ion thruster discharge chamber has an internal pressure of 10^{-4} torr, a plasma density of 2×10^{17} m^{-3}, gas and ion temperatures of 500 K, electron temperature of 4 eV, and a transverse magnetic field of 40 G near the wall with a diffusion length of 2 cm. What is the average transverse ion velocity and the ion confinement factor (ratio of v_i / v_{Bohm})?

3. In Fig. 4-16 it is shown that the reaction rate for ionization exceeds the reaction rate for excitation if the electron temperature exceeds about 9 eV. Why not run discharges with $T_e \geq 9$ eV where ionization is greater than excitation? Give a quantitative answer for an idealized thruster producing 1 A with 10-cm-diameter grids on a discharge chamber 10 cm in diameter and 15 cm long with the anode being the full cylindrical and back wall area. Assume an 80% grid transparency and a neutral density of 10^{18} cm^{-3}, and plot the discharge loss as a function of electron temperature from 3 to 10eV. Explain why. (Hint: examine the various loss terms.)

4. What is the electron temperature in a xenon ion thruster that has an ion loss area of 200 cm^2, a plasma volume of 10^4 cm^3, neutral gas density of 10^{13} cm^{-3}, and a 5% primary electron density at 15 eV?

5. A thruster plasma has a volume of 10^4 cm^3, has a neutral density of 10^{12} cm^{-3}, is 10% ionized with 15-V primary electrons, has a 5-eV electron temperature, and has a primary loss area of 10 cm^2. What are the primary electron confinement time, the primary electron collision time (assume a collision cross section of 2×10^{-16} cm^2), and the primary electron slowing down time? What is the total effective confinement time for a primary electron, and which of the three contributors to the total confinement time is the most important?

6. For a xenon ion thruster with a grid area of 500 cm^2 with a screen grid transparency of 70%, what is the discharge current required to produce a 2.5-A ion beam? Assume a discharge voltage of 25 V, a hollow cathode voltage drop of 10 V, a plasma potential of 5 V, a primary electron density of 5%, and an excitation energy of 10 eV. You can neglect the ion and primary electron loss to the anode, the ion current back to the cathode, and any losses to the back wall of the cylindrical discharge chamber with the same diameter as the grids.

7. A xenon ion thruster discharge chamber produces a 5×10^{17} m^{-3} plasma 20 cm in diameter with an electron temperature of 5.5 eV. What is the beam current and average current density if the screen grid transparency is 80%, and what flatness parameter is required to maintain the peak current density under 10 mA/cm^2?

8. A xenon ion thruster has a grid diameter of 20 cm with a transparency of 75%, an electron temperature of 3 eV in a 30-cm-diameter, 30-cm-long cylindrical discharge chamber with an ion confinement factor of 0.1. What does the cusp anode area have to be to maintain the plasma potential at the sheath edge at 6 V? You can assume that the discharge current is 10 times the beam current and neglect the back wall loss area and primary electron effects. Assuming the ion temperature is 0.1 eV and that there are 3 magnetic rings around the cylindrical chamber, what is the magnetic field at the wall required to produce this cusp anode area?

9. An rf xenon ion thruster has a grid diameter of 10 cm, a grid transparency of 70%, and a cylindrical discharge chamber with a diameter and length of 10 cm. Assuming an electron temperature of 4 eV, an ion confinement factor of 0.5, and a neutral density of 6×10^{18} m^{-3}, what is the plasma potential and discharge loss? If the cylindrical discharge chamber is made into a cone 10 cm long from the grid diameter, how do the plasma potential and discharge loss change?

10. A microwave ion thruster produces 2 A from an 80% transparent grid using a 4-GHz microwave source. If the thruster is running at 90% of cutoff with a flatness parameter of 0.6, what must the diameter of the grid be to produce this beam current?